AN ABSTRACT OF THE DISSERTATION OF

Nicholas A. Forfinski-Sarkozi for the degree of Doctor of Philosophy in Civil Engineering presented on October 25, 2019.

Title: Mapping Nearshore Bathymetry with Spaceborne Data Fusion and State Space Modeling.

Abstract approved: _____

Christopher E. Parrish

Despite numerous techniques for measuring and estimating water depth, bathymetry in the nearshore zone is notoriously difficult to map. Dangerous sea states, noisy environmental conditions, and expensive survey operations, particularly in remote areas, contribute to the difficulties of obtaining data along the coast. Global datasets, derived mainly from satellite altimetry methods, do exist, but they have significant limitations nearshore. Numerous high-resolution datasets, conventionally acquired with acoustic and lidar techniques, also exist, but they cover only a small percentage of the world's coasts. Spaceborne data fusion employing multispectral satellite derived bathymetry (SDB) offers the potential to significantly reduce the global lack of nearshore bathymetry, coined the "white ribbon" by the hydrographic community, referring to the alongshore data gap on many nautical charts. A broad term, multispectral SDB spans a diverse spectrum of methods that have been used extensively in specific case studies, but the application of multispectral SDB on a global or regional scale is significantly limited by the availability of in situ reference depths needed to tune derived values. Additionally, many existing approaches only use a single multispectral image, which can result in significant errors or missing data if the image contains environmental or sensor noise, such as clouds, sediment plumes, or detector-edge artifacts. This dissertation presents two spaceborne empirical multispectral SDB methods to address shortcomings of existing SDB approaches and reduce the global shortage of nearshore bathymetry – (1) active/passive spaceborne data fusion combining MABEL/ICESat-2 and multispectral data and (2) state space modeling of Sentinel-2 and Landsat 8 multispectral data to generate gap-free models of relative SDB (rSDB) with corresponding uncertainty estimates.

The recently launched ICESat-2 mission offers an opportunity for a completely spaceborne active-passive data fusion approach to nearshore bathymetry by potentially providing a global source of nearshore reference depths to tune empirical multispectral SDB algorithms. The main

objectives of the ICESat-2 mission are to measure ice-sheet elevations, sea-ice thickness, and global biomass, but ICESat-2's 532-nm wavelength photon-counting Advanced Topographic Laser Altimeter System (ATLAS) was first posited, then demonstrated capable of detecting bathymetry in certain nearshore environments. Presented in two studies conducted prior to ICESat-2's launch, the active-passive approach is demonstrated with data from MABEL, NASA's high-altitude ATLAS simulator system. The first study assessed the ability to derive bathymetry from MABEL and then evaluated the accuracy and reliability of MABEL bathymetry using data acquired in Keweenaw Bay, Lake Superior. The study also developed and verified a baseline model to predict numbers of bottom returns as a function of water depth. The second study completed the demonstration of the spaceborne active/passive data fusion method by synergistically fusing MABEL-derived bathymetry and Landsat 8 multispectral Operational Land Imager (OLI) imagery over the entire Keweenaw Bay study site using the Stumpf band-ratio algorithm. The study also assessed the spatiotemporal viability of the data fusion approach by characterizing the variability of global coastal water clarity as interpreted from Visible Infrared Imaging Radiometer Suite (VIIRS) Kd(490) data. The calculated SDB agreed with a high-resolution topobathymetric lidar dataset to within an RMSE of 0.7 m, and the spatiotemporal viability analysis indicated that the spaceborne active-passive data fusion approach may be viable over many regions of the globe throughout the course of a year.

State space modeling of empirical multitemporal SDB overcomes limitations of single-image SDB by leveraging the bathymetric signal in multispectral time series to create gap-free models of relative SDB (rSDB) for an arbitrary date, enabling SDB for dates with noisy or no data. State space models (SSMs) are well established in many applications but are absent in empirical SDB literature. Consisting of a state equation, which relates consecutive state vectors, and an observation equation, which relates observations to the state vector, SSMs are typically solved using Kalman filtering techniques, which provide estimates of uncertainties along with state estimates. SSMs also provide a mechanism for data fusion by allowing an observation equation for multiple observed time series. The third study demonstrates a state space approach to empirical multispectral SDB by applying local level SSMs to Landsat 8 OLI and Sentinel-2 MSI rSDB time series, both separately and fused. A representative single-sensor SSM (Landsat 8) was transformed to SDB that agreed with a high-resolution topobathymetric lidar dataset to within an RMSE of 0.29 m, which indicates the promising performance of the state space framework. Internally consistent fused-sensor SSMs verified that state space modeling also offers a data-fusion method capable of incorporating time series from a diverse suite of multispectral sensors.

Mapping Nearshore Bathymetry with Spaceborne Data Fusion and State Space Modeling

by
Nicholas A. Forfinski-Sarkozi

A DISSERTATION

submitted to

Oregon State University

in partial fulfillment of
the requirements for the
degree of

Doctor of Philosophy

Presented October 25, 2019
Commencement June 2020

Doctor of Philosophy dissertation of Nicholas A. Forfinski-Sarkozi presented on October 25, 2019

APPROVED:

Major Professor, representing Civil Engineering

Head of the School of Civil and Construction Engineering

Dean of the Graduate School

I understand that my dissertation will become part of the permanent collection of Oregon State University libraries. My signature below authorizes release of my dissertation to any reader upon request.

Nicholas A. Forfinski-Sarkozi, Author

ACKNOWLEDGEMENTS

I would like to thank my advisor, Dr. Christopher Parrish, for the opportunity to study at Oregon State University. His kindness, patience, and infectious excitement made for a great teacher and mentor. I would also like to thank my committee members, Dr. Michael Olsen, Dr. Merrick Haller, Dr. Anne Nolin, and Dr. Robert Kennedy for their support and expertise.

I would also like to thank my fellow OSU geomatics students. Your help with homework assignments, commiseration with the little annoying things, and your friendship were crucial. Outside of OSU, I would like to thank the following people: Dr. Kathy Brandt, an ICESat-2 scientist with Goddard Space Flight Center, for providing information about MABEL positioning; Dr. Minsu Kim, an SGT Inc. contractor with the USGS EROS Center, for his helpful lidar equation suggestions; and Chad Fulton, an economist with the Board of Governors of the Federal Reserve System and contributor to the Python package *statsmodels*, whose expeditious help with state space modeling was most appreciated.

Finally, I would like to thank my fellow Hooverville-ite and husband, Jason S. Sarkozi-Forfinski, to whose sensory input patterns my mental pathways have become quite accustomed.

This dissertation contains research that was funded by NASA Research Opportunities in Space and Earth Sciences (ROSES) Grant NNX15AQ22G and AmericaView Grant Number G14AP00002, from the Department of the Interior, United States Geological Survey.

TABLE OF CONTENTS

Page

LIST OF FIGURES

Figure Page

LIST OF FIGURES (Continued)

Figure Page

LIST OF FIGURES (Continued)

Figure Page

Figure Page

LIST OF TABLES

INTRODUCTION

Despite a wide variety of techniques for measuring or estimating water depth, there exists a global shortage of nearshore bathymetry. Even in countries with dedicated mapping agencies, "there is a widespread need for more and better data in the coastal zone," particularly along the water/land interface (NRC, 2004). In fact, the hydrographic community has coined the term *white ribbon* to describe this general lack of data, referring to the alongshore strip of whitespace (i.e., no data) present on many nautical charts. The white ribbon, however, affects numerous domains beyond hydrography and nautical charting. Benthic mapping, sea-level change and inundation modeling, coastal engineering, and digital terrain modeling are among applications negatively impacted by sparse or missing bathymetric data. Global bathymetric datasets do exist, but most global-scale data have been derived from coarse-resolution gravity/altimetry techniques with significant limitations in the coastal zone. High-resolution nearshore datasets, such as those produced by shipborne acoustic, airborne lidar, and land-based imaging techniques, are limited because of high operational costs, environmental constraints, and difficulties and hazards of working in remote and dangerous places.

Multispectral remote sensing offers the potential to significantly shrink the white ribbon. Even before the launch of Landsat 1, in 1972, researchers were contemplating how to use airborne multispectral data to better understand shallow water environments (Polcyn and Rollin, 1969). With the launch of the Landsat series of satellites and the ensuing host of spaceborne multispectral platforms, including the Copernicus Sentinel-2 satellites, algorithms for generating bathymetry from high- and moderate-resolution satellite imagery data have proliferated. Multispectral satellite derived bathymetry (SDB) spans a diverse spectrum of techniques, including analytical methods based on radiative transfer theory, empirical methods based on the attenuation of light as defined by the Beer-Lambert Law, and statistical methods including ensemble learning and artificial neural networks (ANNs). The term SDB also encompasses a broader category of spaceborne techniques including methods based on wave kinematics and photogrammetry, but this dissertation focuses on empirical spectral-based SDB.

Popular empirical multispectral SDB algorithms include linear multiband regression, band-ratio transforms, and depth of penetration (DOP) zones, along with numerous variations incorporating geographically adaptive coefficients and optimization techniques. Although these techniques have been used extensively in specific case studies and are being considered by various hydrographic offices to supplement regional-scale bathymetric databases, their applicability on a global scale is limited by the availability of in situ reference depths, particularly in remote and difficult-to-map areas. In addition to relying on available reference data, most empirical SDB methods use single images, which can result in significant errors or missing data resulting from ephemeral water-column, surface, and atmospheric

conditions, such as sediment plumes, algal blooms, and clouds. A growing number of studies are exploring multitemporal methods using multiple images, but they generally rely on only a handful of images and do not leverage frameworks capable of supporting entire time series of multispectral imagery. Another drawback of existing empirical SDB approaches is the absence of uncertainty estimates of the spectral data used to derive bathymetry. In general, uncertainty has received little attention in the SDB literature, with only a few recent studies addressing the topic beyond the traditional RMSE statistic, which conflates the uncertainties of the multispectral data and reference bathymetry.

This dissertation presents two spaceborne empirical multispectral remote sensing SDB methods to address shortcomings of existing SDB approaches and reduce the global shortage of nearshore bathymetry data – (1) active/passive spaceborne data fusion combining either MABEL or ICESat-2 ATLAS and multispectral data and (2) state space modeling of Sentinel-2 and Landsat 8 multispectral data to generate gap-free models of relative SDB (rSDB) with corresponding uncertainty estimates.

Active/Passive Spaceborne Data Fusion

The recently launched Ice and Land Elevation Satellite-2 (ICESat-2) mission offers an opportunity for a completely spaceborne data fusion approach to nearshore bathymetry by potentially providing a global source of nearshore reference depths to tune empirical multispectral SDB algorithms. The primary objectives of ICESat-2 are to measure ice-sheet elevations, sea-ice thickness, and global biomass (Abdalati et al., 2010), but the 532-nm (green) wavelength photon-counting Advanced Topographic Laser Altimeter System (ATLAS), the sole instrument onboard ICESat-2, was posited (Forfinski-Sarkozi and Parrish, 2016), and has since been shown (Parrish et al., 2019), capable of detecting bathymetry in certain nearshore environments. ATLAS data are acquired along narrow tracklines, but any detected bathymetry could be used to infer depth over a much broader area by synergistically fusing the active lidar data with passive multispectral imagery using empirical SDB algorithms. The active/passive spaceborne data fusion method was presented in two studies in anticipation of the launch of ICESat-2, which occurred just prior to the publication of the second study. As such, the data analyzed in these publications are not from ICESat-2 but from the Multiple Altimeter Beam Experimental Lidar (MABEL), NASA's high-altitude ICESat-2 simulator system, which was designed to provide ATLAS-like data for concept verification and algorithm development.

Analysis of Mabel Bathymetry in Keweenaw Bay and Implications for Icesat-2 Atlas

The goals of this study were to (1) assess the ability to derive bathymetry from MABEL and (2) evaluate the accuracy and reliability of MABEL bathymetry. The first goal was achieved by identifying bathymetric returns in MABEL data acquired in Keweenaw Bay, Lake Superior, and applying a first-order

refraction correction and a vertical datum offset to reduce the ellipsoidally referenced photon returns to the local chart datum. The second goal was achieved by comparing the MABEL-derived bathymetry to a high-resolution bathymetric lidar dataset acquired with a Fugro LADS MKII lidar system. The results indicated that MABEL reliably detected bathymetry in depths of up to 8 m, with a root mean square error (RMSE) of 0.7 m, with respect to the reference data. In addition to demonstrating MABEL's ability to detect bathymetry, this study developed and verified a baseline model to predict numbers of bottom returns as a function of water depth.

Active-Passive Spaceborne Data Fusion for Mapping Nearshore Bathymetry

The goals of this study were to (1) demonstrate a completely spaceborne date fusion approach capable of creating datum-based bathymetry over large spatial extents and (2) assess over which portion of the world's coastal regions the data fusion approach might be viable. The first goal was achieved by synergistically fusing MABEL-derived bathymetry and Landsat 8 multispectral Operational Land Imager (OLI) imagery over Keweenaw Bay, Lake Superior, using the Stumpf band-ratio SDB algorithm to generate bathymetry that agreed with a high-resolution bathymetric lidar dataset to within an RMSE of 1.1 m. The second goal was achieved by assessing the spatiotemporal variability of global costal water clarity as interpreted from Visible Infrared Imaging Radiometer Suite (VIIRS) Kd(490) data. The spatiotemporal viability results indicate that the spaceborne active-passive data fusion approach may be viable for filling the nearshore data void in many regions of the globe over the course of a year.

State Space Modeling for Empirical Multispectral Satellite Derived Bathymetry

State space modeling of empirical multitemporal SDB overcomes limitations of single-image SDB by leveraging the bathymetric signal in multispectral time series to create internally consistent gap-free models of relative SDB (rSDB) for an arbitrary date, enabling SDB for dates affected by missing or noisy data. Characteristically solved using Kalman filtering, state space models (SSMs) generate statistically optimal estimates of a state vector, with corresponding uncertainty estimates. State space approaches are well established in many applications, including navigation, normalized difference vegetation index (NDVI) studies, and certain coastal mapping applications, but are absent in empirical SDB literature. In addition to estimating an underlying state from a single observed time series, SSMs provide a data-fusion mechanism to combine time series from a diverse suite of multispectral sensors. By including an observation equation for each time series, SSMs are able to estimate a single underlying state, expressed by a state equation, from different data sources.

The goals of the final study are to (1) demonstrate the ability of state space modeling to generate gap-free rSDB models from noisy and incomplete individual time series of multispectral data and (2)

demonstrate the ability of state space modeling to fuse rSDB time series from different multispectral sensors. The first goal was achieved by applying separate local level SSMs, consisting of a single observation equation, to Landsat 8 OLI and Sentinel-2 MSI time series. The second goal was achieved by using a single SSM with two observation equations to create a fused Landsat 8 and Sentinel-2 rSDB model. All three SSMs generated internally consistent, gap-free models of rSDB, with corresponding uncertainties. To assess the state space framework, a representative SSM was then transformed to SDB using geographically adaptive transformation parameters derived using a one-to-one correspondence with a high resolution bathymetric lidar data set resampled to match the resolution of Landsat 8 OLI (30 m). The transformed bathymetry agreed with the reference bathymetry to within an RMSE of 0.29 m, which serves as a proxy indicator of the promising performance of the underlying state space framework. The internally consistent fused SSMs show that state space modeling also offers a data-fusion method capable of incorporating time series from a diverse suite of multispectral sensors.

ANALYSIS OF MABEL BATHYMETRY IN KEWEENAW BAY AND IMPLICATIONS FOR ICESAT-2 ATLAS

Nicholas A. Forfinski-Sarkozi
Christopher Parrish

Remote Sensing
St. Alban-Anlage 66, 4052 Basel, Switzerland
2016 8(9), 772

ANALYSIS OF MABEL BATHYMETRY IN KEWEENAW BAY AND IMPLICATIONS FOR ICESAT-2 ATLAS

Abstract

In 2018, the National Aeronautics and Space Administration (NASA) is scheduled to launch the Ice, Cloud, and land Elevation Satellite-2 (ICESat-2), with a new six-beam, green-wavelength, photon-counting lidar system, Advanced Topographic Laser Altimeter System (ATLAS). The primary objectives of the ICESat-2 mission are to measure ice-sheet elevations, sea-ice thickness, and global biomass. However, if bathymetry can be reliably retrieved from ATLAS data, this could assist in addressing a key data need in many coastal and inland water body areas, including areas that are poorly-mapped and/or difficult to access. Additionally, ATLAS-derived bathymetry could be used to constrain bathymetry derived from complementary data, such as passive, multispectral imagery and synthetic aperture radar (SAR). As an important first step in evaluating the ability to map bathymetry from ATLAS, this study involves a detailed assessment of bathymetry from the Multiple Altimeter Beam Experimental Lidar (MABEL), NASA's airborne ICESat-2 simulator, flown on the Earth Resources 2 (ER-2) high-altitude aircraft. An interactive, web interface, *MABEL Viewer*, was developed and used to identify bottom returns in Keweenaw Bay, Lake Superior. After applying corrections for refraction and channel-specific elevation biases, MABEL bathymetry was compared against National Oceanic and Atmospheric Administration (NOAA) data acquired two years earlier. The results indicate that MABEL reliably detected bathymetry in depths of up to 8 m, with a root mean square (RMS) difference of 0.7 m, with respect to the reference data. Additionally, a version of the lidar equation was developed for predicting bottom-return signal levels in MABEL and tested using the Keweenaw Bay data. Future work will entail extending these results to ATLAS, as the technical specifications of the sensor become available.

Introduction

NASA's upcoming Ice, Cloud, and land Elevation Satellite-2 (ICESat-2) mission, with a 91-day repeat period and near-polar orbit (Abdalati et al., 2010), provides a unique opportunity to assess ice sheet elevation change. The sole instrument aboard ICESat-2 will be the Advanced Topographic Laser Altimeter System (ATLAS), a micro-pulse, photon-counting lidar system operating at 532 nm using a frequency-doubled neodymium-doped yttrium aluminum garnet (Nd:YAG) laser (Abdalati et al., 2010; McGill et al., 2013). Although the primary objectives of ICESat-2 will be to measure ice-sheet elevations, sea-ice thickness, and global biomass (Abdalati et al., 2010), the ATLAS design specifications suggest the feasibility of bathymetry retrieval from ATLAS data. If it can be demonstrated that reliable bathymetry estimation from ATLAS is, in fact, possible, this could greatly benefit studies of coastal and inland water bodies, which are often hindered by a dearth of shallow-water bathymetry (NRC, 2004). The fact that

ATLAS is an active remote sensing system makes it of particular interest for bathymetric mapping, since it may be possible to synergistically fuse water depth estimates from ATLAS with bathymetry retrieved from a variety of sources, including passive multispectral satellite imagery (Hamylton et al., 2015; Pe'eri et al., 2013; Stumpf et al., 2003; Taramelli et al., n.d.) , such as from Landsat 8 and Sentinel-2, and synthetic aperture radar (SAR) data (Calkoen et al., 2001; Huang and Fu, 2004; Ludeno et al., 2015; Stewart et al., 2016). Using ATLAS to measure bathymetry and complement other bathymetric techniques is well aligned with NASA's Applied Sciences Program mission to discover innovative and practical uses for Earth observations (*NASA*, 2010). Additionally, the bathymetric mapping capability would represent an important advancement over ICESat-2's predecessor, the original ICESat, which carried the Geoscience Laser Altimeter System (GLAS). While GLAS did contain a green laser, it was designed with a different laser architecture (Yu et al., n.d.) for the secondary mission of measuring optically thin clouds and atmospheric aerosols (Abshire et al., 2005; Krainak et al., n.d.). GLAS used a 1064-nm laser, incapable of penetrating the water column to provide bathymetry, for elevation mapping.

In empirically evaluating the potential to derive bathymetry from ATLAS, a logical place to start is with NASA's airborne photon-counting ATLAS simulator, the Multiple Altimeter Beam Experimental Lidar (MABEL), which has been flown on the NASA Earth Resources 2 (ER-2) high-altitude aircraft on over 50 missions since 2010. It is important to note that MABEL is not an exact model of what ATLAS will be (McGill et al., 2013), but its main purposes are to verify the ATLAS measurement concept and provide data similar to ATLAS data for algorithm development.

In keeping with the above considerations, our long-range research goals are to: (1) assess the ability to derive bathymetry from MABEL; (2) evaluate the accuracy and reliability of MABEL bathymetry; (3) extend the analysis of MABEL data to ATLAS; and (4) (pending the results of the previous phases) develop tools and techniques for bathymetric mapping using fusion-based approaches that leverage ATLAS bathymetry. The motivation for our long-range research program stems from the large number of nearshore, coastal areas around the world for which bathymetric data are entirely lacking, and the need for such data for applications ranging from modeling inundation, due to storm surge and sea level rise, to nautical charting (NRC, 2004). The broad objective of obtaining coastal bathymetry worldwide is entirely aligned with initiatives to manage, expand, and add value to the suite of global bathymetry obtained through a variety of techniques by a number of national and international organizations (EMODNET Coastal Mapping, n.d.; Intergovernmental Oceanographic Commission, n.d.; International Hydrographic Organization - Organisation Hydrographique Internationale (IHO), n.d.; GEBCO, n.d.; US Department of Commerce, n.d.). Due to the challenges of mapping bathymetry in very shallow waters with any one particular technology (NRC, 2004), the synergistic fusion of spaceborne, active sensor bathymetric data with

complementary data sets, including airborne bathymetric lidar, shipborne sonar, airborne and spaceborne multi-and hyperspectral imagery, and synthetic aperture radar (SAR), affords the best option for filling the voids in worldwide shallow bathymetric coverage.

This study presents the results of the first two phases of the long-range research program outlined above. *MABEL Viewer*, a web-application developed in this study to facilitate interactive identification of MABEL bottom returns, was used to identify bathymetric returns in MABEL data acquired over Keweenaw Bay in Lake Superior. To quantitatively assess the quality of bathymetry from MABEL, the identified bottom returns were first corrected using National Oceanic and Atmospheric Administration (NOAA), Great Lakes Coastal Forecasting System (GLCFS) data and a first-order refraction correction. These corrected depths were compared against high-accuracy bathymetry acquired for NOAA with a Fugro Laser Airborne Depth Sounder (LADS) Mk II in 2010. The results show good agreement between MABEL bathymetry and the NOAA reference bathymetry, with a z-component root mean square error ($RMSE_z$) of 0.7 m in water depths of up to 8 m. Concurrently with this analysis, a version of the lidar equation was developed for predicting the number of bottom returns in the data set as a function of depth within the project site. The predictions were compared against the observed data to assess the general validity of our baseline model. We conclude with a discussion of the next steps, including the extension of this work to ATLAS, using simulations generated by project partners at the University of Houston, National Center for Airborne Laser Mapping (NCALM).

Bathymetric Lidar Background

Almost as old as the laser itself, airborne lidar (light detection and ranging) has its roots in the mid-1960s. The reader is directed to Guenther (Guenther, 2007) and Petrie and Toth (Petrie and Toth, 2009) for a detailed history of airborne lidar remote sensing, including the first practical demonstration of the capability of measuring depth in 1969 (Hickman and Hogg, 1969). Lidar technology evolved rapidly over subsequent decades, leveraging developments in enabling technologies, including inertial and satellite navigation systems (Guenther, 2007; Petrie and Toth, 2009). Conventionally, lasers operating in the near infrared (typically, 1064 and 1550 nm) have been preferred for topographic lidar, while bathymetric lidar has used water-penetrating 532 nm lasers, sometimes in combination with 1064 nm for obtaining water surface returns and simultaneously mapping topography. Industry-standard bathymetric lidar systems include the Optech Scanning Hydrographic Operational Airborne Lidar Survey (SHOALS) system and Coastal Zone Mapping and Imaging Lidar (CZMIL), Leica Airborne Hydrography AB (AHAB) Chiroptera II and HawkEye II and III, National Aeronautics and Space Administration (NASA) Experimental Advanced Airborne Research Lidar (EAARL), United States Geological Survey (USGS) EAARL-B, and Fugro LADS Mk II and Mk 3 (Guenther, 2007; Pack et al., 2012; Quadros, 2013). Even more varied than

the number of systems are the applications of these systems, including benthic habitat classification (Miller et al., 2016; Tulldahl et al., n.d.; Wedding et al., 2008; Zavalas et al., 2014), shoreline delineation (Pe'eri et al., 2011), inundation modeling (Chamberlin and Arcas, 2015), river morphodynamics (Mandlburger et al., 2015; McKean et al., 2014), geomorphological mapping (Finkl et al., 2005; Houser et al., 2015; Kennedy et al., 2014), and hydrography (Guenther, 2007; Irish and Lillycrop, 1999; Kinzel et al., 2007). The conventional bathymetric lidar systems listed above are all waveform resolving, meaning they record and/or analyze in real time digitized, backscattered pulses containing up to thousands of photons.

In the topographic lidar community, an emerging technology is photon-counting lidar, which uses either photomuliplier tubes (PMTs) or avalanche photodiodes (APDs) operated well above the breakdown voltage (i.e., in Geiger mode) to record returns as low as a single photon as individual points. The low power consumption of photon-counting lidar systems, which also have low signal-to-noise ratios (SNR), make them ideal systems for spaceborne platforms with strict power budgets. However, photon-counting lidar systems, despite first being identified as a potential mapping technology in 1996 (Priedhorsky et al., 1996), have received considerably less attention in the ocean and coastal mapping community. Only with advances in photon-detector ranging resolution and dead time have photon-counting systems become viable mapping tools (Degnan, 2002). A number of recent publications target terrestrial and cryospheric applications, such as canopy extraction (Awadallah et al., n.d.; Herzfeld et al., 2014; Moussavi et al., 2014) and sea-ice and glacier profiling (Brunt et al., 2016, 2014; Farrell et al., 2011; Kwok et al., 2014), and noise-filtering techniques (Horan and Kerekes, n.d.; Magruder et al., n.d.; Wang et al., 2016), but research pertaining to using photon-counting lidar for bathymetric mapping remains limited.

Examples of photon-counting systems that have been shown to detect bathymetry are the Coastal Area Tactical-mapping System (CATS) (Shrestha et al., 2012) and the NASA Airborne Multi-kilohertz Microlaser Altimeter Instrument (Degnan, 2002). MABEL has also been shown to detect bathymetry, in the low-turbidity waters of Lake Mead and depths of up to approximately one Secchi depth (Jasinski et al., 2016). Focused primarily on the retrieval of water surface height statistics, Jasinski et al. (2016) includes a brief qualitative discussion of depth profiles observed in the photon-elevation data. However, the study did not account for index-of-refraction and vertical-datum corrections or include a quantitative comparison with existing bathymetry from dedicated bathymetric-mapping instruments. Whereas CATS and the NASA microaltimeter were operational at heights above ground level (AGLs) of 500 to 6,700 m, MABEL is operational at an AGL of up to 20,000 m. A detailed investigation of MABEL, which is flown above 95% of Earth's atmosphere, is, therefore, an important step toward evaluating the possibility of measuring bathymetry from photon-counting, spaceborne lidar.

Lidar Equation

In addition to the empirical analysis, it is also of interest to develop a model for predicting the bottom return signal level, given a specified set of environmental conditions and system parameters. Such a model is not only beneficial for evaluating the expected depth ranges in which bathymetry retrieval might be viable using MABEL, but, in future work, it could be extended to ATLAS, as the final system parameters are made available by NASA. In this study, the expected number of photoelectrons corresponding to bottom (seafloor) returns, n_{bot}, is evaluated using a modified version of the lidar equation in (Cossio et al., 2009):

$$n_{bot} = \eta_q \eta_t \eta_r \frac{E_t}{hv} \rho_\lambda \cos(\alpha_t) \frac{A_r}{\pi (R_{air} + R_w)^2} \left(1 - r_{int}(\alpha_s)\right)^2 T_\lambda^2 e^{-2 c_\lambda R_w}, \quad (1)$$

In Equation 1, h is Planck's constant; v is the photon frequency; R_w is the pulse travel distance in water; R_{air} is the pulse travel distance in air; η_q is the detector quantum efficiency; η_t is the transmitter optical efficiency; η_r is the receiver optical efficiency; E_t is the transmitted energy per channel per pulse; ρ_λ is the bottom reflectance at the laser wavelength, λ; α_t is the incidence angle on the bottom; A_r is the collecting area of receiver aperture; r_{int} is the air-water interface reflectance; T_λ^2 is the two-way atmospheric transmittance; α_s is the local incidence angle on water surface; and c_λ is the effective attenuation coefficient (for which the water column diffuse attenuation coefficient, K_d, establishes a lower bound). The two-way atmospheric transmittance can be further expressed as:

$$T_\lambda^2 = e^{-2 \int_0^H \sigma(z) dz}, \quad (2)$$

where $\sigma(z)$ is the total atmospheric extinction coefficient, at the laser wavelength, as a function of altitude, z, and H is the altitude of the ER-2 aircraft at the time of the MABEL overflight.

Materials and Methods

MABEL Data

In missions spanning from December 2010 to August 2014, MABEL data have been acquired across North America, over a variety of landforms, marine environments, and vegetative regimes, including inland and coastal mountain ranges, Arctic sea ice and ice sheets, prairies, deserts, savannah, and coastal plains. This study focuses on two sites along the "Transit to KPMD" mission (where KPMD refers to the Palmdale Regional Airport, in Palmdale, CA) identified using *MABEL Viewer*, an in-house prototype data-explorer web application built on Python and JavaScript. This custom software tool facilitates examining the existing MABEL data archive by providing a graphical user interface (Figure 1) to select a flight line of interest and interactively view and classify the photon elevation data for each channel. During future phases of the project, *MABEL Viewer* is intended to also serve as an algorithm-development environment and a template for distributing MABEL data.

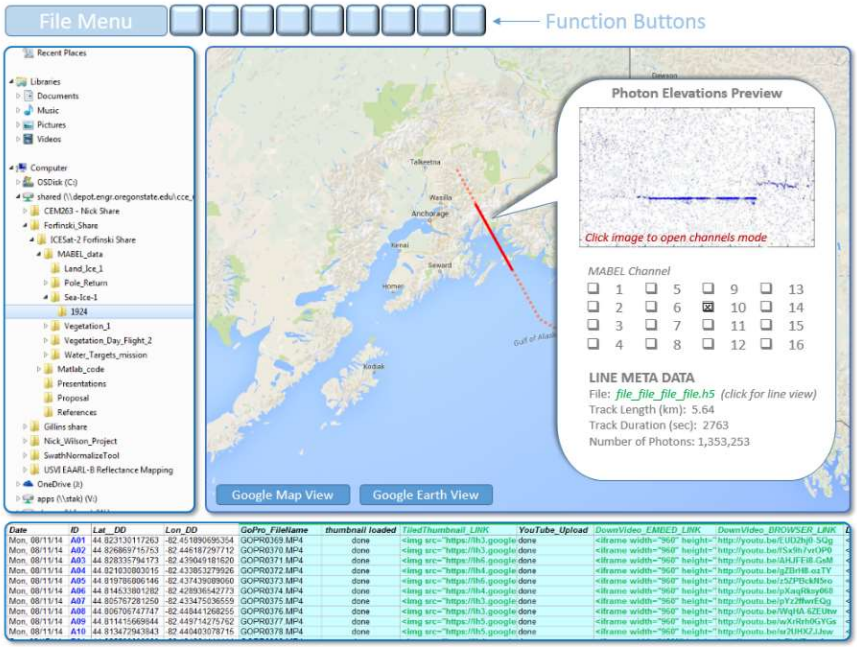

Figure 1. MABEL Viewer prototype interface for interactive identification of bottom returns from the Multiple Altimeter Beam Experimental Lidar (MABEL).

The two study sites are in Lake Superior, at the eastern base of Michigan's Keweenaw Peninsula (Figure 2). No local water-clarity information is available in the study area during the time of data acquisition, but in general, Lake Superior is an optically complex, oligotrophic case 2 water body (Effler et al., 2010). Dominant coastal substrates in the region include high-reflectance white quartz sand derived from Jacobsville sandstone, lower-reflectance gray stamp sands, a product of the region's historic copper mining, and localized cobble fields (Biberhofer, 2002; Kerfoot et al., 2012; Yousef et al., 2013).

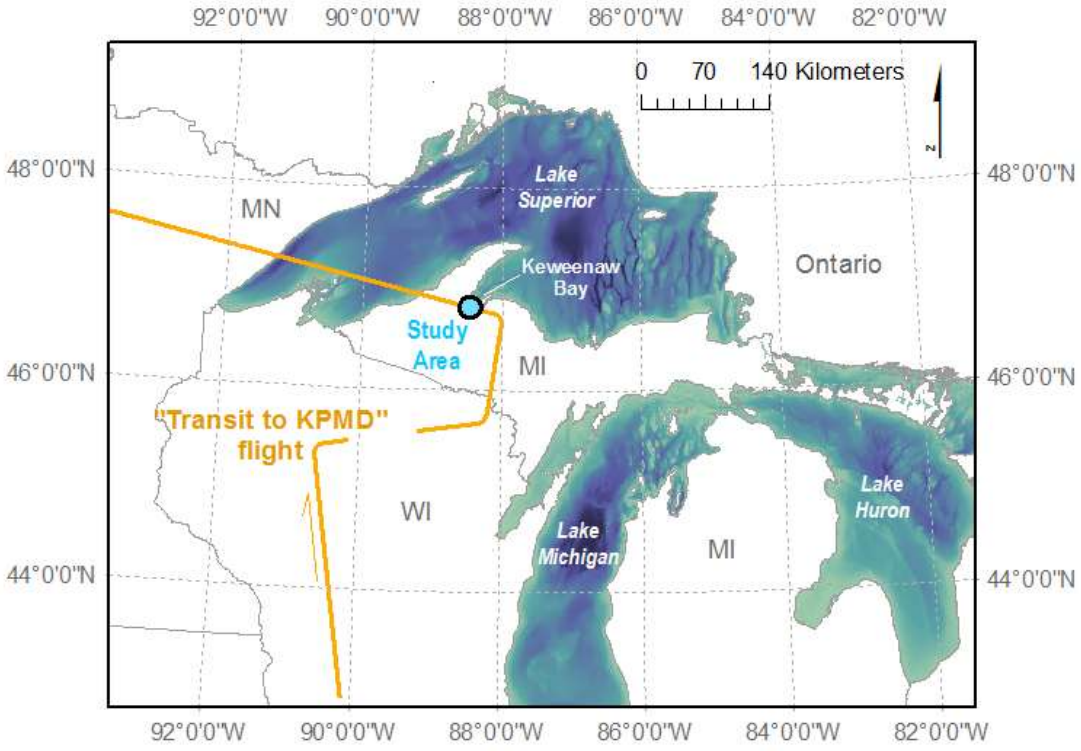

Figure 2. The study site is at the southern end of Keweenaw Bay, Lake Superior, at the eastern base of Michigan's Keweenaw Peninsula.

MABEL has 16 green (532 nm) channels and eight near infrared (1064 nm) channels, with a laser pulse length of 2 ns and an operational laser repetition rate of 5–20 kHz. The geometry of the channels is defined by selecting various fibers within the 215-fiber transmitter and receiver arrays located at the foci of the corresponding matched transmitter and receiver telescopes. This study examines data acquired during the "Transit to KPMD" mission, for which only 13 of the 16 green channels were configured. The corresponding beam angles, elevations, and relative energy levels for this mission are listed in Table 1. Only the green channels are considered in this study because ATLAS will operate only at the green wavelength and because it is the only one of the two wavelengths capable of penetrating the water column to provide bottom returns. At a nominal mission AGL of 20,000 m, the 13 green channels cover a swath of 200 m (Figure 3) and have a nominal footprint of 2 m. The channels corresponding to the anticipated low- and high-energy levels of ICESat-2, as per MABEL metadata, are also listed in Table 1; however, according to NASA, the documented power levels have not been rigorously verified and are affected by a number of environmental factors and configuration procedures (Cook, 2016). To more closely represent the relative energies "as flown", we reclassified the relative ICESat-2 energy level of each channel according to the along-track density of water-surface returns, which was used as a proxy indicator of signal strength. The

energy level for each channel was then linearly scaled based on an assumed channel 6 energy level of 0.2 μJ, a value taken from a previous study examining MABEL data acquired 5 months prior under a similar energy regime (Kwok et al., 2014; Neumann, 2016). The average low and high energy levels were calculated to be 0.04 and 0.2 μJ, up to two orders of magnitude lower than the 5–7 μJ reported in the original design specifications (McGill et al., 2013).

Table 1. MABEL channel specifications for the 13 green channels configured for the "Transmit to KPMD" mission.

Green Channel	Energy Level (metadata)	Energy Level (reclassified)	Angle (mrad)	Elevation (mrad)
1	Low	Low	5.0	−1.5
3	High	Low	−2.2	−0.5
4	High	Low	−0.2	−0.5
5	High	High	−5.0	−1.5
6	High	High	0.0	−1.5
7	Low	Low	1.8	−0.5
8	Low	High	−2.0	−1.5
9	Low	Low	2.2	−2.5
10	High	Low	0.2	−2.5
11	Low	High	2.0	−1.5
12	High	Low	−1.9	−2.0
14	Low	Low	−2.1	−1.0
15	Low	Low	−1.8	−2.5

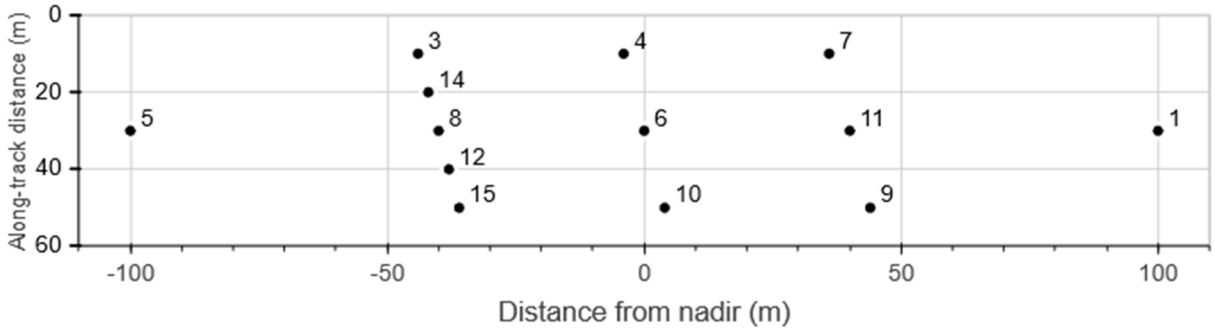

Figure 3. Thirteen green channels were configured for the MABEL "Transit to KPMD" mission. The graph shows the across- and along-track distances for each channel, given a nominal operational height above ground level (AGL) of 20,000 m.

The MABEL data were directly georeferenced with a NovAtel GPS-aided inertial navigation system (INS) (Brunt, 2016). The MABEL trajectory and photon-elevation data, available from the online L2A product data archive, are relative to the WGS84 (G1674) ellipsoid, having been processed in NovAtel Inertial Explorer with a PPP (precise point positioning) post-processing paradigm, using precise ephemeris

data obtained from the International GNSS (Global Navigation Satellite System) Service (IGS) (Brunt, 2016). The roll, pitch, and heading accuracies are documented to be, respectively, 0.007°, 0.007°, and 0.010°. Rotations between MABEL and the inertial measurement unit (IMU) reference frames and between the IMU and the aircraft reference frames are recorded in the MABEL data files.

Figure 4 shows example MABEL data with a distinctive bathymetric profile, along with discernable ground and vegetation returns. Raw photon elevations for each channel from the entire data file are shown in Figure 5. Photon classifications of water-surface and bottom were assigned manually using a classification tool in *MABEL Viewer*. Bottom returns were visually identified via expert knowledge of typical bathymetric profiles, in which the topographic surface can be seen to extend continuously below the water surface to the extinction depth of the lidar. The density of the data relative to ambient noise levels was also considered. The classification scheme shown in Figures 4 and 5 is as follows: red = bottom; dark blue = water surface; light blue = all others (vegetation, land and noise classes).

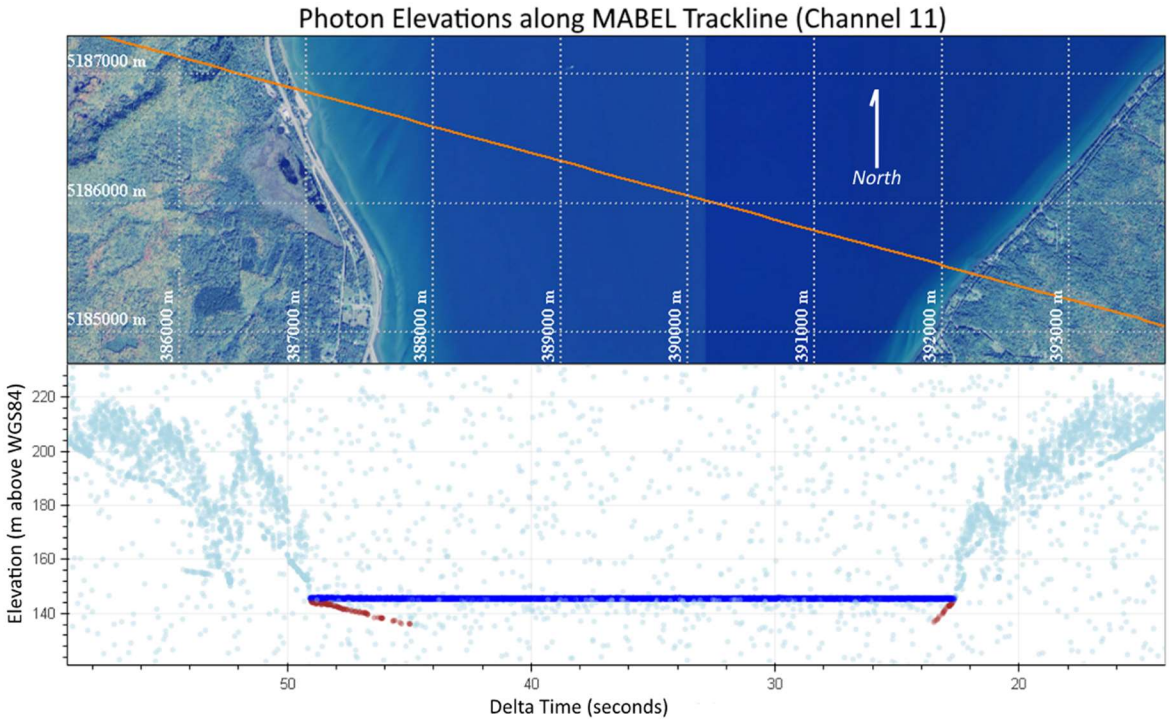

Figure 4. Characteristic water-surface and bottom profiles are clearly discernable in the MABEL data. The delta time on the x-axis is shown in reverse order so that the spatial orientation of the photon elevation data coincides with the 1-m resolution National Agriculture Imagery Program (NAIP) imagery shown above (i.e., viewing the track left-to-right in the above image). In addition to the surface and bathymetric returns, ground and vegetation returns are also discernable in the MABEL photon elevation data. The overlain grid shows World Geodetic System 1984 (WGS84), Universal Transverse Mercator (UTM) zone 16N coordinates.

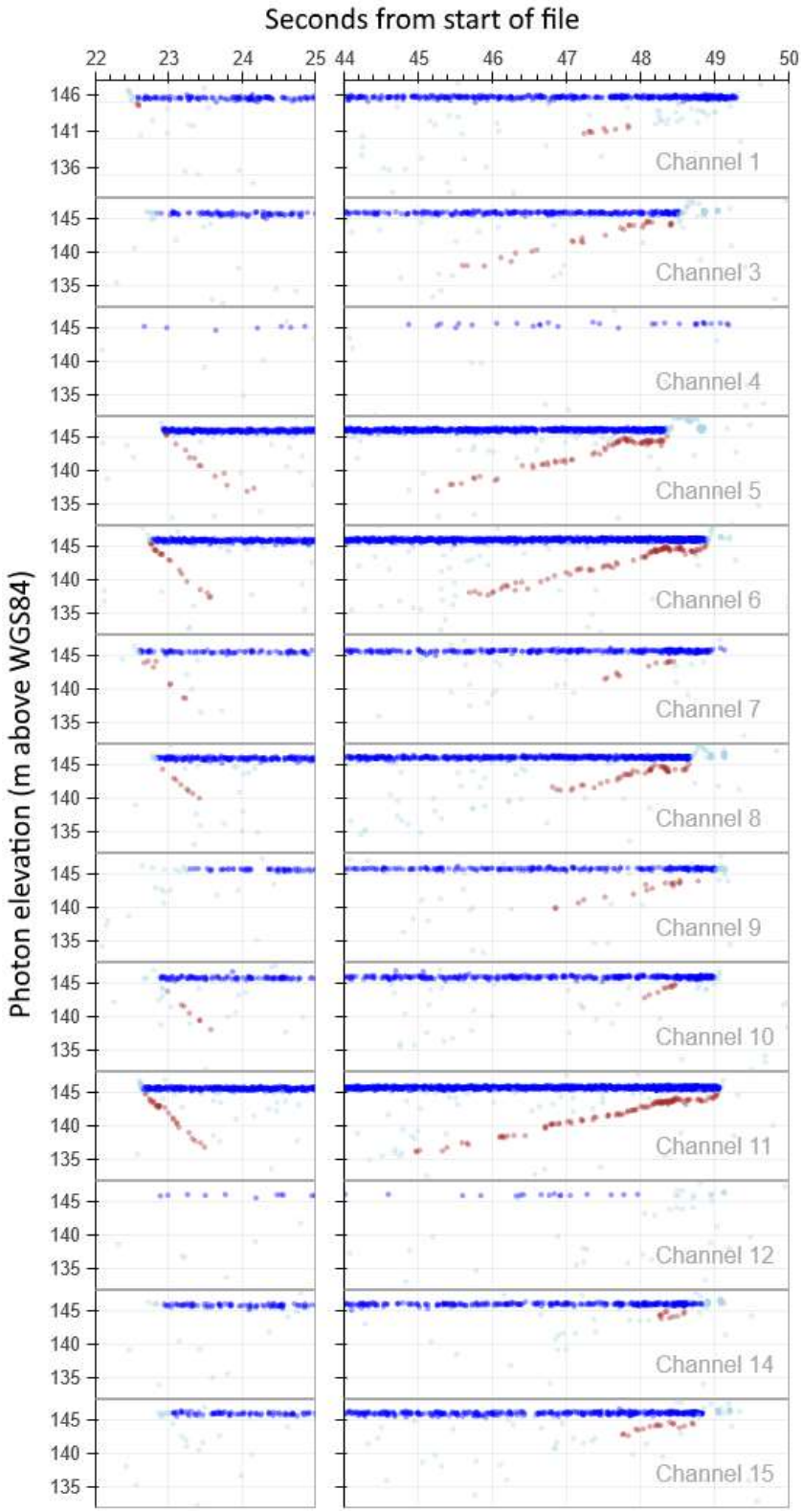

Figure 5. Surface returns (blue dots) and bottom returns (red dots) are shown for each green channel.

Reference Data

The reference data set used in this study was a 2010 NOAA Coastal Services Center data set acquired with the Fugro LADS Mk II airborne bathymetric lidar system (NOAA CSC, 2011). A high-power, full-waveform lidar, the LADS Mk II was operated at an altitude of 365 to 670 m, at 140 to 175 kts, with a pulse rate of 900 Hz and a scan rate of 18 Hz. Horizontal control, referenced to NAD83(CORS96), a realization of the North American Datum of 1983 based on Continuously Operating Reference Stations (CORS), was achieved with a control network consisting of two dedicated GPS base stations and seven CORS. Vertical control, referenced to the International Great Lakes Datum 1985 (IGLD85), was based on water-level data from four NOAA National Water Level Observation Network (NWLON) stations and a co-tidal model. The data set is documented in the distributed metadata as having a horizontal accuracy of 2.97 m and a vertical accuracy, after transformation to the Geodetic Reference System 1980 (GRS80) ellipsoid, of 0.29 m. The average point density was calculated to be 0.27 points per m^2. The data were obtained from NOAA Digital Coast referenced to WGS84 (G1674).

Predicted Number of Photoelectrons

The predicted number of photoelectrons per pulse as a function of depth for each channel was calculated by applying Equation 1. For the purposes of this study, the expected number of photoelectrons given by Equation 1 is assumed to also be the expected number of signal events, given a signal threshold of one photoelectron. The values used in Equation 1 are summarized in Table 2. In order of preference, the values were obtained from: (1) NASA specifications, data sheets and correspondence (nominal energy level, collecting area of receiver aperture, pulse travel distance in air); (2) manufacturer specifications (detector quantum efficiency); (3) typical values for similar systems and environmental conditions obtained from published papers or reports (bottom reflectance); or (4) reasonable, assumed values (optical efficiencies, air-water reflectance, atmospheric transmittance, and effective total beam attenuation coefficient). The values stated in the table are purposefully listed with variable precisions, which reflect our relative level of knowledge of each. Project partners at the University of Houston are concurrently working on more rigorous simulations (Glennie, 2016), which will be continually updated as new/improved system specifications for MABEL and ATLAS become available.

Table 2. Parameter values used in a photon-counting version of the lidar equation to predict the number of photon returns from the bottom. Parameter values are purposefully stated with variable precisions, which reflect our relative level of knowledge of each.

Variable	Value	Unit	Description
η_q	0.18	-	Detector quantum efficiency (Hamamatsu PMT H7260)
η_r	0.4	-	Receiver optical efficiency
η_t	0.4	-	Transmitter optical efficiency
E_t	0.04 and 0.2	μJ	Transmitted energy per channel pulse
ρ_λ	0.3	-	Bottom reflectance at laser wavelength, λ
α_t	0.1	rad	Incidence angle on lake bottom
A_r	0.01	m^2	Collecting area of receiver aperture
R_{air}	20,000	m	Pulse travel distance in air
r_{int}	0.1	-	Reflectance of air-water interface
T_λ	0.8	-	One-way atmospheric transmittance
c_λ	0.25	m^{-1}	Effective total beam attenuation coefficient

The expected numbers of photoelectrons were calculated in 2-D bins extending nominally 20 m along-track and 1-m vertically. Each bin corresponded to 0.1 sec, or 500 laser shots, assuming an operational pulse rate of 5 kHz and speed of 200 m/s. Individual channel track lines were modeled by fitting a curve to the positions of the water-surface returns within each channel. The track lines were projected onto the bathymetric surface defined by the LADS Mk II reference bathymetry, and the average bottom elevation along each bin was used in Equation 1 to calculate the predicted number of photoelectrons for that bin. The average number of expected photoelectrons for each depth range for each channel was then calculated by averaging the populated bins at that depth range. High- and low-energy averages for each depth range were then calculated by averaging the corresponding channels.

Deriving MABEL Bathymetry

The next steps in our analysis focused on the quantitative comparison of MABEL bathymetry against the reference bathymetry. Before the identified MABEL bottom returns were analyzed for bathymetric accuracy and internal consistency, the data were corrected for water-surface refraction and vertically reduced to Lake Superior low water datum (LWD). The full workflow for generating bathymetry from MABEL data is illustrated graphically in Figure 6, and the steps which have not yet been described (i.e., those following the point classification in *MABEL Vi*ewer) are outlined below:

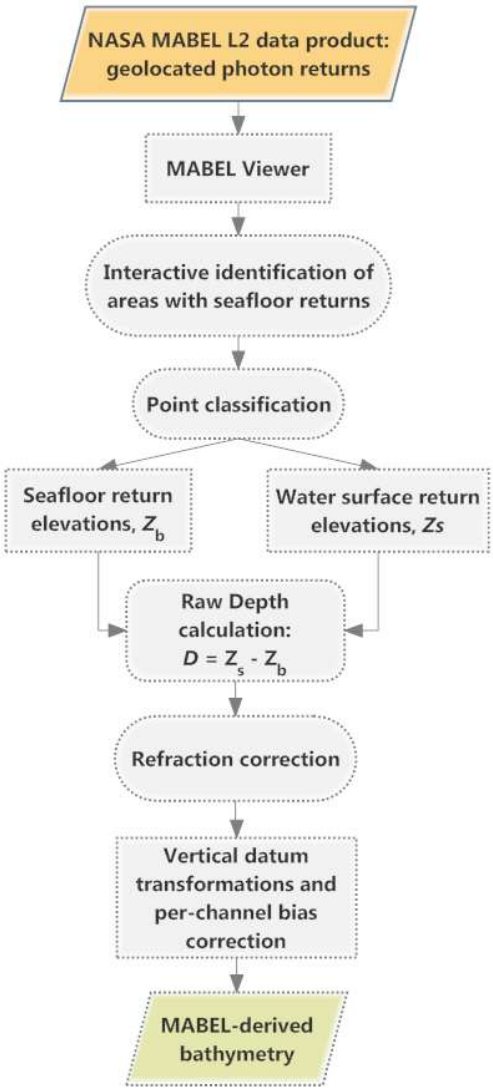

Figure 6. Workflow for generating bathymetry from MABEL data.

Refraction Correction

Because the native MABEL photon-elevation calculation assumes subaerial travel times only, a refraction correction was needed to account for the speed of light in the water column. In this study, a first-order depth correction factor was used, computed as the ratio of the index of refraction of air to that of fresh water, 0.7521. Planimetric corrections (which would require a water surface model for rigorous implementation) were not considered, because the maximum error associated with not applying them (~0.3 m for a 3° angle of incidence in 8 m water depth, assuming a flat water surface and no surface waves) was at the noise level for the purposes of this study. The raw depths were calculated by subtracting each bottom photon elevation from the mean elevation of all the water-surface photons in the corresponding data file.

Vertical Datum Transformation

The raw photon elevations were referenced to the WGS84 ellipsoid. Additional vertical corrections were necessary to account for the observation that the water level as inferred from the surface returns did not match the water level as portrayed by NOAA Great Lakes Environmental Research Laboratory (GLERL) data. The data reduction methodology used in this study incorporates both the traditional hydrographic practice of making water-level corrections based on local water-level observations (Arroyo-Suarez et al., n.d.) and the modern initiative to make "GPS-tide" corrections based on chart-datum—ellipsoid separation models (Dodd and Mills, 2011).

Figure 7 shows the vertical differences between the water-surface as calculated from the surface-return elevations for each channel and the known water level elevation at the time of data acquisition. The average bias is 2.1 m, with a standard deviation of 0.2 m. The source of these channel-specific biases is unknown, but possible explanations include uncalibrated, channel-specific range error and any error in the z-component of the instrument installation lever-arms.

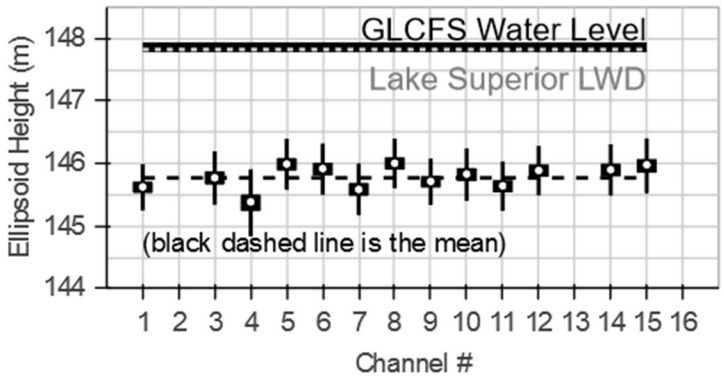

Figure 7. Channel-specific biases were observed in the mean surface elevations. The biases are the differences between the average surface photon elevation and the elevation of the actual water level, as modeled based on a Great Lakes Coastal Forecasting System (GLCFS) water level point query. The range of values for each channel are shown as vertical bars.

The channel-specific biases were calculated by differencing each channel's average surface photon elevation and the elevation of the actual water level as modeled based on a regional Great Lakes Coastal Forecasting System (GLCFS) water-level value (Figure 8). The GLCFS water level, originally referenced to Lake Superior low water datum (LWD), was converted to a WGS84 (G1674) ellipsoid height based on a constant WGS84-IGLD85 separation of 35.38 m, which was derived from a model that was created using VDatum, a vertical datum transformation tool that uses a collection of transformation grids to transform vertically referenced data to and from a number of ellipsoidal, orthometric, and tidal datums (Myers et al.,

n.d.; Parker et al., 2003). Lake Superior LWD is defined as 183.2 m above IGLD85 (NOAA NGS, 2013). The WGS84-IGLD85 separation model, shown in Figure 8, was generated by summing two component separation values at each node of a 100-m resolution 2-D grid: (1) the separation between WGS84 and NAD83 and (2) the separation between NAD83 and IGLD85. The single value used in the GLCFS water-level conversion was calculated by averaging the gridded separation values along the MABEL track line in the project site, the variation of which (σ = 3 cm) was deemed to be insignificant for the purposes of this study.

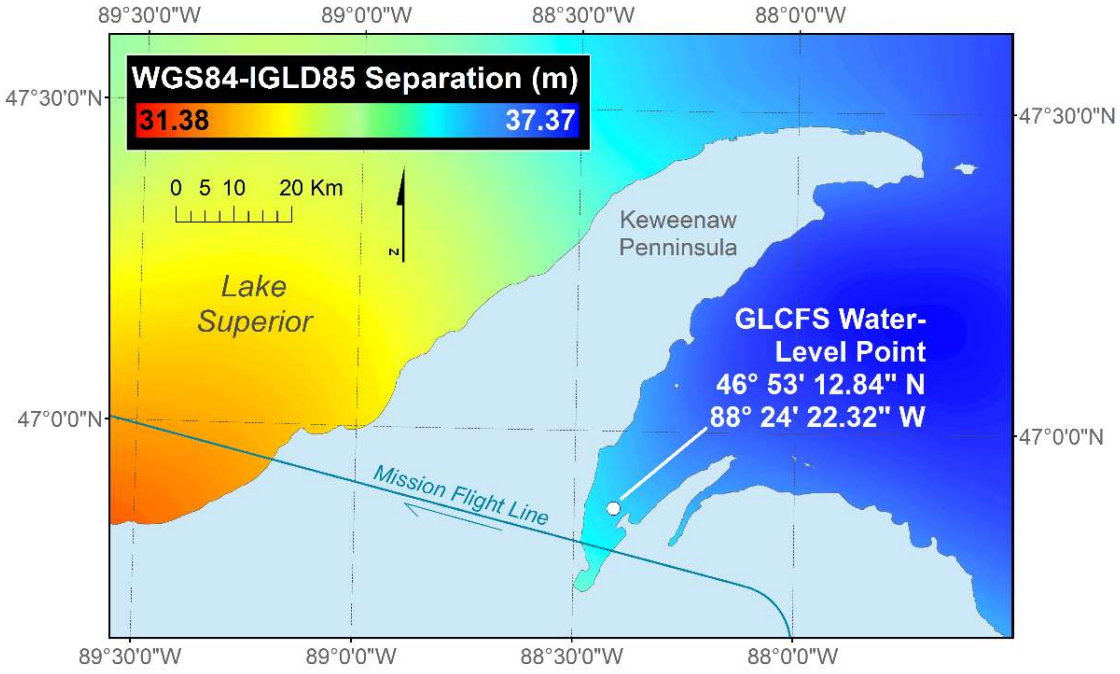

Figure 8. GLCFS water-level data and a WGS84-IGLD85 separation model generated in VDatum, a vertical datum transformation tool, were used to reduce refraction-corrected depths to the WGS84 (G1674) ellipsoid. The datum separation used for this study was 35.38 m, the average separation value along the MABEL track line in the study area.

The vertical reduction methodology is summarized in Figure 9, and the corresponding variables are listed in Table 3. The final ellipsoid elevation for each bottom return was calculated using Equations (3)–(6).

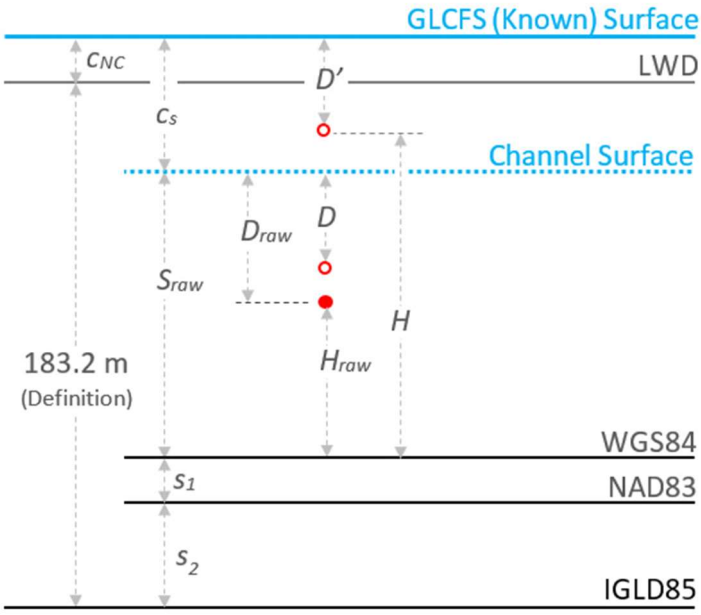

Figure 9. The vertical-control methodology used to reduce the raw bottom photon elevations to WGS84 (G1674) includes traditional hydrographic water-level corrections and modern datum-separation models.

Table 3. Values used to reduce raw bottom elevations to WGS84 (G1674) elevations corrected for index-of-refraction and channel-specific water level biases.

Variable	Description
c_{NC}	GLFCS water level (w.r.t. Lake Superior low water datum)
c_s	Channel-specific water-level bias
$\Delta_{LWD-IGLD}$	Lake Superior LWD - IGLD85 offset (183.2 m, by definition)
S_{raw}	Uncorrected channel water-surface ellipsoid height
D_{raw}	Raw depth (without index-of-refraction correction)
D	Depth (with index-of-refraction correction)
D'	D adjusted vertically for c_s
H_{raw}	Raw photon ellipsoid elevation
H	Final photon ellipsoid elevation
s_1	WGS84-NAD83 separation
s_2	NAD84-IGLD85 separation
n_{air}	Index of refraction for air
n_{water}	Index of refraction for fresh water

$$c_s = \Delta_{LWD-IGLD} + c_{NC} - (s_1 + s_2 + s_{raw}\,), \quad (3)$$

$$D_{raw} = S_{raw} - H_{raw}, \quad (4)$$

$$D' = D_{raw}\left(\frac{n_{air}}{n_{water}}\right), \quad (5)$$

$$H = S + c_s - D', \quad (6)$$

Results

Predicted Photon Returns

Figure 10 shows the predicted numbers of photoelectrons vs. depth for depths of 0–10 m, for each energy level, based on applying the values in Table 2 to Equation 1.

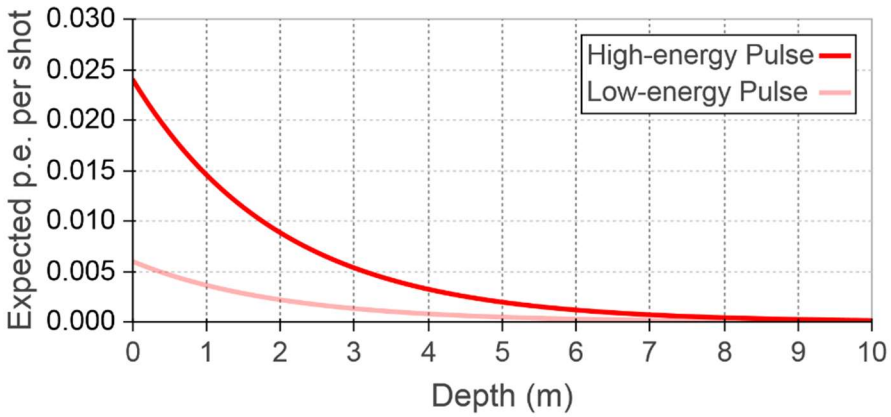

Figure 10. The predicted numbers of photoelectrons per pulse (or shot) vs. depth are shown for each energy level, for the Keweenaw Bay project site.

Figure 11 shows example results, from channel 6, comparing the expected and observed numbers of photoelectrons. The left panel displays the reference depth profile, with the along-track 2-D depth bins, and the derived MABEL depths. The right panel displays the average number of expected and observed photoelectrons per shot bin for each depth range.

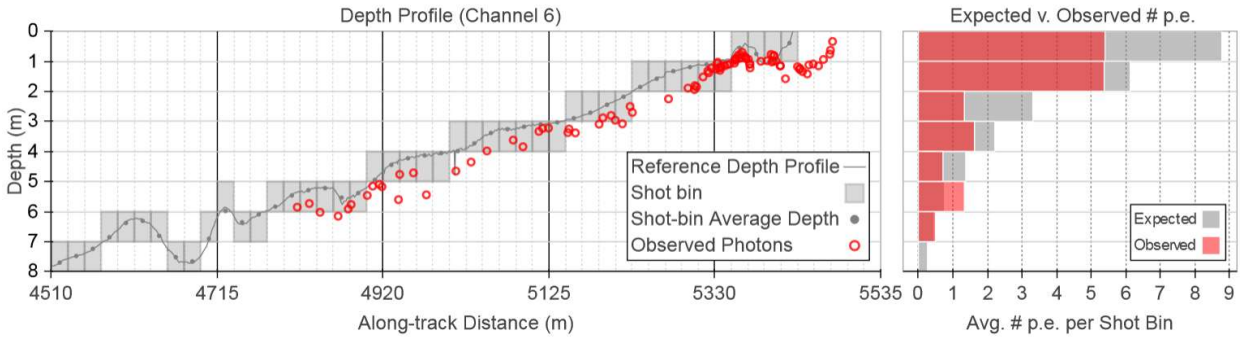

Figure 11. Left: A portion of the depth profile from channel 6 illustrates the comparison between the observed photon returns and the reference Laser Airborne Depth Sounder (LADS) MkII dataset. The expected numbers of photoelectrons (p.e.) for each shot bin was calculated based on the average depth of the shot bin. Right: The corresponding (channel 6) average expected and observed numbers of photoelectrons for each depth range were calculated by averaging the respective values from the populated shot bins in that depth range.

Figure 12 summarizes the average corresponding numbers of expected and observed photoelectrons per pulse for each energy level. Table 4 lists the corresponding values. Overall, the number of observed photoelectrons decreases with increasing depth at a decay rate similar to the expected numbers of p.e. for each energy level. One noticeable exception is the relatively low number of observed photoelectrons in the 0–1 m depth range for both the high and low energy channels. This is not unexpected, as the shallow nearshore zone generally poses challenges for all bathymetric lidar systems (Pe'eri and Philpot, 2007; Quadros et al., 2008; Tuell et al., n.d.). The challenges associated with this depth range stem from a number of environmental factors in the surf zone, such as breaking waves, the associated bubbles, foam, and re-suspended sediment, which are often unavoidable. (As an aside, an additional challenge with waveform-resolving lidar systems in this very shallow depth range is that the convolution of the laser pulse with the water surface may result in a broadened pulse in which the bottom return is obscured.) Spatial variability of bottom reflectance, which was assumed to be constant in our model, is also a plausible contributing factor, because, as mentioned in Section 2.1, the region is characterized by high-reflectance natural white sand and lower-reflectance anthropogenic stamp sands that are transported along the coast.

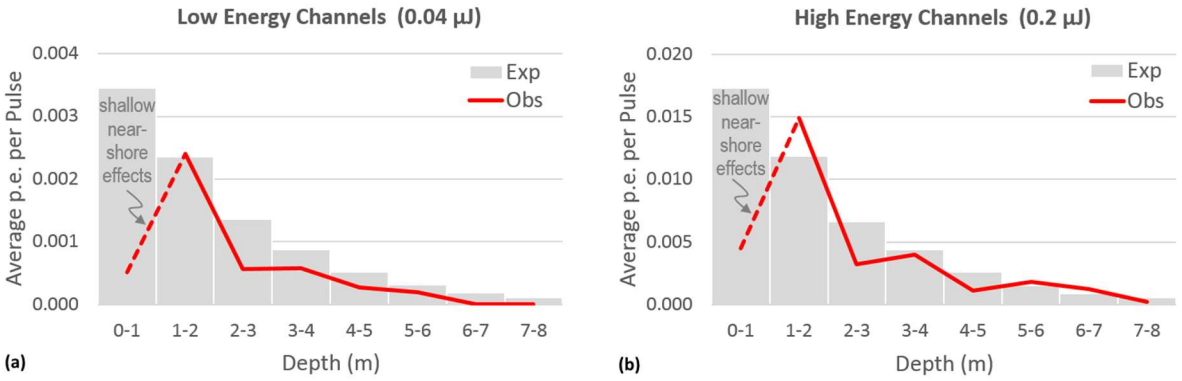

Figure 12. The average observed and expected numbers of photoelectrons (p.e.) are shown for the (a) low-energy and (b) high-energy channels. The results show good qualitative agreement between observed and expected numbers of p.e. in the 1–8 m depth range, but anomalous, shallow, near-shore effects in the 0–1 m depth range, which is typically challenging for bathymetric lidar mapping.

Table 4. Average expected and observed numbers of photoelectrons per pulse for the reclassified low- and high-energy channels, which reflect the "as flown" energy regime.

Depth (m)	**Low Energy Channels (0.04 µJ) (1, 3, 4, 7, 9, 10, 12, 14, 15)**			**High Energy Channels (0.2 µJ) (5, 6, 8, 11)**		
	Expected	***Observed***	***Difference***	***Expected***	***Observed***	***Difference***
0–1	0.003	0.001	−0.003	0.017	0.005	−0.013
1–2	0.002	0.002	0.000	0.012	0.015	0.003
2–3	0.001	0.001	−0.001	0.007	0.003	−0.003
3–4	0.001	0.001	0.000	0.004	0.004	0.000
4–5	0.001	0.000	0.000	0.003	0.001	−0.001
5–6	0.000	0.000	0.000	0.002	0.002	0.000
6–7	0.000	0.000	0.000	0.001	0.001	0.000
7–8	0.000	0.000	0.000	0.001	0.000	0.000

The general (order-of-magnitude) agreement between the expected and observed signal levels both corroborates the observed results and provides an indication that our model produces reasonable estimates, which is important if the model is to be refined and extended to ATLAS in future work. Care should be taken to not over interpret the results of our prediction model, because the transmit energy levels have relatively high uncertainty that is difficult to quantify, given the limitations discussed in Section 2.1. The model suffices for the goals of the current phase of research: namely, it provides a means of assessing the general feasibility of deriving bathymetry from MABEL and developing a baseline model to be refined and extended in subsequent project phases.

Bathymetry Accuracy Assessment

The accuracy of the MABEL bathymetry was assessed by quantitatively comparing elevation differences between the reduced bottom-return ellipsoid heights with the reference bathymetry acquired in 2010 with the Fugro LADS MkII system. A detailed approach resolving uncertainties into vertical and horizontal components was not pursued because well-defined discrete features to use for planimetric positional comparisons were not discernable in the sparse photon data; however, we suspect that the MABEL photon positioning contains a horizontal or angular bias because the positioning of the shoreline relative to the channel track lines, which extend landward of the coast, suggests a nominal southwestward offset of the MABEL photon returns. The comparison was performed with the reduced ellipsoid heights and not the calculated depths to avoid introducing errors associated with additional vertical datum transformations. Differences were calculated for all photon returns classified as bottom, including the returns positioned up to 35 m outside of the extents of the reference data due to the suspected horizontal or angular bias.

The distribution of differences between the bottom-return ellipsoid heights and the ellipsoid heights of the nearest reference bathymetry data points, as found by a *k*-d tree nearest neighbor search, are shown in Figure 13. With an overall bias of -0.59 m, the two datasets agree to within an RMS difference of 0.74 m. Numerous factors could explain the general trend of the MABEL-derived depths being generally deeper than the reference surface, including depth and vertical-datum biases in the reference bathymetry and the suspected horizontal bias in the MABEL photon positioning. Conversely, the observed bias may also include a systematic underestimation of depth resulting from the possible penetration of "surface returns" into the upper portions of the water column (Guenther et al., n.d.). A small, slope-induced high depth bias is also possible due to the LADS MKII system having a slightly larger footprint (nominally 2.5 m) than MABEL (2 m). A change in actual bathymetry over the intervening two years is also a likely factor, as the project area is characterized by dynamic bedform features, including nearshore sand bars and troughs and offshore shoals likely influenced by migrating sand (Ward, 2016). The sedimentary regime of Keweenaw Bay has not been fully described, but a key regional sedimentary process occurring along the northern reaches of the Bay is the southwestward long-shore movement and deposition of stamp sands, which eventually migrate laterally to coalesce with deeper, larger bars (Kerfoot et al., 2012; Yousef et al., 2013). Keweenaw Bay's exposure to an approximately 230-km northeasterly fetch could also play a significant role in the sediment dynamics of the project area (Biberhofer, 2002).

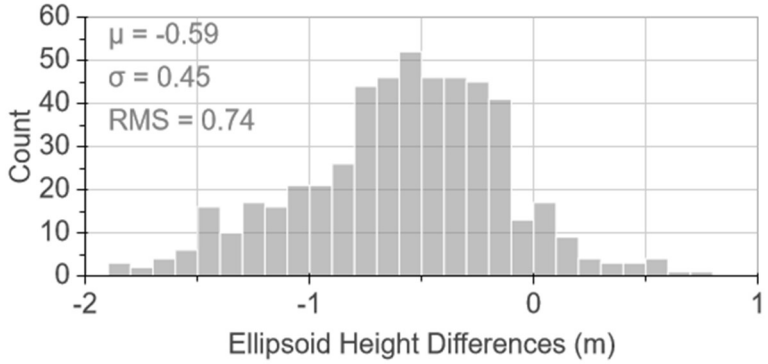

Figure 13. The distribution of differences between the ellipsoid heights of the detected bottom photons and the nearest reference depth has a root mean square (RMS) error of 0.74 m.

Figure 14 shows the spatial variability of the ellipsoid-height differences plotted over 1-m resolution NAIP imagery. Nearshore clusters of positive and negative differences are consistent with the combined effects of migrating sand bars and the suspected horizontal bias. Although the imagery does not temporally coincide with the MABEL and reference data, it offers insight into the observed spatial distribution of the ellipsoid height differences by revealing the dynamic geomorphological nature of the project area.

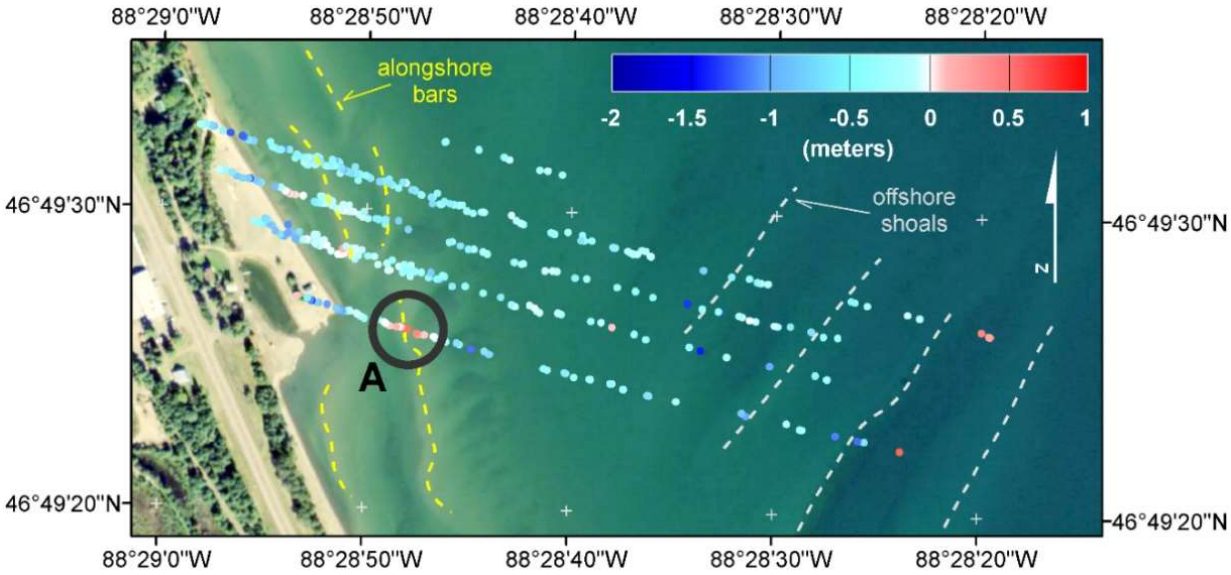

Figure 14. The spatial distribution of ellipsoid-height differences at the western edge of the project area are plotted over 1-m resolution NAIP imagery. Blue colors (negative numbers) represent MABEL depths that are deeper than the corresponding reference depths, and Red colors (positive numbers) represent MABEL depths that are shallower than the corresponding reference depths. Clusters of differences, such as the one highlighted with the black circle labeled 'A', are consistent with a sand bar that has migrated and/or the horizontal positioning error of a sand bar that has not migrated. Certain geomorphological features are labeled to aid interpretation of the background imagery.

Discussion

As noted earlier, MABEL is not intended to be an exact replica of ATLAS. Table 5 lists some of the significant parameter differences between the two sensors.

Table 5. Comparison between MABEL and future Advanced Topographic Laser Altimeter System (ATLAS) system parameters. Note: the values in parentheses in the MABEL pulse energy field denote the reclassified, "as flown" energy levels, as opposed to the original design specifications.

Parameter	MABEL	ATLAS
Laser footprint ($1/e^2$)	2 m (100 µrad)	15 m (31 µrad)
Field of View	4.2 m (210 µrad)	41 m (83 µrad)
Laser pulse repetition freq.	5–20 kHz	10 kHz
Pulse energy	5–7 µJ (0.04–0.2 J)	41/160 µJ
Pulse pattern	16 532-nm beams, 8 1054-nm beams	6 beams (3 pairs of 2)
Swath width	2 km (max) (variable)	6 km
Wavelength	532 and 1064 nm	532 nm
Filter width	~150/~400 pm (532/1064 nm)	30 pm
Receiver aperture area	0.013 m^2	0.79 m^2
Operational altitude	20 km	500 km

Many of the parameter values needed to quantitatively assess ATLAS expected signal levels from the bottom in a particular area using Equation 1 are not currently available. However, given the significantly higher pulse energies and receiver aperture, it is reasonable to expect that the depth penetration capabilities of ATLAS will at least equal, if not exceed, those of MABEL. The much greater altitude of the ICESat-2 satellite (as compared with the ER-2 aircraft during the MABEL flights) impacts the reflected beam solid angle, but has relatively little impact on atmospheric transmittance, since the ER-2 operational altitude is already above ~95% of the Earth's atmosphere. The fundamental spatial resolution of ATLAS will also be coarser, given its larger footprint.

If ICESat-2 ATLAS is found to have similar or greater bathymetric mapping capabilities than MABEL, the resulting bathymetric data may be useful for small-scale nautical charting in poorly mapped areas, as well as for inundation and storm surge modeling and related coastal zone management and science needs. Only one, small area was examined in this study, but a preliminary review of the suite of existing MABEL data reveals high-probability returns in other parts of Lake Superior, as well as a location along the Northern Icelandic coast. Additionally, Jasinski et al. (Jasinski et al., in press) noted MABEL bathymetry in Lake Meade. (These data were qualitatively assessed, but not included in the quantitative analysis of bathymetry in this study, due to a lack of available reference bathymetry for the sites.)

Although the observed MABEL and anticipated ATLAS data densities and vertical uncertainties do not approach those of dedicated airborne bathymetric lidar using full-waveform systems, a satellite platform

allows regular data acquisition in remote, poorly mapped areas, where high-resolution bathymetric lidar and shipborne acoustic data are typically scarce or altogether absent. Hence, there are multiple opportunities to acquire data in areas in which there are large seasonal—or even daily—variations in water clarity. Additionally, the repetitive coverage offered by repeat orbits may densify bottom returns and improve SNR.

Another potential application of ICESat-2 bathymetry data is to serve as a constraint in bathymetry retrieval from a variety of synergistic methodologies using various data sources, including passive, multispectral satellite imagery (Gao, 2009; Pe'eri et al., 2013; Stumpf et al., 2003) and synthetic aperture radar (SAR) (Brusch et al., 2011; Huang and Fu, 2004; Ludeno et al., 2015). Imagery-derived bathymetry is inferred from the relative reflectance of different bands (e.g., blue and green), and SAR-derived bathymetry is inferred based on variations of surface roughness. Each of these methods has the advantage of providing dense depth estimates over large spatial extents; however, each method usually relies on "seed depths" typically soundings from nautical charts or lidar surveys (Stumpf et al., 2003) or shipboard sonar data (Hogrefe et al., 2008), to calibrate derived values to meaningful local depths. By providing a more-direct form of depth measurement, MABEL (and, ultimately, ATLAS) bathymetry does not require existing reference soundings. On the other hand, bathymetry from MABEL or ATLAS has the disadvantage of being spatially sparse, as depths are constrained to lie along discrete track lines. MABEL (or ATLAS) bathymetry and bathymetry from multispectral satellite imagery and SAR data are, therefore, highly complementary, such that the fusion of each could potentially combine the strengths and overcome the limitations of each method individually. By providing a nearly seamless transition across the shoreline, ICESat-2 bathymetry is also a natural complement to coastal-mapping applications incorporating infrared, terrestrial lidar (Arsen et al., 2013; Chust et al., 2008; Deronde et al., 2006; Elaksher, 2008; Gilvear et al., 2004; Jones et al., 2010; Lee and Shan, 2003).

Conclusions

MABEL, the airborne simulator for NASA's upcoming ICESat-2 mission, has been shown to detect bathymetry up to 8 meters deep in the oligotrophic waters of Keweenaw Bay, Lake Superior. The depths were derived by applying index-of-refraction and water-level corrections to the raw MABEL photon elevations and were shown to be in good agreement with the NOAA reference data acquired two years earlier. Resolving positional uncertainty into vertical and horizontal components requires further research evaluating system and procedural parameters such as boresight calibration angles and georeferencing settings; and incorporating a thorough index-of-refraction model, accounting for the orientation of the aircraft, the corresponding angle of incidence of each beam relative to the water surface, and a water-surface model. Before MABEL data—and potentially ICESat-2 ATLAS data—can be reliably reduced to specific vertical data with sub-meter accuracy without directly relying on local water-level measurements at the

time of data acquisition, vertical uncertainties resulting from 3-D georeferencing and channel-specific range calculations need to be refined.

In addition to assessing the depth accuracy of the derived MABEL bathymetry through a comparison with a high-accuracy reference dataset, a photon-counting version of the lidar equation was used to predict the number of signal events (taken to be one photoelectron) in 2-D bins along each channel track line. Anomalies in the 0–1 m depth range are consistent with known environmental limitations; and uncertainties in the assumed transmit-energy levels limit the applicability of our results, but the general agreement between the average observed and expected numbers of photoelectrons in the 1–8 m depth range for the low- and high-energy channels substantiates our approach and justifies developing our baseline model in future project phases.

Future research plans include developing an algorithm to automatically classify and process bottom returns from photon-counting lidar data and a corresponding uncertainty model. Research plans also include collaboration with the National Center for Airborne Laser Mapping (University of Houston) to extend this MABEL analysis to incorporate theoretical performance characteristics of the ATLAS sensor.

ACTIVE-PASSIVE SPACEBORNE DATA FUSION FOR MAPPING NEARSHORE BATHYMETRY

Nicholas A. Forfinski-Sarkozi
Christopher Parrish

Photogrammetric Engineering and Remote Sensing
25 Barlow Place, Suite 210
Bethesda, Maryland 20814-2160

ACTIVE-PASSIVE SPACEBORNE DATA FUSION FOR MAPPING NEARSHORE BATHYMETRY

Abstract

In anticipation of NASA's ICESat-2 mission, which will employ ATLAS, a 532-nm photon-counting lidar, we demonstrate a spaceborne data-fusion approach that has the potential to significantly shrink the global nearshore data gap often referred to as the "white ribbon." Bathymetry algorithms relying on multispectral imagery are conventionally limited by the availability of in situ reference depths, particularly in remote or difficult-to-map areas. Therefore, a completely spaceborne approach could greatly extend the usefulness of such algorithms. The approach is tested with data from NASA's airborne ICESat-2 ATLAS simulator, MABEL, and passive optical imagery from Landsat 8 using an existing spectral-ratio algorithm. The output bathymetric data set agrees with high-resolution Fugro LADS MK II bathymetric data to within an RMS difference of 1.1 m. The spatiotemporal variability of areas where this spaceborne data-fusion approach will potentially be useful is evaluated, based on worldwide coastal water clarity as interpreted from VIIRS Kd(490) data.

Introduction

Despite a large variety of remote sensing techniques that measure or estimate water depth (Gao, 2009; Jawak et al., 2015), there remains a global lack of nearshore bathymetry data (IHO, 2018a; NRC, 2004). The hydrographic community has called this data gap the "white ribbon," referring to the corresponding along-shore empty space on many nautical charts (Leon et al., 2013; Mason et al., 2006). Inadequate or nonexistent chart data is particularly an issue in the Arctic, which has seen an increase in ship traffic (NOAA, 2016a), and in the southwest Pacific (IHO, 2018a). The white ribbon affects numerous research domains and coastal-management applications beyond navigation, such as coral-reef studies (Miller et al., 2011), river geomorphology (Legleiter and Overstreet, 2012), reservoir management (Moses et al., 2013), inundation modeling, and broader efforts to generate seamless topographic/bathymetric digital elevation models (DEMs) (Eakins and Grothe, 2014). Even in countries with dedicated coastal-mapping agencies, populating and maintaining coastal bathymetric databases is challenging, given environmental constraints, limited resources, and difficulties and hazards of working in remote and dangerous areas. Global and regional bathymetric datasets do exist, but high-resolution datasets are limited, and much of the global-scale data is derived from altimeter/gravity techniques that have significant limitations in coastal areas (Smith and Sandwell, 2004; Weatherall et al., 2015). These methods generally produce low-resolution (nominally 5- to 100-km spatial resolution) estimates of bathymetry, and, therefore, are unsuitable for many nearshore applications. While these existing methods and data sets are valuable for physical oceanographic studies and analysis over broad spatial extents, our aim is to improve on the accuracy and spatial resolution

in the nearshore domain.

Relying solely on conventional acoustic (i.e., ship- or boat-based echosounder) methods to map the nearshore zone would be expensive and time-consuming, as well as dangerous in the shallowest areas and near reefs, rocks, and other dangers to navigation. According to Weatherall et al. (2015), approximately 900 ship-years of sonar-based acquisition time (ignoring logistics, data processing, and repeat-survey requirements) are needed to map Earth's oceans, with the 0-200 m depth range requiring two thirds of that time. Another technology for bathymetric mapping that merits discussion is airborne bathymetric lidar (ALB). The use of airborne (i.e., airplane- or helicopter-mounted) laser mapping systems extends back at least as far as 1968 and a study done by Hickman and Hogg (1969), but widespread use of ALB only occurred in the 1990s through early 2000s, as GNSS-aided inertial navigation systems (INS) and related technologies matured to the point of facilitating broad, operational use. Current, commercial ALB systems include: CHARTS, SHOALS, CZMIL, HawkEye, Chrioptera I and II, LADS Mk II and III, and the Riegl VQ-880-G. Despite the widespread use of ALB, it remains difficult to deploy—especially in remote regions—and requires significant resources. Hence, it is a great option for localized acquisition, but not feasible as a sole means of filling the nearshore data void. Multispectral remote sensing methods of deriving bathymetry have been appealing ever since the mid-1960s, when Gilg and McConnell, Jr. (1966) considered using spaceborne photography for bathymetric reconnaissance.

Beginning with the first documented spectral-based approach (Polcyn and Rollin, 1969), methods of mapping bathymetry from multi- and hyperspectral imagery have been well established in the published literature. However, a major drawback of most spectrally-based bathymetry retrieval approaches is that they require in situ data, in the form of reference or "seed" depths. This requirement negates the possibility of mapping bathymetry solely from satellite-based data and from using the methods in areas where there are no existing reference soundings. To overcome this limitation, we propose an active-passive spaceborne data fusion approach, leveraging satellite-based lidar and multispectral imagery. (Note that, for purposes of this study, we define data fusion broadly to include any technique leveraging multiple, complementary inputs where each provides some information the others do not (Castanedo, 2013; Elmenreich, 2002)).

Spaceborne lidar (Abdallah et al., 2013), including NASA's ICESat-2 mission (Abdalati et al., 2010), offers the potential to map elevations along repeat/near-repeat tracklines and does not require existing reference data. (Incidentally, ICESat-2 launched while this study was under review, at 6:02am local on September 15, 2018, from Vandenberg AFB in California. As of the time of submitting the revised manuscript, ATLAS data were not yet available.) The sole instrument aboard ICESat-2 is the Advanced Topographic Laser Altimeter System (ATLAS), a 532-nm (green wavelength) photon-counting lidar. The main objectives of ICESat-2 are to measure ice-sheet elevations, sea-ice freeboard, and global biomass, but

ATLAS's green laser makes it a potential candidate for measuring water depth (Forfinski-Sarkozi and Parrish, 2016; Jasinski et al., 2016). However, ICESat-2 ATLAS data will be spatially limited to lie along discrete track lines. The fusion of ATLAS and multispectral satellite imagery, such as from Landsat 8 OLI or Sentinel-2A MSI, may afford the ability to combine the strengths and eliminate the weaknesses of passive (multispectral imagery) and active (lidar) space-based bathymetric mapping techniques and, therefore, to significantly shrink the white ribbon.

While previous work by the research team investigated the feasibility of mapping bathymetry from ICESat-2 ATLAS (Forfinski-Sarkozi and Parrish, 2016), two important research questions remained: (1) Can spaceborne lidar and spaceborne multispectral imagery be fused to overcome the limitations of each and create datum-based bathymetry over large spatial extents? (2) Over which portion of the world's coastal regions might this approach be viable? The present study addresses these two questions through a multi-step approach leveraging a spectral-ratio method of deriving bathymetry from Landsat 8 imagery, combined with data from NASA's airborne ICESat-2 ATLAS simulator, in conjunction with a spatiotemporal assessment of global nearshore water clarity along planned ICESat-2 tracklines. The results indicate that the spaceborne, active-passive data fusion approach may be viable for filling the nearshore data void in many regions of the globe over the course of a year.

Methods

To demonstrate how spaceborne lidar and multispectral optical imagery can be synergistically combined to map depth over large areas, we use the Stumpf (2003) band-ratio method to fuse MABEL-derived bathymetry and a Landsat 8 OLI scene acquired over Keweenaw Bay, Lake Superior. The accuracy of the resulting satellite derived bathymetry (SDB) is compared to a high-resolution bathymetric lidar dataset acquired with a Fugro LADS Mk II. We also assess where this approach might be viable by examining the spatiotemporal variability of global nearshore water clarity along expected ICESat-2 ground tracks as interpreted from VIIRS diffuse coefficient of downwelling irradiance (Kd(490)) data. The spatiotemporal results are presented statistically with standard summary techniques and cartographically in conjunction with established biogeographic water regions as defined by the Marine Ecoregions of the World (MEOW) and Freshwater Ecoregions of the World (FEOW) datasets.

Study site: Keweenaw Bay

The study site is in Keweenaw Bay, Lake Superior, at the eastern base of Michigan's Keweenaw Peninsula (Figure 15). The area of interest (AOI) was defined to be the extents of National Oceanic and Atmospheric Administration (NOAA) electronic navigational chart (ENC) US5MI72M. Generally considered an optically complex case 2 water body, oligotrophic Lake Superior, including Keweenaw Bay,

is characteristically clear (Effler et al., 2010). Regional coastal substrates include high-reflectance quartz derived from Jacobsville sandstone, lower-reflectance gray stamp sands, an anthropogenic product of the region's historic copper mining, and localized cobble fields (Biberhofer, 2002; Kerfoot et al., 2012; Yousef et al., 2013). Characteristic nearshore bedform morphology includes shifting sandbars and alongshore troughs (Ward unpublished data, 2018).

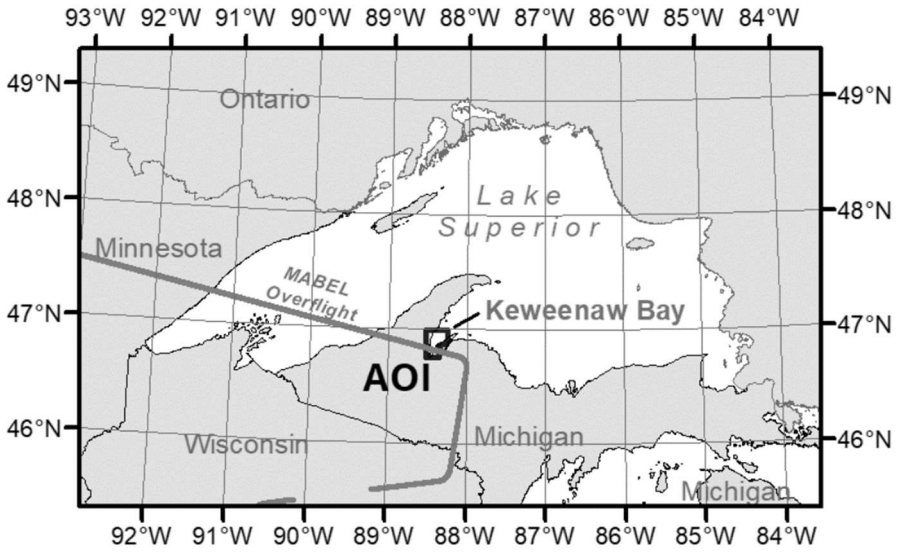

Figure 15. The area of interest (AOI) is in Keweenaw Bay, Lake Superior, where photon-counting bathymetric lidar data were acquired with the ICESat-2 airborne simulator system, MABEL. The extents of NOAA ENC US5MI72M define the AOI, shown by the black polygon.

Data Sets

MABEL

The Multiple Altimeter Beam Experimental Lidar (MABEL) is the airborne simulator for the Advanced Topographic Laser Altimeter System (ATLAS), the sole instrument onboard NASA's ICESat-2 mission (McGill et al., 2013). MABEL has 16 green (532 nm) channels and eight near infrared (1064 nm) channels, the geometry of which is defined by selecting various fibers within the fiber-bundle transmitter and receiver arrays. Originally specified to have low- and high-energy levels ranging from 5 to 7 μJ, MABEL's energy regime has been estimated during certain missions to be up to two orders of magnitude smaller, due to various environmental and operational factors that have degraded the efficiency of the optics over time (Cook unpublished data, 2018). A NovAtel global navigation satellite system (GNSS) -aided inertial navigation system (INS) was used to directly georeferenced the MABEL data. The WGS84 (G1674) trajectory and photon elevation data made available in the online L2A data product archive were processed using a precise point positioning (PPP) paradigm, with precise ephemeris data obtained from the

International GNSS Service (IGS) (Brunt unpublished data, 2018). System configuration metadata, including rotation angles between MABEL and the inertial measurement unit (IMU), are included in the data files.

The MABEL data used in this study were acquired during the "Transit to KPMD (Palmdale Regional Airport, Palmdale, CA, USA)" mission, on September 26, 2012. Only the green channels were used in this study, because ATLAS has only a green laser. Depths were calculated from the L2A data product photon elevations using the approach documented in Forfinski-Sarkozi and Parrish (2016), with one additional corrector. A 70-m (positive to right) across-track, planimetric offset was applied to the depth positions to account for an observed horizontal positional offset likely to be the result of an angular instrument misalignment. MABEL, a concept-verification instrument, was not optimized for pointing accuracy (McGill et al., 2013), and even small misalignments could induce noticeable biases at an operational altitude of 20 km ASL. Moreover, the MABEL data available on NASA's online archive are preliminary, as not all calibrations and corrections have been applied (NASA, 2014). The magnitude of the across-track correction was empirically determined by visually aligning the shoreline geometry observed in the photon-elevation data with the corresponding shoreline geometry observed in high-resolution NAIP imagery of the study area. The PPP method used to create the trajectory data in the L2A data product is unlikely a significant contributor to the observed horizontal offset, because tropospheric error is minimized at MABEL's operational altitude (Brunt unpublished data, 2018).

Landsat 8 OLI

The Operational Land Imager (OLI) instrument onboard the Landsat 8 satellite acquires 30-m resolution, multispectral data in 9 visible (VIS) and near-infrared (NIR) bands (USGS, 2016). OLI's improvements over previous Landsat VIS/NIR sensors include a push-broom configuration (as opposed to whisk-broom), an increased (12-bit) radiometric resolution, and additional coastal and cirrus bands. With a 98.2° inclination sun-synchronous orbit at 705 km altitude and 98.9-min orbital period, Landsat 8 has a repeat cycle of 16 days and an equatorial crossing time of approximately 10:00 AM local time. Landsat 8 imagery data are partitioned into nominally 170-km x 183-km scenes, which are organized according to the Word Reference System 2 (WRS-2), a notation system identifying each image with a path/row designator. As of 2016, Collection 1 Level-1 Landsat data (up-sampled to 16-bit) are placed in one of three tiers, according to processing status and geometric and radiometric quality criteria. The 2013 Landsat 8 OLI imagery used in this study (scene ID LC80240272013254LGN01) was obtained from the Collection 1 Level-1 archive via Earth Explorer (Figure 16). Because a spectral ratio method was used to derive bathymetry from the imagery, radiance and reflectance corrections were deemed unnecessary. Although the image has approximately 43% cloud cover, the AOI is clear. Sedimentary bedforms, including sandbars

and along-shore troughs, are clearly discernable in the imagery.

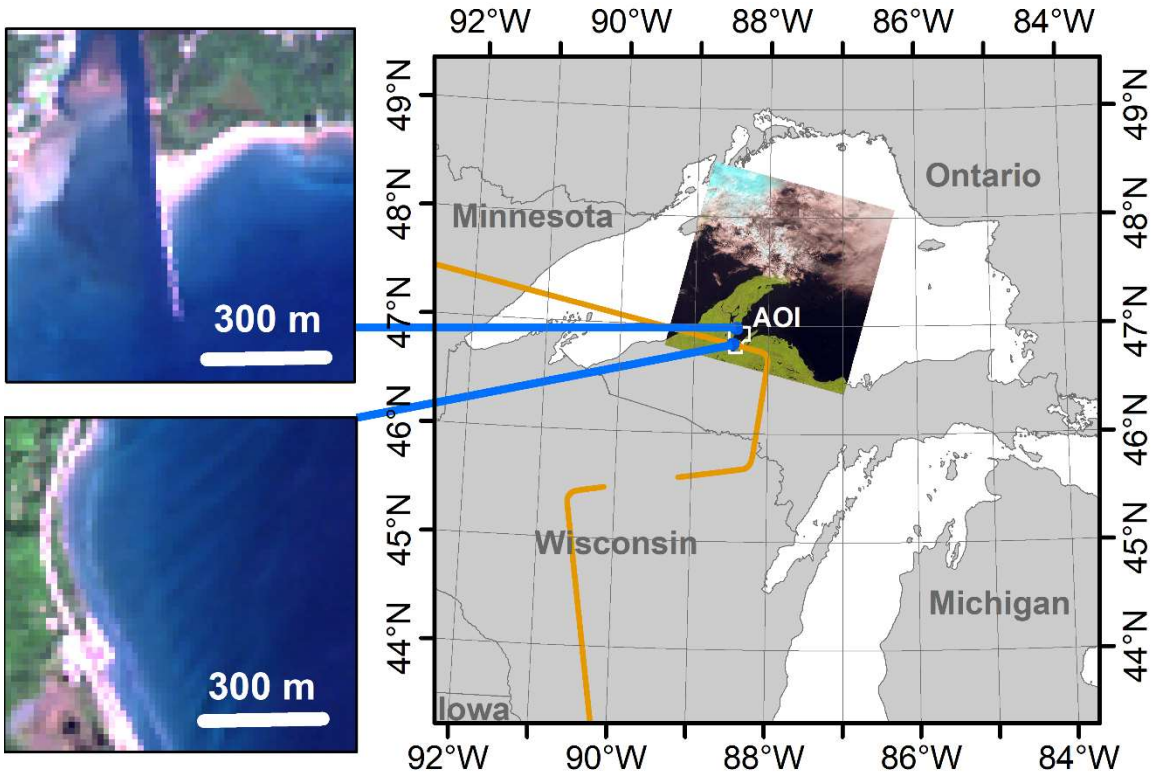

Figure 16. The natural-color Landsat 8 composite shows a cloud-free view of the AOI in Landsat 8 image LC80240272013254LGN01. Sedimentary bedforms are discernable in detail view A, and a dredged channel is discernable in detail view B.

VIIRS Kd(490)

The Visible Infrared Imaging Radiometer Suite (VIIRS) is one of the five payloads onboard the Suomi National Polar-orbiting Partnership (NPP) satellite, which has an orbital period of 101 min. Extending the science of the NOAA Advanced Very High Resolution Radiometer (AVHRR) and the EOS Moderate Resolution Imaging Spectroradiometer (MODIS) sensors, VIIRS is a scanning radiometer acquiring data in the visible and near infrared range that are used in a variety of terrestrial, atmospheric, cryospheric, and oceanic applications (Justice et al., 2013). Data from VIIRS form the basis of a rich suite of data products, including the monthly global Level 3 binned Kd(490) environmental data records (EDRs) used in this study to assess global coastal water clarity (Wang et al., 2016). Generated by the NOAA Center for Satellite Applications and Research (STAR) Ocean Color Science Team, the Kd(490) data are generated using the algorithm developed by Wang et al. (2009), which combines standard techniques for open-ocean waters and a new semi-analytical technique specifically designed for coastal waters. The Kd(490) retrieval algorithm is expressed by Equation 7:

$$K_d^{Comb}(490) = (1 - W)K_d^{Clear}(490) + WK_d^{Turbid}(490) \quad (7)$$

where W is a weighting function bridging the clear open ocean Kd(490) and turbid coastal Kd(490) values. $Kd_d^{Clear}(490)$ is derived from standard Kd(490) models for open oceans, and $Kd_d^{Turbid}(490)$ is derived using Equation 8, which is based on a strong correlation between Kd(490) and the ratio of R(667) and R(488) in turbid waters (Wang et al., 2009):

$$K_d^{Turid}(490) = \frac{c_1}{R(488)} + c_2\frac{R(667)}{R(488)} + 4.18[c_3 + c_4R(645)] \cdot \left\{1 - 0.52\exp\left[\frac{c_5}{R(488)} - \mathrm{c}_6\frac{R(667)}{R(488)}\right]\right\} \quad (8)$$

In extremely turbid waters, where band 667 is often saturated, the ratio of R(645) and R(488) is used. Table 6 lists the constants for the R(667)/R(488) and R(645)/R(488) scenarios.

Table 6. Constants used for calculating turbid coastal Kd(490) values

Constant	R(645)/R(488)	R(667)/R(488)
c_1	-9.785×10^{-4}	2.697×10^{-4}
c_2	0.8321	1.045
c_3	-2.54×10^{-3}	7×10^{-4}
c_4	2.1598	2.7135
c_5	9.19×10^{-3}	-2.533×10^{-3}
c_6	7.81	9.817

It would be possible to apply a conversion from Kd(490) to Kd(532), following the methods in, e.g., Feygels et al. (2017) and de Rada et al. (2012). However, this conversion was not deemed necessary in this work, for the following reasons: 1) from the Jerlov curves for type 1C to 3C waters, the difference between Kd(490) and Kd(532) is approximately 3%, and, while the difference can grow to > 10% for more turbid coastal water types, these waters will be excluded from consideration, due to being too turbid; and 2) as the overall purpose of this assessment is to gain insight into relative water clarity spatially and temporally, corrections that are small and/or approximately constant over the ranges of interest have negligible impact on the analysis.

The VIIRS monthly average Kd(490) data used in this study to assess the spatiotemporal variability of global costal water clarity span one year, from 7/1/2015 to 6/30/2016. Each monthly average map consisted of a tiled set of 24 45°x60° netCDF data files, which were downloaded from the NOAA National Environmental Satellite, Data, and Information Service (NESDIS) Thematic Real-time Environmental Distributed Data Services (THREDDS) server. Two monthly maps had incomplete data coverage. One tile (sector XY) was unavailable for 4/2016, and five tiles (sectors UZ, VZ, YX, ZX, and XY) were unavailable

for 6/2016. Before starting this analysis, an important question that was carefully considered by the research team was whether the relatively coarse-resolution (750 m) Kd(490) data would support a sufficiently detailed analysis of where and when the fusion-based bathymetry retrieval approach would be viable. Detailed visual analysis of the VIIRS Kd(490) data in a number of sites around the world, some of which contained higher-resolution data and/or were familiar to the project team, revealed that the VIIRS Kd(490) data did, in fact, enable analysis of both large regional variations and localized nearshore variations sufficient to assess when and where our spaceborne, fusion-based bathymetric mapping approach might be feasible. Specifically, although the VIIRS Kd(490) data do not generally fill the entire nearshore zone, enough overlap exists to capture alongshore variation over much of the globe, as depicted in the examples in Figure 17.

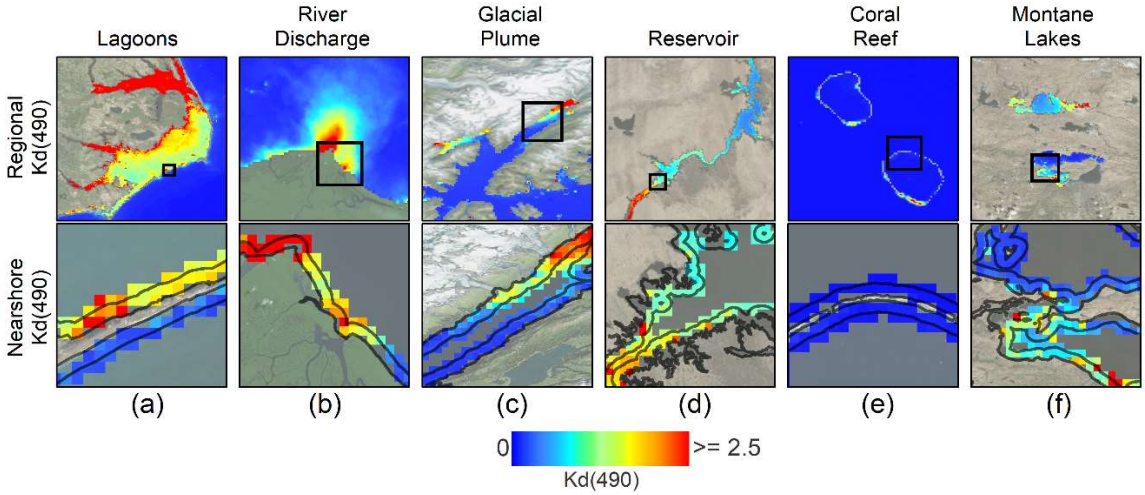

Figure 17. VIIRS Kd(490) data capture nearshore water clarity variability deemed suitable for a global spatiotemporal viability analysis of the presented spaceborne data-fusion approach. The top images show regional variability, and the bottom images show corresponding details of the VIIRS Kd(490) data intersecting the nearshore zone (indicated by black polygons): (a) differences between back-bay and ocean sides of barrier islands along NC, USA; (b) sediment plume at the mouth of Sungai Mamberamo, Papau, Indonesia; (c) glacial-powder plumes in Prince William Sound, AK, USA; (d) variations along Lakes Nasser and Nubia in Egypt and Sudan; (e) predominantly clear waters of the coral-fringed lagoons of French Polynesia; (f) variations among lakes of the Tibetan Plateau.

Reference Bathymetric Lidar Data

The reference data set used in this study was a Fugro LADS Mk II bathymetric lidar data set that was acquired in 2010 as part of a NOAA Coastal Services Center coastal mapping project of Lake Superior (NOAA CSC, 2011). The high-power, full-waveform LADS Mk II airborne lidar system was flown at an attitude of 365-670 m, at 140 to 175 kts, with a 900 Hz pulse rate and an 18 Hz scan rate. Horizontal control, relative to NAD83 (CORS96), was achieved with a control network consisting of two dedicated GPS base

stations and seven Continuously Operating Reference Stations (CORS). Vertical control, relative to the International Great Lakes Datum 1985 (IGLD85), was based on water-level data from four NOAA National Water Level Observation Network (NWLON) stations and a co-tidal model. The associated metadata documents the horizontal and vertical accuracy as 2.97 m and 0.29 m, respectively. The average point density was calculated to be 0.27 pt/m^2. The data were obtained from NOAA Digital Coast referenced to WGS84 (G1674).

Satellite-Derived Bathymetry

A wide variety of multispectral empirical algorithms have been developed and applied to an extensive range of high- and moderate-resolution multispectral sensors (Table 7).

Table 7. Multispectral sensors used in empirical bathymetric data-fusion algorithms, with selected case studies.

Sensor	**Example Case Studies**
MSS (*Landsat 1-4, 5)*	Benny and Dawson, 1983; Lyzenga and Polcyn, 1979; Warne, 1978
TM (*Landsat 4, 5)*	Liceaga-Correa and Euan-Avila, 2002; van Hengel and Spitzer, 1991
ETM+ (Landsat 7)	Hu et al., 2014
OLI *(Landsat 8)*	Deidda et al., 2016; Figueiredo et al., 2016; Pacheco et al., 2015
MSI *(Sentinnel-2a/b)*	Hedley et al., 2012
IKONOS	Fonstad and Marcus, 2005; Mishra et al., 2004; Su et al., 2014
LISS-III *(IRS P6, 1C, 1D)*	Pattanaik et al., 2015; Tripathi and Rao, 2002
Quickbird-2	Conger et al., 2006; Kanno et al., 2011a; Lyons et al., 2011
MERIS	Minghelli-Roman and Dupouy, 2012
MODIS	Fitzpatrick et al., 2014
RapidEye	Giardino et al., 2014
WorldView-2 (3)	Bramante et al., 2013; Collin and Hench, 2012; Hamylton et al., 2015
SPOT 4 (5)	Kao et al., 2009; Liu et al., 2010
GeoEye	Niroumand-Jadidi and Vitti, 2016
ASTER	Ceyhun and Yalçın, 2010; Sneed and Hamilton, 2007

Many empirical algorithms are founded on the Beer-Lambert law (Equation 9), which describes the approximately exponential attenuation of light with increasing depth due to the combined effects of absorption and scattering:

$$E_d(z) = E_d(0)e^{-K_d z}, \tag{9}$$

where $E_d(0)$ and $E_d(z)$ are the irradiances at the surface and depth z, respectively, and Kd is the diffuse coefficient of downwelling irradiance. The relationship given in Equation 10 is often expressed in the following form

$$ln\, E_d(z) = -K_d z + ln\, E_d(0) \tag{10}$$

to emphasize the linear relationship between depth and the natural logarithm of irradiance, which is a key component of many empirical methods. The wavelength-dependent diffuse coefficient of downwelling irradiance is an apparent optical property of water given by Equation 11.

$$K_d = -\frac{d \ln E_d}{dz} = -\frac{1}{E_d}\frac{dE_d}{dz} \tag{11}$$

Equation 11 refers to the theoretical value at in infinitesimally thin layer at depth z, but in practice, K_d often refers to the vertically averaged value over the interval of interest, or $\overline{K}_d$.

A popular variation of the attenuation-based approach is the Lyzenga (2006) method, which itself is an extension of methods by Clark et al. (1987), Lyzenga (1978), and Paredes and Spero (1983), which predict depth based on a linear combination of different bands. The Lyzenga method has in turn been extended numerous times to include, for example, spatial interpolation based on nonparametric regression (Kanno et al., 2011b), geographically adaptive coefficients (Figueiredo et al., 2016; Su et al., 2014), and ordinary block kriging to account for scale differences between point measurements and image pixels. Related approaches include the Jupp (1988) method, which defines 'depth of penetration' (DOP) zones based on depths at which particular wavelengths disappear, and the Stumpf (2003) method, a band-ratio method assuming the ratio of logarithms of band reflectances varies linearly with depth. Extensions of the Jupp and Stumpf methods incorporate, respectively, a stratified genetic algorithm (Gianinetto and Lechi, 2004) and Levenberg-Marquardt optimization (Su et al., 2008). Other statistical methods employ simple regression of single band radiances to reference depths (Fitzpatrick et al., 2014; Legleiter, 2012; Roberts and Anderson, J. M., 1999), polynomial fitting (Hernandez and Armstrong, 2016), artificial neural networks capable of modeling nonlinearities difficult to capture using other methods (Ceyhun and Yalçın, 2010; Liu et al., 2015), supervised classification incorporating inverse probability weighted interpolation of depth estimates from complementary Naïve Bayesian (NB) and neural-network models (Salah, 2016), and unsupervised segmentation (Provost et al., 2004). The diverse methods are summarized in Table 8.

Table 8. Summary of empirical SDB algorithms. Note: this is not intended to be a comprehensive list of algorithms; rather, it is a representative sampling of algorithms representing different categories of approaches.

Method	Study	Comments
	BEER-LAMBERT METHODS	
Linear multiband regression	Lyzenga et al., 2006	Developed version of (Clark et al., 1987; David R. Lyzenga, 1978; Paredes and Spero, 1983)
	Figueiredo et al., 2016	Variation of Lyzenga with geographically adaptive coefficients
	Kanno et al., 2011b	Variation of Lyzenga with generalized coefficients
	Su et al., 2014	Variation of Lyzenga with geographically adaptive coefficients
Band-ratio transform	Stumpf et al., 2003	Simplified ratio approach requiring only 2 inputs
	Su et al., 2008	Variation of (Stumpf et al., 2003) using optimization to calculate coefficients
Depth of Penetration (DOP)	Jupp, 1988	Based on depths of extinction of various wavelengths
	Gianinetto and Lechi, 2004	Variation of (Jupp, 1988) using stratified genetic algorithm
	STATISTICAL METHODS	
Single-band regression	Roberts and Anderson, J. M., 1999	Uses regression between single band DNs and reference depths
Ensemble learning	Manessa et al., 2016	Machine Learning approach using nonlinear Random Forest (RF) regression
Artificial neural network (ANN)	Ceyhun and Yalçın, 2010	Uses ANN with back propagation; can account for nonlinearities
Supervised classification	Salah, 2016	Uses probability weighted interpolation of Naïve Bayesian (NB) and neural-network models
Unsupervised classification	Provost et al., 2004	Uses hierarchical Markovian segmentation

Most approaches incorporate one or more bands from a single image, but Lee et al. (2013) developed a method incorporating multiple images from different viewing angles, and Pe'eri et al. (2016) and van Hengal and Spitzer (1991) investigated multi-temporal analysis of images of the same area acquired at different times to discern anomalous image values due to ephemeral phenomena such as sediment plumes from actual bathymetry. While empirical methods may result in larger errors than analytical methods, the relative simplicity with which they are applied to a diversity of multispectral imagery make them appealing tools when considering deriving nearshore bathymetry on a global scale.

In this work, SDB was generated from Landsat 8 OLI imagery, using a process adapted from the SDB process documented in the General Bathymetric Chart of the Oceans (GEBCO) Cook Book (IHO, 2016), which is based on the empirical Stump (2003) band-ratio method. The relative simplicity of the Stumpf ratio method, which relies on only two parameters and does not require atmospheric correction, facilitates deriving bathymetry on a global scale. The four main steps include masking the land, calculating the ratio of the natural logs of spectral bands, calculating the transform coefficients, and transforming the relative bathymetry to absolute bathymetry. In Step 1, a NIR threshold of 6000 was used to differentiate water pixels from land pixels. In Step 2, the scaling factor, n, was set to 1000. In Step 3, the depths from all enabled MABEL channels were included in a single regression. In Step 4, the relative bathymetry was linearly transformed to absolute bathymetry, with real-world units, by applying the coefficients calculated in Step 3.

Spatiotemporal Usability Assessment

The spatiotemporal variability of areas where the presented active/passive data-fusion methodology would potentially be useful was assessed by analyzing global, monthly averaged VIIRS Kd(490) values along the expected ICESat-2 tracklines within nearshore and shallow coral-reef zones. With the objective of identifying sections of coast and coral reef, not depth-dependent zones, this study broadly defined the coastal zone as a 1-km buffer of the shoreline. (Performing a global depth-dependent shoreline analysis adopting rigorous littoral definitions based on depth of closure and optical properties based on attenuation is hindered by the very lack of nearshore bathymetry that this study aims to address.) The shoreline used in the analysis was the shoreline depicted in the ArcGIS World Water Bodies basemap layer, which included lakes, seas, oceans, large rivers, and dry salt flats (ESRI and Garmin International, Inc., 2017). The shallow coral-reef extents used in the analysis where those defined by the United Nations Environment Programme World Conservation Monitoring Centre (UNEP-WCMC) Global Distribution of Coral Reefs data layer (UNEP-WCMC et al., 2010). The spatiotemporal usability assessment workflow, divided into pre-processing and analysis, is summarized in Figure 18.

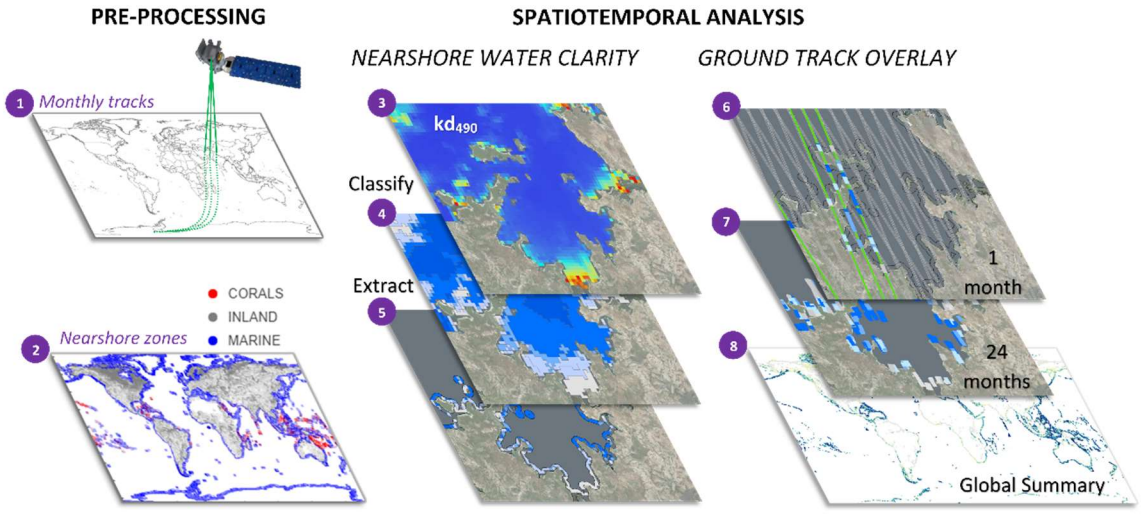

Figure 18. The spatiotemporal viability assessment consisted of data pre-processing and analysis components. In the pre-processing stage, the monthly ICESat-2 ground tracks are identified and the water-bodies and land-masses layers are manipulated through a series of spatial overlay operations to create the 1-km buffer zone taken to represent the nearshore area. In the spatiotemporal analysis, the segments of ICESat-2 ground tracks that overlap the nearshore buffer are intersected with the monthly Kd(490) maps.

Pre-processing

Pre-processing consisted of two steps. First, the ground tracks corresponding to each monthly time period were identified. Second, marine and inland nearshore zones were created through a series of geographic information system (GIS) spatial overlay operations on the input land and water-bodies layers.

Create Monthly ICESat-2 Ground Tracks

Ground track files corresponding to each monthly time period were identified assuming an initial date of January 1, 2019, approximately 2.5 months from the launch of ICESat-2 on September 15, 2018. An exact date and ground track number for when and where ICESat-2 will begin acquiring mission data will depend on operations during a nominal 60-day operations readiness examination period following launch (Magruder unpublished data, 2018). The coordinates for the ground tracks were obtained from kmz files available on the ICESat-2 mission website (NASA, 2018). Each monthly ground track file was created by grouping integer numbers of ground tracks assuming a 91-day repeat cycle, with a 29/29/33 (days) subcycle pattern. Figure 19 shows the ground tracks corresponding to each month, repeat, and subcycle.

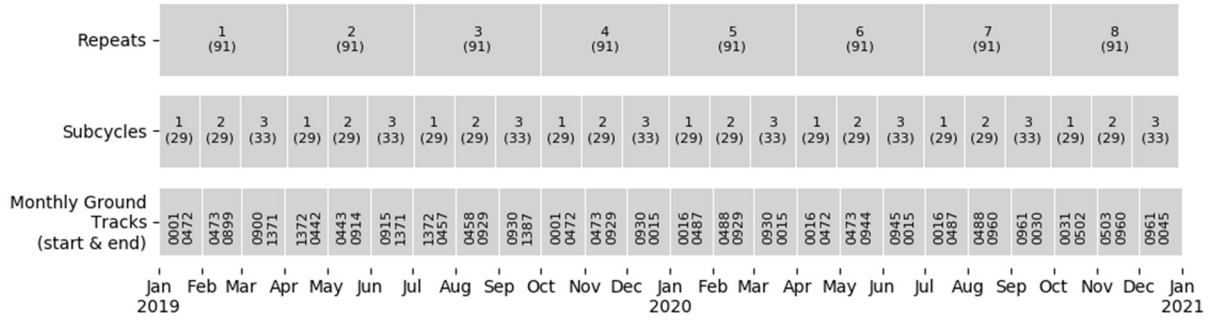

Figure 19. The ground tracks associated with each month were identified by grouping integer numbers of days corresponding to the 29/29/33 (days) subcycles associated with each 91-day repeat cycle. The numbers in parentheses are numbers of days.

Define Nearshore Zones

Defined as a 1-km seaward buffer from marine and inland shorelines, the nearshore zone was generated in two steps. First, the land-masses layer (which did not include the extents of inland lakes and rivers) was intersected with the water-bodies layer to create a land-masses layer portraying the extents of all water bodies. The modified land-only polygons were then buffered to create the nearshore zone. All sections of the nearshore zone were assigned a class of either marine or inland coastal waters, based on the corresponding water-bodies classification.

Spatiotemporal Analysis

The spatiotemporal analysis consisted of first characterizing global nearshore water clarity and then examining the water clarity along the planned ICESat-2 ground tracks. Water clarity was described according to Jerlov's coastal water types, with 0.125, 0.208, 0.365, 0.625, and 1.096 the upper Kd(490) limits for classes J1, J3, J5, J7, and J9, respectively (Solonenko and Mobley, 2015). Global nearshore water clarity was characterized in three steps, using classification and spatial overlay operations in ArcGIS. First, each monthly Kd(490) raster was classified according to the coastal Jerlov water types. Second, the classified raster data were vectorized to create water-class polygons. Third, the water-class polygons were clipped with the pre-processed nearshore-zone polygons. Water clarity along the planned ICESat-2 ground tracks was then characterized by overlaying the monthly ground tracks with each corresponding monthly classified nearshore zone and recording the water type associated with each resulting ground track segment. The monthly nearshore ground track segments were then statistically summarized using standard plotting techniques and a series of hexagonal bin maps portraying different levels of cartographic abstraction. To emphasize the areas most likely to benefit from the proposed spaceborne data-fusion approach, the J1 segments were also summarized in terms of the biogeographic water regions of the MEOW and FEOW classification systems. The boundaries between the MEOW and FEOW regions were modified to be

consistent with the marine, inland, and coral nearshore zones.

Results

Satellite-Derived Bathymetry

Figure 20-a illustrates the regression analysis used to calculate the linear transformation coefficients needed to convert the relative SDB (rSDB) to absolute depths. Relative depths < 1 m were excluded from the analysis because the relative bathymetry did not exhibit a linear relationship with reference depths in the 0-1 m depth range, as seen in Figure 20-a. This breakdown of the linear relationship in the shallowest portion of the depth range has been observed in other studies (Pacheco et al., 2015; Pe'eri et al., 2014) and may be attributable to breaking waves, foam, suspended sediment, and other nearshore environmental conditions that pose challenges for SDB. The spatial distribution of the residuals is shown in Figure 20-b.

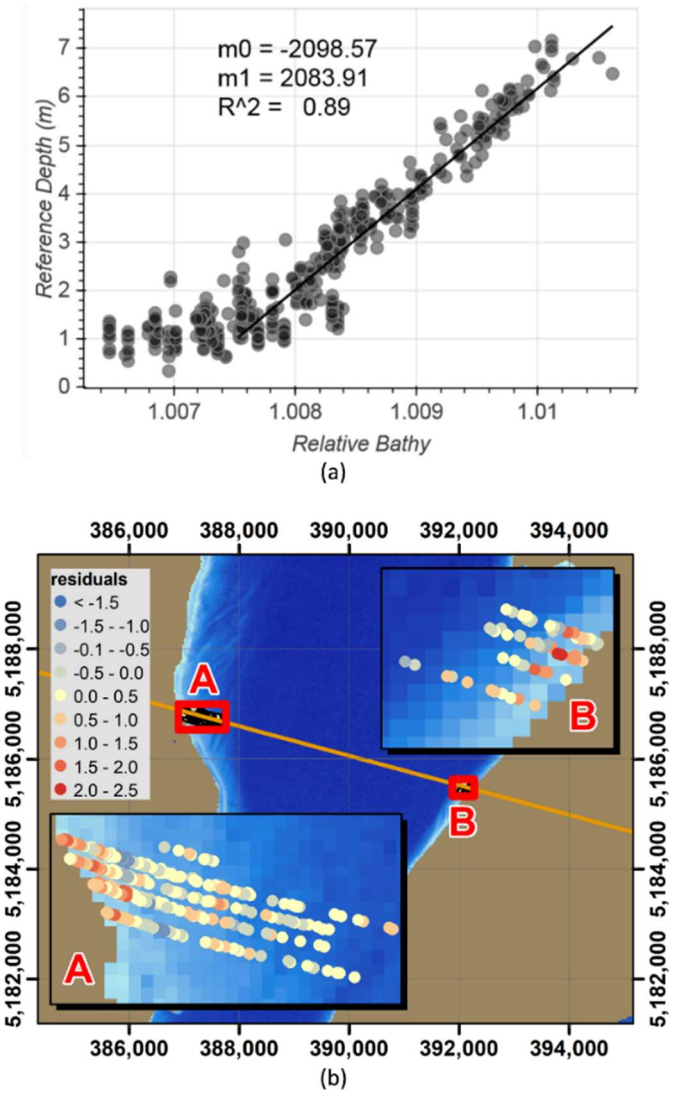

Figure 20. (a) The reference depths are regressed against the relative bathymetry values to derive the coefficients of the linear transformation used to convert relative depths to absolute depths. The linear regression fit has a coefficient of determination of 0.89. (b) The spatial distribution of the regression residuals is plotted over the relative bathymetry. The datum is WGS84 (G1674), and the map projection is UTM Zone 16 N, with units of meters.

A histogram of the distribution of differences between the absolute bathymetry and the reference bathymetry is shown in Figure 21-a. The absolute bathymetry agreed with the high-resolution bathymetric lidar dataset to within an RMS difference of 1.07 m. Figure 21-b shows the spatial distribution of the differences. The largest differences form patterns that are indicative of changing bedforms, due to sediment transport.

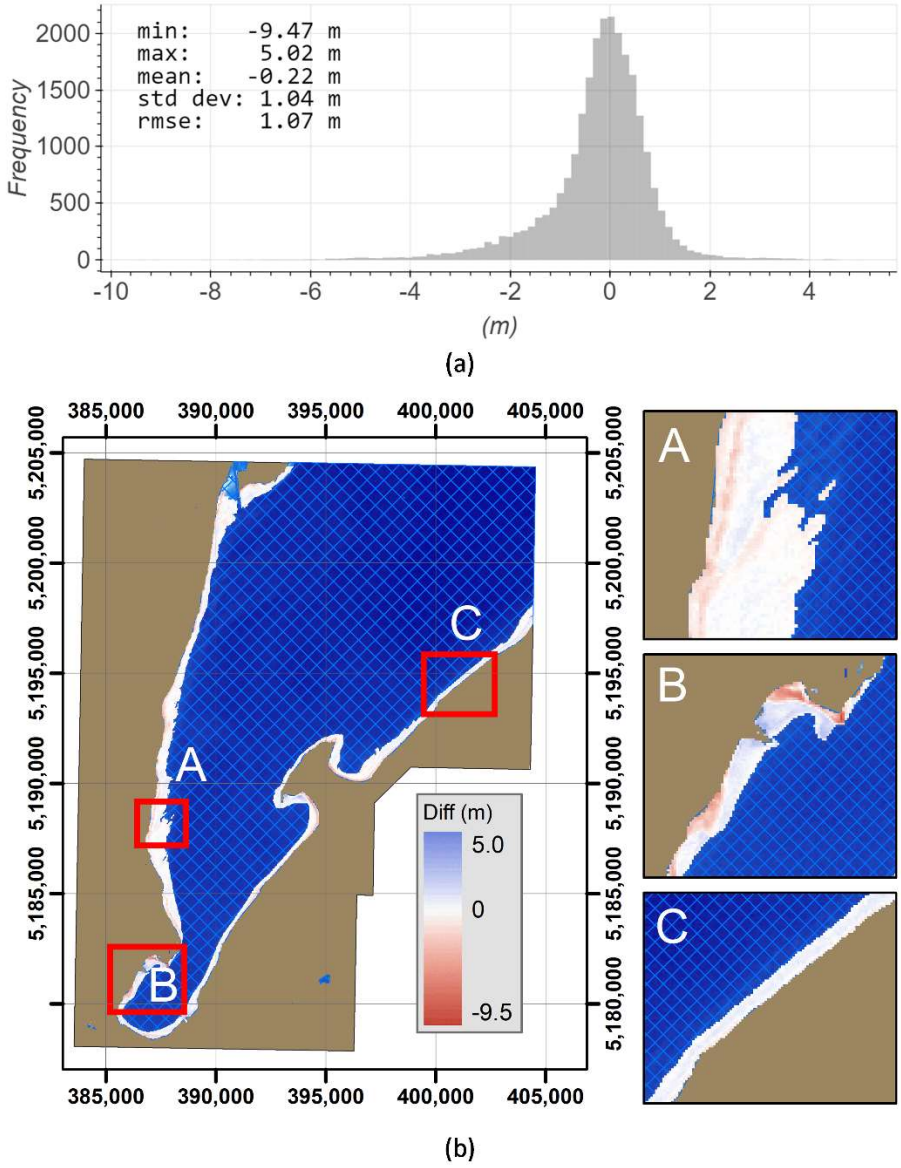

Figure 21. (a) The distribution of depth differences (SDB minus reference) has a mean of -0.22 m, a standard deviation of 1.04 m, and a root mean square error (RMSE) of 1.07 m. (b) The left panel shows an overview of the difference surface (SDB minus reference bathymetry). The subpanels A and B show detailed views of patterns likely due to sediment transport. Subpanel C shows an area of minimal difference. The blue hatched areas are outside the range of the reference depths. The datum is WGS84 (G1674), and the map projection is UTM Zone 16 N, with units of meters.

Global Spatiotemporal Usability Assessment

Nearshore and Coral Kd(490) Summary

The hexagonal bin map in Figure 22-a shows mean (over time) nearshore Kd(490) in areas where data are available. Distinct areas of high and low mean Kd(490) are clearly discernable. While Figure 22-a summarizes spatial variability in Kd(490) for the entire globe, 8-b summarizes the temporal variability for broadly-defined zones (marine, inland, and coral). A seasonal pattern is observed in the median Kd(490) for the marine and inland zones (indicated by the solid black lines in the boxplots in Figure 22-b), with the lowest values occurring in December for the marine zone and July for the inland zone. In all months, the median marine Kd(490) value is less than the median inland Kd(490) by an order of magnitude, with an average of 25% of all monthly marine values classified as J1. The coral zone has low, relatively stable median Kd(490) of 0.08 to 0.09 m^{-1} throughout the year, with 67% of all monthly values classified as J1.

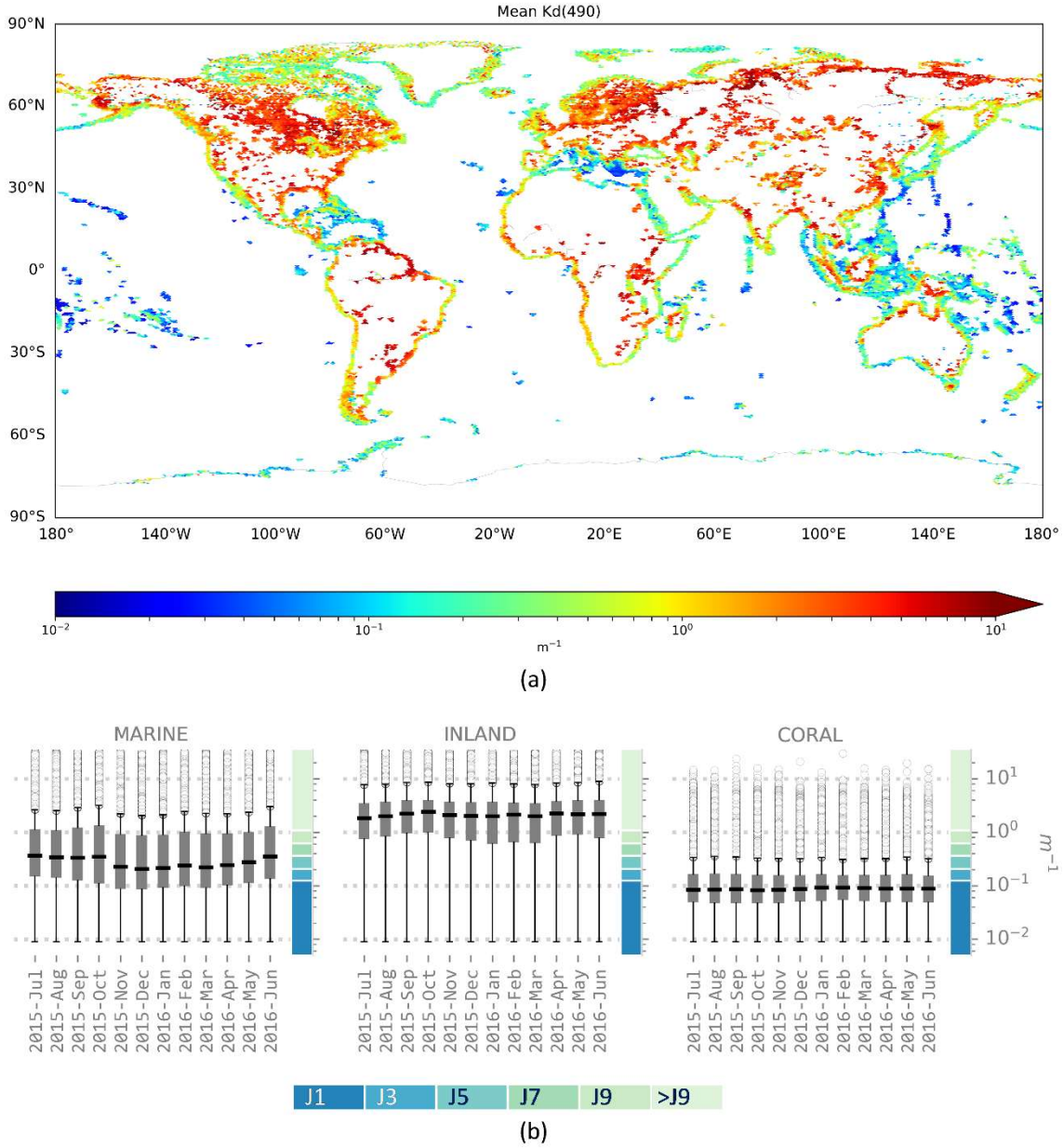

Figure 22. (a) The hexagonal bin map shows the mean global nearshore water clarity. (b) Box plots summarize the monthly distribution of global nearshore Kd(490) values within the marine, inland, and coral zones. The ranges of the Jerlov coastal water types are shown next to each panel for reference.

Figure 23 shows the cumulative Kd(490) data coverage for the 12 months of data used to compute the mean nearshore water clarity depicted in Figure 22-a. The areas depicted in dark red in Figure 23 indicate where a full twelve months' worth of Kd(490) data were available, whereas areas in purple indicate only a single month of available Kd(490) data. A latitudinal gradient associated with seasonality is clearly visible, particularly in North America, with data coverage in the most northern latitudes limited to the

northern hemisphere summer months. Other broad-scale variability in the marine zone includes a general lack of data in Antarctica and limited coverage in western equatorial Africa. Only 3 to 13% of the inland zone has monthly Kd(490) data, but many of the larger lakes and reservoirs are represented. Figures 8-a and 9 can be used in conjunction to evaluate where the spaceborne bathymetric mapping procedures developed in this work are likely to be successful. Areas depicted in dark red in Figure 23 and in deep blue in Figure 22-a generally indicate the greatest promise for spaceborne, fusion-based bathymetric mapping, as they represent high Kd(490) coverage, indicative of snow- and ice-free conditions over much of the year, and good average water clarity.

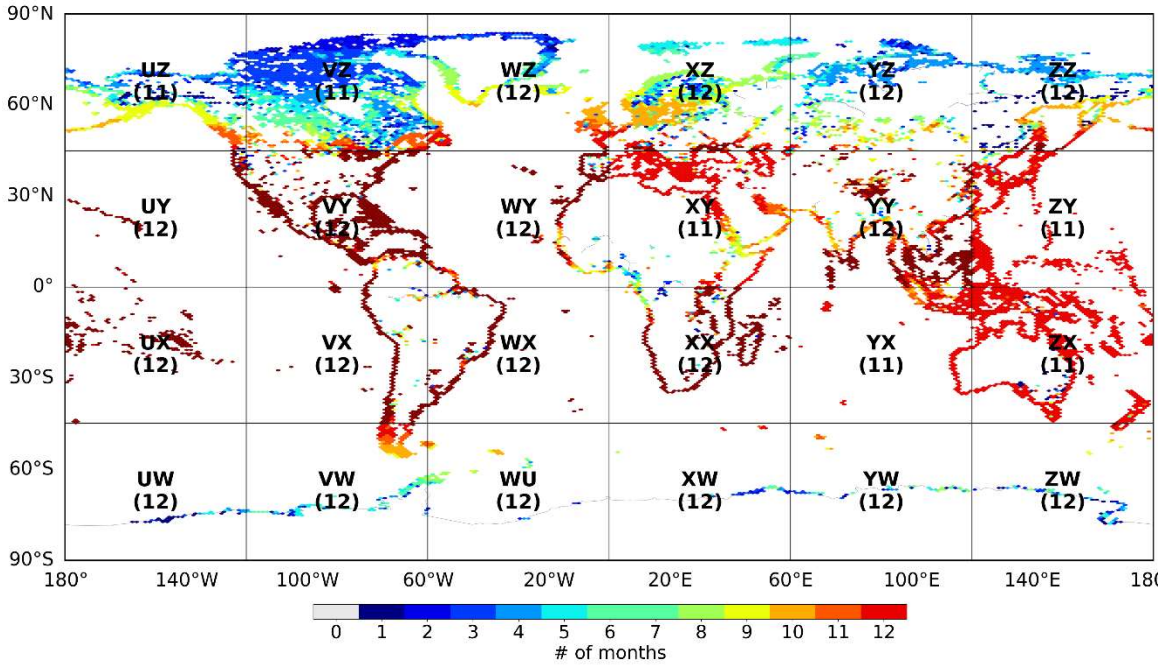

Figure 23. The colors represent the cumulative monthly Kd(490) coverage. The black gridlines show the extents of the original Kd(490) data tiles, along with the corresponding label and the number of data files within each tile.

Nearshore Water Clarity along Planned ICESat-2 Ground Tracks

Of the nearly 20 million kilometers of ICESat-2 ground track segments in the nearshore and coral zones, 17% of the segments fully or partially intersect the monthly Kd(490) data. Figure 24-a shows the proportion of ground tracks intersecting Kd(490) data for each month and zone, and Figure 24-b shows the corresponding proportions of classified segments. A clear seasonal pattern is observed in both the total length of nearshore and coral ground track segments. Although the marine zone has less than half of the total number of nearshore ground track segments, the marine zone accounts for 74% of all classified

segments. The clearest water class, J1, accounts for 25% of all classified segments. The relative minimums in June are artifacts resulting from certain VIIRS Kd(490) tiles containing data from only 11 months.

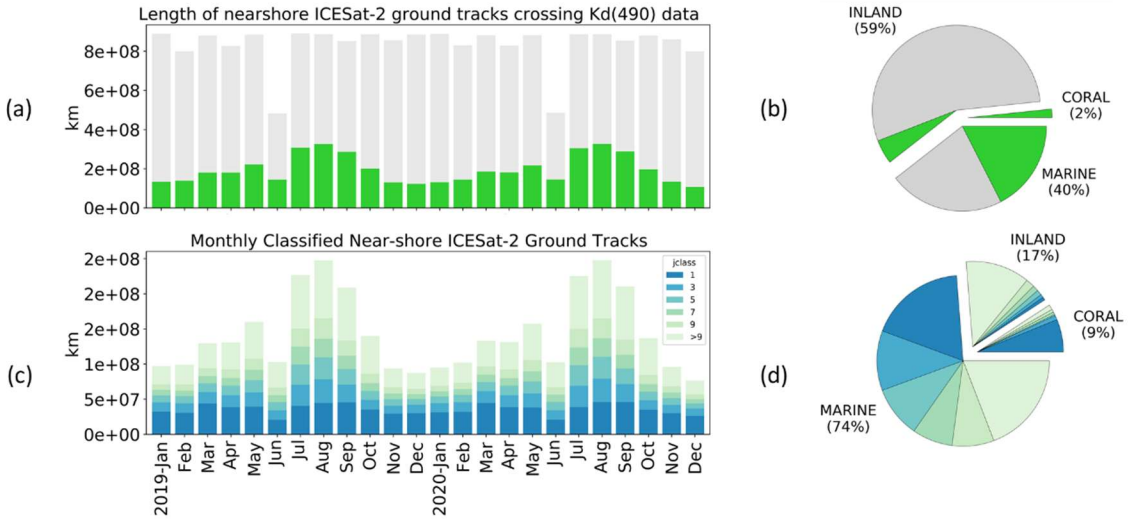

Figure 24. Panels (a) and (b) show the proportions of nearshore ground track segments that intersect, respectively, the corresponding monthly Kd(490) data and each nearshore zone type. Panels (c) and (d) show the proportions of nearshore ground track segments falling within each of the Jerlov water classes per month and per zone type, respectively.

The spatial distribution of the 3.4 million kilometers of classified ground track segments is shown in Figure 25-a. Broad-scale patterns of relatively clear and turbid nearshore areas are clearly discernable. Distinct regional and local variability is also observed, as shown in Figure 25-b. The full-resolution data depicted in Figure 25-a will be provided as an interactive map in a Jupyter notebook on ScholarsArchive@OSU, Oregon State University's open portal for data sharing.

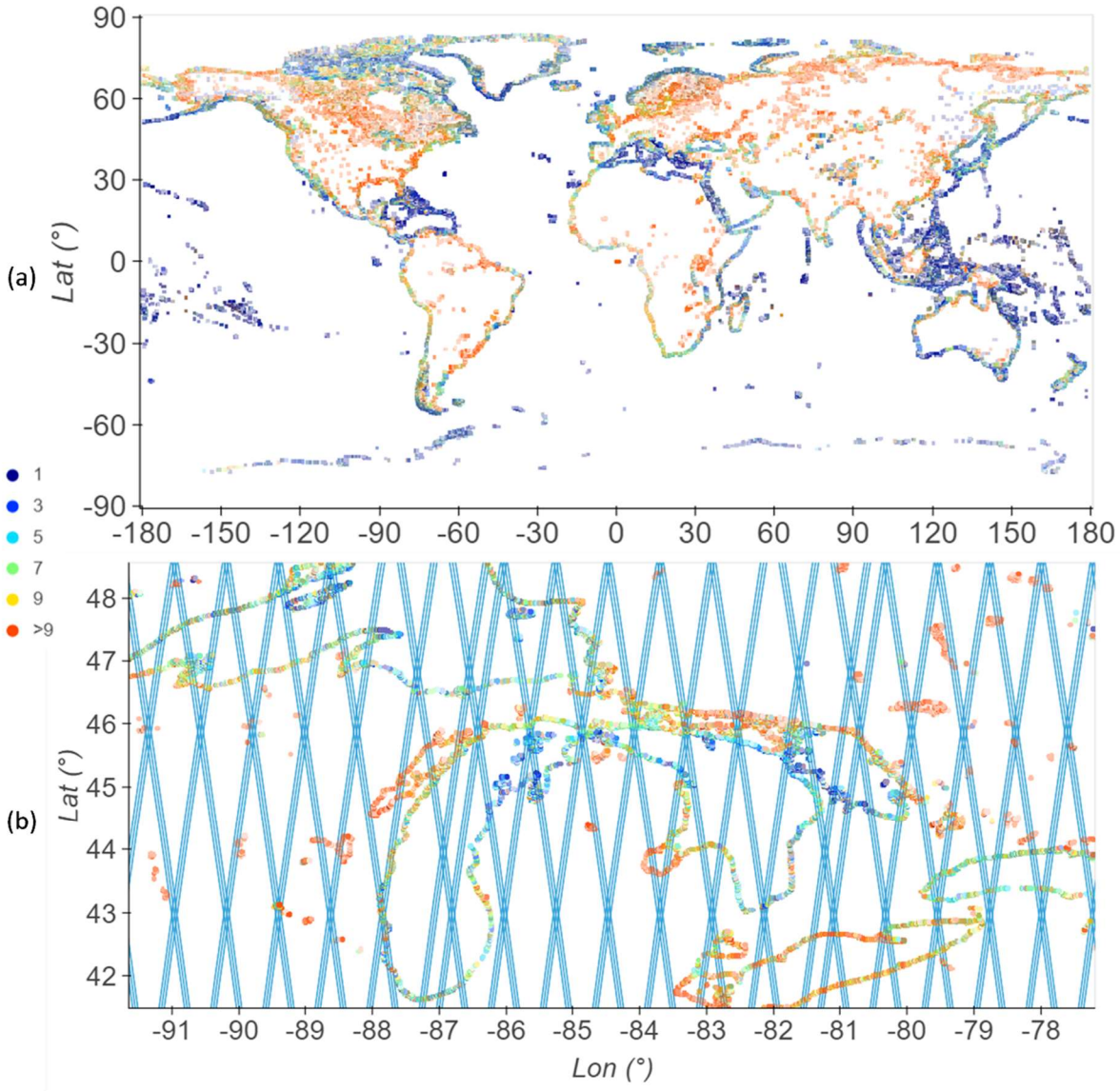

Figure 25. (a) The global spatial distribution of all classified monthly nearshore ground track segments is represented by the relative intensities of each class color. (b) A detail shows distinct water clarity variability along sections of North America's Great Lakes. The first month of ICESat-2 ground tracks is included for reference.

To highlight broad-scale areas with the clearest water, Figure 26 shows a highly generalized map of the total length of J1 ground track segments over the entire 2-yr period. J1 segments are distributed around much of Earth's nearshore/coral zones, with high concentrations in several regions, including the Caribbean, Western Greenland, the Mediterranean and Red Seas, and the broad area encompassing much of Southeast Asia, Northern Australia, and Polynesia. To facilitate assessing the viability of the current spaceborne data-fusion approach in relation to established water regions, Figure 26 also includes the extents of the MEOW and FEOW biogeographic regions.

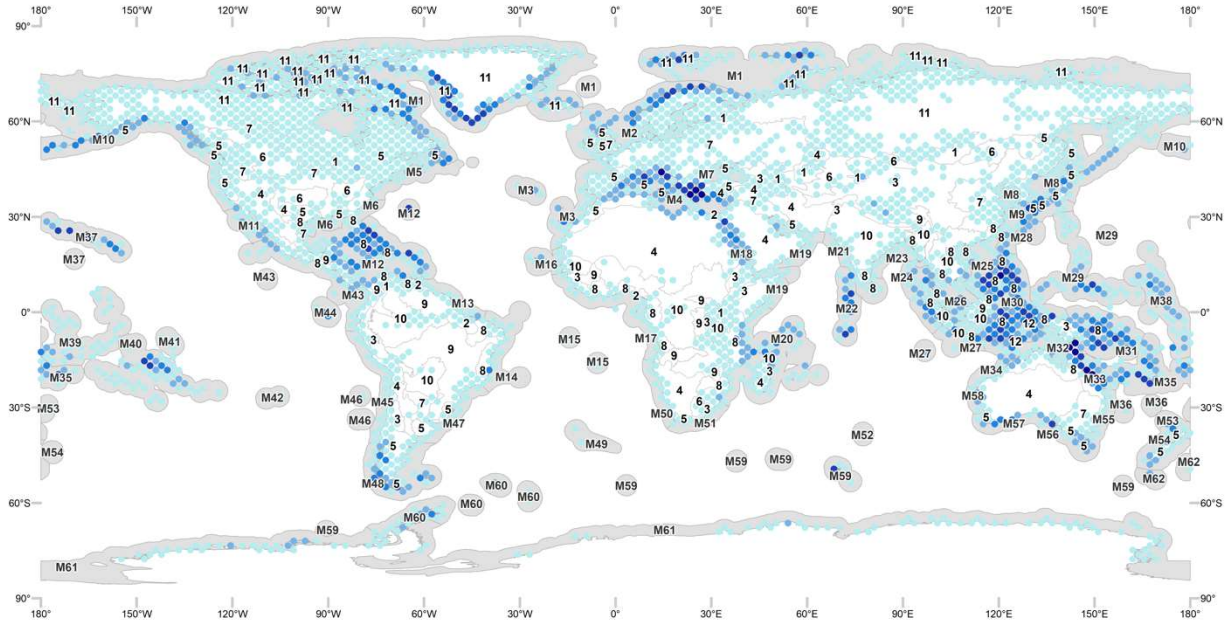

Figure 26. The centroids of a coarse-resolution hexagonal bin map are colored according to total length of J1 ground track segments to portray broad-scale distributions of areas most likely to benefit from a spaceborne data-fusion approach relying on ICESat-2. Included are the extents of the Marine Ecosystems of the World (MEOW) and Freshwater Ecosystems of the World (FEOW) biogeographic regions, depicted in grey and white, respectively.

Figure 27 summarizes the total length of J1 ground track segments for all 24 months for each MEOW/FEOW region. While some regions have consistently low or high monthly totals, other regions display seasonal trends. The prominent June data gaps visible in many of the MEOW regions is an artifact of VIIRS Kd(490) tiles ZY, YX, and ZX not containing data from that month, not a lack of J1 ground track segments. Figure 27 also lists the average regional densities of J1 ground track segments per square kilometer. Whereas the Artic has the largest total length of J1 segments, it ranks 37th according to average density. Conversely, although Easter Island has a total length of J1 segments three orders-of-magnitude smaller than the Arctic, it ranks 1st in average density of J1 segments. Although the freshwater regions generally have less total length and a lower density of J1 segments, there are areas with dense J1 coverage, such as North America's Great Lakes, the montane lakes of the Tibetan Plateau, and the large lakes of the African Rift Valley.

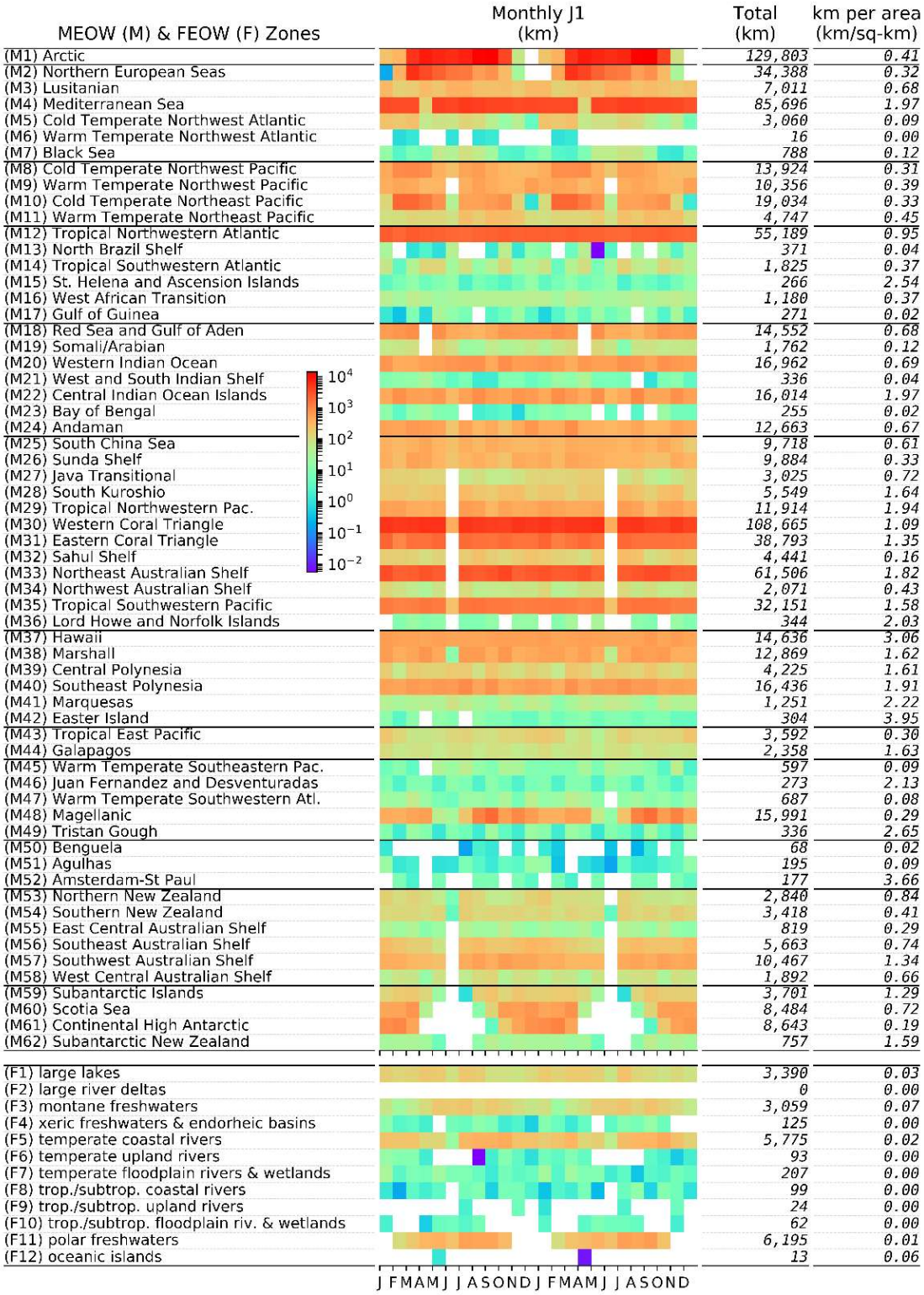

Figure 27. The monthly total length of J1 ground track segments is shown for each MEOW province and FEOW major habitat type. The MEOW provinces are grouped according to the parent category, or realm.

Discussion

The spaceborne approach presented in this research offers the potential for mapping nearshore bathymetry over much of the globe. Although the uncertainty of multispectral SDB generated in this study (nominally 1 m RMSE) is greater than that required by International Hydrographic Organization (IHO) specifications for navigation, SDB is valuable to many coastal, coral, and reservoir applications affected by the global nearshore data gap. While the spatial resolution of Landsat 8 OLI (30 m) is coarser than other available multispectral data, its global coverage, stable radiometry, and historical continuity provide a rich open database for SDB. The assumption that optical properties are consistent throughout a scene is also a limitation of the ratio method, but the relative simplicity of the approach is appealing when working on a global scale. Because a spaceborne approach could accommodate any method of deriving relative bathymetry, however, more-stringent methods of deriving relative bathymetry could be employed when desired. Another factor potentially limiting the applicability of the present method in certain applications is the availability of transformation parameters to convert either the MABEL/ATLAS depths or the calculated satellite bathymetry to a particular vertical datum. In areas not covered by well-defined transformations, the uncertainty associated with water-level corrections and vertical-datum definitions could be significant. Despite the disadvantages, the current method has the potential to contribute significantly to the best-available estimate of bathymetry in many poorly-surveyed, remote areas of globe and to monitoring already-mapped areas that undergo frequent change.

The spatiotemporal analysis indicates that the spaceborne data-fusion method would be viable over much of the globe throughout the year. Only 17% of the nearshore and coral zone ground track segments intersect the available VIIRS Kd(490) data, but the spatial and temporal distribution of the segments classified according to the corresponding Jerlov water type reveals distinct global, regional, and local areas of relatively clear water. Even in areas that are generally turbid throughout much of the year (such as the North Slope of Alaska and large portions of Russia's northern coast), there are windows (spatially and temporally) of J1 and J2 segments where the current spaceborne approach could produce meaningful results. It is important to interpret collectively the patterns of classified ground track segments and not the exact locations or lengths of individual segments, however, because fine-scale variation in the analysis of the distribution of classified segments is sensitive to a number of factors, including the resolution and availability of VIIRS Kd(490) data, the scale and accuracy of the vector datasets used to define the nearshore and coral zones, and the starting date and ground track for defining the monthly ground tracks. Other factors affecting the characterization of nearshore water clarity are the underlying definition of the nearshore zone and environmental factors such as predominant wave conditions, cloud cover, and marine vegetation. Despite the simplified nearshore definition and conditions assumed in this study, the results

provide a first-order depiction of where and when the proposed spaceborne bathymetric mapping approach will and will not be viable.

Beyond indicating the spatiotemporal viability of spaceborne bathymetric data fusion, the nearshore water-clarity analysis presented in this study can aid planning and operations for conventional nearshore mapping missions that depend on water clarity, including airborne lidar bathymetry (ALB) surveys. Just as with a spaceborne approach, a fundamental factor in predicting ALB data coverage (and maximum survey depth) is a priori information about the spatiotemporal variability of nearshore turbidity (Saylam et al., 2017). If no such data are available, knowing when and where to survey can be challenging and costly, particularly in remote areas and areas with highly variable water clarity. As an alternative to relying on a single source of Kd, such as VIIRS, to predict the viability of ALB and spaceborne lidar bathymetry (SLB), our method could be extended to include other spaceborne Kd sources, such as SeaWIFS (Mueller, 2000), MODIS (Knight and Voth, 2012; Shi et al., 2018), MERIS (Alikas et al., 2015), LANDSAT 8 (Lee et al., 2016), Sentinnel-3A, and GOCI (Huang and Yao, 2017). Local nearshore water-clarity is generally far more spatially and temporally variable than is detectable by any of these sensors, but they all could contribute, to varying degrees, to understanding broad-scale variability useful for survey planning and reconnaissance. Although beyond the scope of our current method, global databases of in situ water-clarity measurements, including Secchi depths and turbidity-sensor data, could complement satellite-derived data (Lee et al., 2018). Once operational, ALB and SLB sensors themselves could become sources of Kd data, as Kd can be approximated from the observed attenuation of the lidar signal throughout the water column (Montes et al., 2011).

Conclusion

This study investigated the feasibility of a purely spaceborne bathymetric mapping approach, based on synergistic fusion of active and passive satellite data, as well as a global spatiotemporal analysis to identify where and when such an approach could be utilized. The significance of this approach is that it provides a new method of filling the global nearshore data void that does not rely on existing reference depths. Furthermore, the fact that the approach relies entirely on satellite-based data is important, as it enables areas to be captured at specified revisit cycles, eliminates the need for personnel on site, and enables bathymetric mapping in even the most remote or difficult-to-access regions of the globe. Areas identified in this work as particularly promising for spaceborne bathymetric mapping and that intersect planned ICESat-2 tracklines during opportune time windows will be used to: 1) conduct higher spatial and temporal resolution water clarity analysis and 2) submit requests to NASA for early access to ICESat-2 ATLAS georeferenced photon return data products, such that the spaceborne, data-fusion approach to bathymetric mapping can be tested operationally in diverse regions. Future research plans also include developing

algorithms to fuse multiple sources of multispectral time-series imagery, including Landsat and Sentinel-2 data, and reference bathymetry, ranging from high-resolution IHO special-order hydrographic surveys to high-uncertainty crowdsourced soundings.

STATE-SPACE MODELING FOR EMPIRICAL MULTISPECTRAL SATELLITE DERIVED BATHYMETRY

Nicholas A. Forfinski-Sarkozi

Remote Sensing of Environment

(submitted 8/13/19, under review as of 11/2/19)

STATE-SPACE MODELING FOR EMPIRICAL MULTISPECTRAL SATELLITE DERIVED BATHYMETRY

Abstract

This research introduces a state-space framework for multitemporal empirical satellite derived bathymetry (SDB) that addresses limitations inherent in conventional methods, which rely on single images and are therefore prone to significant errors or missing data resulting from environmental noise, such as clouds and sediment plumes. State-space modeling offers a method to statistically model time series of relative SDB (rSDB) as calculated by a particular rSDB measure (e.g., band ratio) using data from one or more sensors. Having the ability to leverage bathymetric information contained in multispectral images over space and time has the potential to significantly expand the scope of SDB by providing gap-free models of rSDB, with corresponding per-pixel uncertainties, for an arbitrary date. The state space framework is demonstrated using the Stumpf band-ratio algorithm with Landsat 8 OLI and Sentinel-2 MSI time series covering the north and northwest shores of Nantucket, MA, USA. First, rSDB models were created for each time series individually and, to show its potential as a data-fusion mechanism, a fused time series. The best rSDB model was then used to generate SDB, the residuals of which served as a proxy indicator of the viability of the state space approach. The SDB was generated for a date representing the acquisition period of a reference bathymetric data set acquired with a Leica AHAB Chiroptera II topobathymetric lidar system. To evaluate the state space modeling of rSDB and not the SDB transformations associated with a given limited number of reference data points (as in the typical application of multispectral SDB), the rSDB model was linearly transformed to SDB using parameters derived from a regression incorporating all rSDB values and the corresponding reference depths. Spatially adaptive coefficients derived using geographic weighted regression were used to account for apparent invalid homogeneity assumptions regarding water quality and/or bottom type. The state space framework generated consistent sensor-specific and data-fused daily rSDB models that accounted for missing and noisy multispectral data. The example SDB generated from the Landsat 8 rSDB model for 10/20/2016 agreed with the reference bathymetry to within an RMSE of 0.29 m, which reveals the state space framework as a viable previously unexplored approach to multitemporal empirical SDB.

Introduction

Multispectral satellite derived bathymetry (SDB) has proliferated since its inception in the late 1960s. Numerous approaches have been developed, including empirical methods relying on the Beer Lambert law (Jupp, 1988; Lyzenga et al., 2006; Stumpf et al., 2003), analytical/semi-analytical methods relying on spectral mixing or lookup tables (Philpot, 1989), and more recently, a growing number of machine-learning methods using supervised classification and artificial neural networks (Ceyhun and

Yalçın, 2010; Salah, 2016). Most of these approaches, however, are limited in that they rely on a single multispectral image from a single sensor. Relying on a single image, whether using empirical, analytical, or machine learning techniques, can result in significant errors or missing data if ephemeral water-column, surface, and atmospheric conditions, such as sediment plumes or clouds, obscure or occlude the bathymetry signal. In addition to obstructive environmental conditions, single-image approaches suffer from the inability to incorporate statistical uncertainty analyses that are possible with multiple measurements. Beyond environmental and uncertainty limitations, single-image approaches are limited in that they do not consider spectrally inferred bathymetric information from time periods between available images. Particularly in empirical approaches relying on reference depths that are not spatiotemporally coincident with the available imagery, ignoring intervening bathymetry change can introduce significant errors. This study offers a method to mitigate the challenges of single-image SDB by providing a means to generate daily gap-free models of rSDB for an arbitrary date, with corresponding per-pixel uncertainties, using state space modeling of multispectral time series.

Although most approaches assume a single image, a few studies have heeded Tanis et al.'s (1983) suggestion, "to consider developing algorithms which can exploit co-registered multi-date imagery." Examples include using multiple Landsat images to assess potential morphological changes (Pe'eri et al., 2016; van Hengel and Spitzer, 1991), using series of SPOT images to extract water-level variations to coarsely estimate the attenuation coefficient and, in turn, depth (Kao et al., 2009; Melsheimer and Liew, 2001), and using Google Earth Engine resources to generate median composites (Traganos et al., 2018). While certain studies have begun addressing limitations of single-image SDB by incorporating analysis of images acquired over time, most have relied on only a handful of images and do not broadly leverage established frameworks capable of supporting multitemporal SDB, such as state space modeling of time series.

State space analysis of time series, specifically linear Gaussian state space analysis, offers an opportunity to expand the scope of multitemporal SDB, which in turn has the potential to help obtain bathymetry in the nearshore zone, which is notoriously difficult to map (Forfinski-Sarkozi and Parrish, 2019; Leon et al., 2013). (It is noteworthy that even in the current study's area of interest (AOI), a popular recreational area in the vicinity of Nantucket Island, MA, the largest scale nautical chart contains an area labeled "Unsurveyed.") State space models (SSMs), which are characteristically solved using Kalman filtering, span a variety of modeling approaches, but the unifying premise is that observed stochastic time series depend linearly on an unobserved state vector (Durbin and Koopman, 2012). In state space analyses, the model is comprised of a state equation, which relates one state to the next, and an observation equation, which relates the observations to the states. The nature of the state equation depends on the system being

modeled. For example, state equations governed by the laws of motion are ubiquitous in engineering fields concerned with navigation and target tracking (Allerton and Jia, 2005; Kam et al., 1997; T. Nicosevici et al., 2004), while animal movement studies often use variations of the random-walk ARIMA (autoregressive integrated moving average) equations (Nicosia et al., 2017). SSMs are established in many other disciplines, including oceanography (Tandeo et al., 2011; Wikle et al., 2013), epidemiology (LaDeau et al., 2011), econometrics (Harvey and Todd, 1983; Proietti, 2006), and acoustic bathymetric mapping (Saucan et al., 2014), but they have received little attention in the SDB community. Wüst (2004) used state space predictions of sand waves as observed in multibeam echosounder time series to support channel maintenance decisions in the North Sea, and Singh et al. (2015) used state space modeling of Landsat TM/ETM+/OLI data to estimate volume in poorly-gauged reservoirs, but SSMs have not been applied directly to spectral SDB time series.

In addition to state space modeling leveraging the information contained in a single time series to estimate an underlying state and provide a corresponding uncertainty, it also provides a data-fusion mechanism to combine time series from multiple sources. Data fusion is a broad term describing many approaches to combining many types of temporal and spatial data sets in many disciplines (Castanedo, 2013; Khaleghi et al., 2013; Varma et al., 2003), but the unifying principle is that different datasets are combined in some manner to achieve a result that is more desirable than any of the individual datasets. In remote sensing, the term has traditionally been associated with fusing 2-D images for pan-sharpening or classification (Schmitt and Zhu, 2016), but it has evolved to encompass a widening range of techniques and data types, including decision-level fusion of lidar and hyperspectral data (Wozencraft and Park, 2013), machine-learning based techniques to fuse MODIS and VIIRS ocean color data (Bai et al., 2016), and state space modeling of NDVI (De Bernardis et al., 2016; Militino et al., 2017; Stepčenko and Čižovs, 2016), among others. State space approaches fuse data series by including observation equations and uncertainty characteristics for each series, assuming the separate series are representations of the same state. The use of state space models for data fusion is common in the coastal bathymetry community, with diverse Kalman-based approaches combining heterogeneous video data to derive depth estimates (Birrien et al., 2013), ultra-short baseline (USBL) and multibeam sonar data for autonomous underwater vehicle (AUV) navigation (Barkby et al., 2009), and optical and radar data to model the surf-zone (Wilson et al., 2014), but using state space analysis to fuse multispectral time series is absent in empirical SDB research.

This research introduces a multitemporal SDB framework that incorporates state space modeling of multispectral times series to generate gap-free daily models of rSDB, which are then transformed to SDB. The framework is demonstrated using the Stumpf et al. (2003) band-ratio algorithm, but the framework is not fundamentally tied to a particular empirical SDB algorithm, because relative bathymetry

is modeled as a parameter separate from the derived bathymetry. Modeling rSDB, not SDB, offers the advantage of being able to generate rSDB for a particular date, which avoids SDB errors associated with using multispectral imagery and reference, or tuning, depths that are not temporally coincident. Modeling rSDB rather than SDB also provides a means to partially decouple the relative bathymetry parameter and imperfect measures of relative bathymetry, which characteristically have simplifying assumptions regarding the spatial homogeneity of water and bottom characteristics.

This study applies the state space approach to multitemporal SDB by first modeling Landsat 8 and Sentinel-2 imagery time series spanning a 29-month period, both separately and fused, and then generating a statistically optimal estimate of relative bathymetry using the best model for 10/20/2016, a date representing the acquisition period for a reference topobathymetric lidar dataset. The parameters to linearly transform the modeled relative bathymetry to absolute bathymetry are then generated using global and local regression. Unlike with a typical application of SDB, in which only a relatively few reference depths may be available, the regressions were performed using the entire high-resolution reference dataset, resampled to match the resolution of the state space rSDB model. The entire dataset was used because the purpose of this study was to examine the performance of the state space modeling, rather than the linear transformation associated with a particular set of reference depths. Finally, implications of multitemporal state space data fusion for global SDB spatiotemporal databases are discussed, following an analysis of the spatiotemporal variation of the SDB results.

Methodology

Summarized in Figure 28, the methodology consists of three main components. First, the preprocessing steps generate 30-m resolution, co-registered relative satellite derived bathymetry (rSDB) and reference topobathymetric lidar data. Second, per-pixel daily state space models are generated from the co-registered Landsat 8 and Sentinel-2 rSDB time series. Third, the best state space modeled rSDB for a date representing the acquisition period of the reference bathymetry lidar data is linearly transformed to absolute bathymetry using locally adaptive parameters generated using geographically weighed regression.

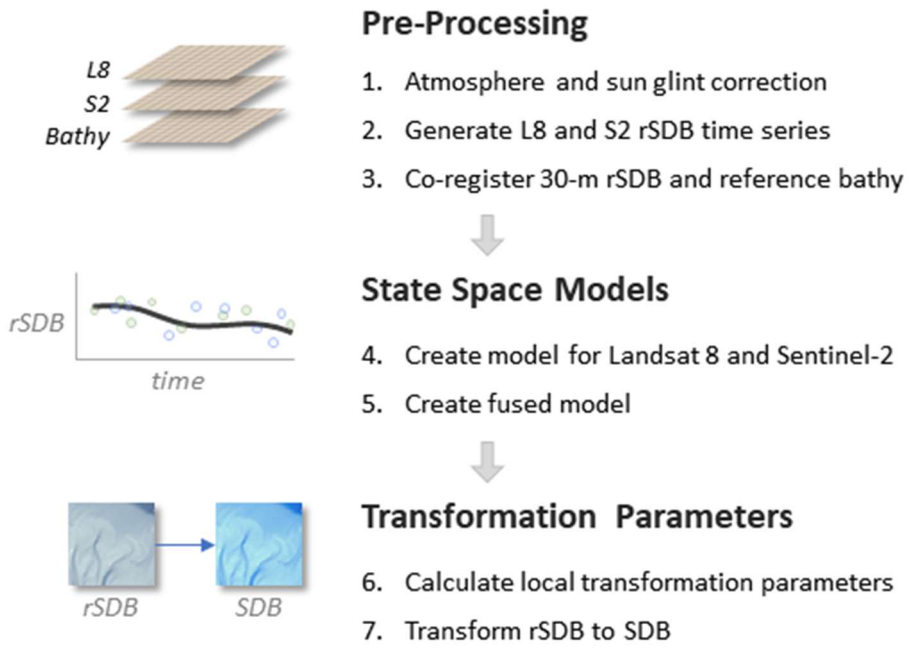

Figure 28: Methodology Overview - The purpose of preprocessing is to generate co-registered rSDB time series and reference bathymetry. The 5-m resolution bathymetry data and the 10-m resolution Sentinel-2 data were resampled to match the resolution and grid-cell alignment of the 30-m resolution Landsat 8 data. State space models of the co-registered 30-m L8 and S2 rSDB are then generated using local linear modeling of single and data-fused timeseries. Finally, the state space rSDB data are linearly transformed to real-world bathymetry using transformation parameters derived from geographically weighted regression (GWR).

Study Site

The study site is the vicinity along the northern shore and western end of Nantucket, MA, USA, including Nantucket and Madaket Harbors (Figure 29-a). The geomorphology of the area is characterized by glacial landforms stemming from the advance and retreat of the Launrentide ice sheet during the Wisconsinian glaciation period (Giese et al., 2015; Oldale, 2001). With surficial sediments consisting generally of unconsolidated, sorted outwash sands, fine clays, and gravels associated with glacial moraines, the island's shoreline is greatly influenced by sediment transport, with the northern shore typically dominated by deposition. Situated off the coast of Cape Cod, with exposure to the open ocean, the area often experiences significant weather events, including hurricanes, tropical storms, and nor-easters, which have significant impacts on sediment transport and, in turn, bathymetry. Although areas with dynamic bathymetry are subject to significant challenges in conventional SDB methods, if the available reference depths and the multispectral image are not temporally coincident, a state space framework for SDB inherently mitigates these challenges by applying Kalman filtering to rSDB timeseries. Numerous sandbars

and alongshore troughs can be observed in the Landsat 8 RGB composite of the AOI shown in Figure 29-b. The AOI, particularly Nantucket and Madaket Harbors, also includes eelgrass beds (*Zostera marina*).

Data Sets

This study used multispectral time series from the Operational Land Imager (OLI) and MultiSpectral Instrument (MSI) sensors onboard the Landsat 8 and Sentinel-2 satellites, respectively. The Landsat 8 time series included 63 Tier 1 images spanning the 1473-day period from 01/25/15 to 02/05/19. The Sentinel-2 time series included 119 images spanning the 1276-day period from 08/09/15 to 02/04/19. This study also used a high-resolution topobathymetric lidar data set acquired with a Leica/AHAB Chiroptera II lidar system during the period from 10/5/16 to 10/31/16.

Landsat 8 OLI

The multispectral Operational Land Imager (OLI) sensor onboard the Landsat 8 satellite is a 9-band, 30-m spatial resolution visible and near-infrared (VNIR) radiometer with a push-broom configuration and 12-bit radiometric resolution (USGS, 2016). Landsat 8 has a sun-synchronous, near-polar orbit with a repeat cycle of 16 days and an equatorial crossing time of approximately 10:00 AM local time. This study used the blue (438 nm) and green (561 nm) bands from 63 Tier 1 scenes covering Worldwide Reference System 2 row/path ID 011/031, spanning the period from 01/25/15 to 02/05/19. The Level 1 Landsat 8 OLI data were downloaded from the Google Cloud Platform using the Google Cloud Storage API.

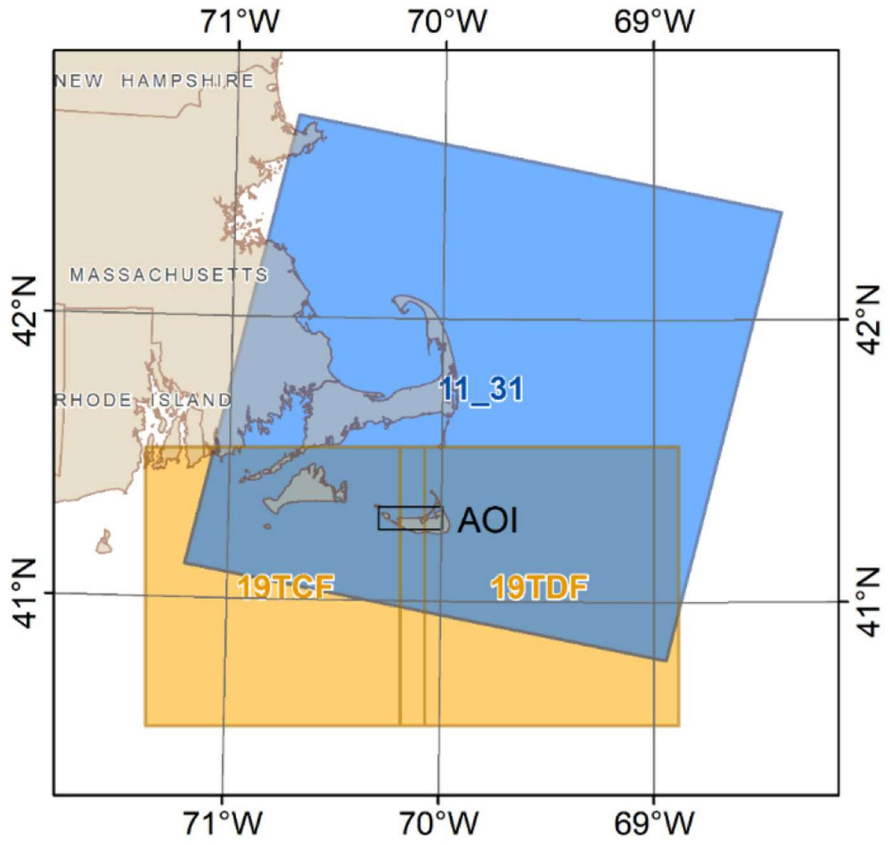

(a)

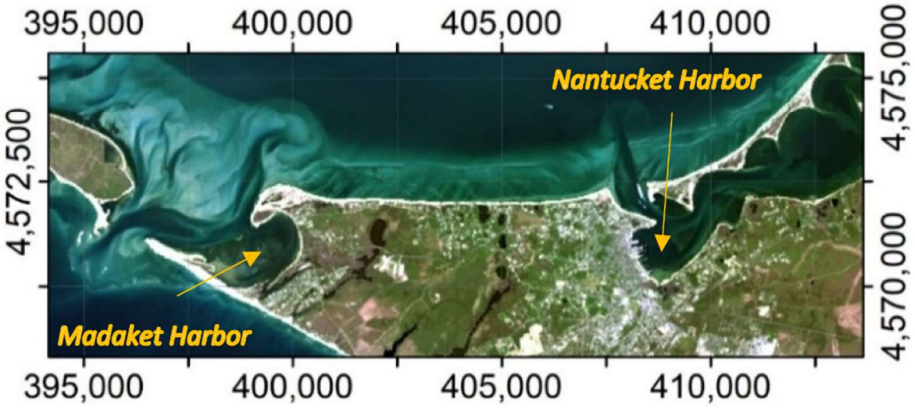

(b)

Figure 29: Study Site – (a) The study site is the vicinity along the northern and western shores of Nantucket, MA, USA. The Area of Interest (AOI) is covered by Worldwide Reference System 2 row/path ID 011/031 and Sentinel-2 tiles 19TCF and 19TDF. (b) Dominated by deposition of glacial sediments stemming from the Wisconsinian Glaciation Period, the study site is characterized by shifting shoals, alongshore troughs, and sand bars, which are clearly visible in the Landsat 8 RDB composite. The study area also contains eel grass beds, particularly in Madaket and Nantucket Harbors.

Sentinel-2 MSI

The MultiSpectral Instrument (MSI) sensor onboard the two satellites comprising the Sentinel-2 mission (Sentinel-2A and Sentinel-2B) is a push-broom sensor with a wide swath width of 290 km (ESA, 2015). MSI acquires data in 13 bands ranging from the visible and near-infrared (VNIR) wavelengths to the shortwave infrared (SWIR) wavelengths. The blue ($blue_{S2A}$ = 492 nm, $blue_{S2B}$ = 492 nm) and green ($green_{S2A}$ = 560 nm, $green_{S2B}$ = 559 nm) bands used in this study have 10-m spatial resolution, with 12-bit radiometric resolution. Sharing the same sun-synchronous orbit, but offset by 180°, Sentinel-2A and Sentinel-2B have an equatorial crossing of 10:30 AM local time and a collective repeat cycle of 5 days (10 days individually). The Level 1 Sentinel-2 data for 119 granules covering Sentinel-2 tiles 19TCF and 19TDF, from the period spanning 08/09/15 to 02/04/19, were acquired from the Google Cloud Platform using the Google Cloud Storage API.

Leica Chiroptera II

The reference topobathymetric lidar dataset was acquired with a Leica/AHAB Chiroptera II lidar system over the period from 10/5/16 to 10/31/16 (NOAA NGS, 2017). The 515-nm wavelength Chiroptera II topobathymetric lidar was flown at 120 knots at an AGL altitude of 400 m, with a scanner pulse rate of 35 kHz and a scan frequency of 2358 Hz. The nominal pulse density (NPD) was 1.34 ppsm. Horizontal control was achieved with kinematic GPS relying on two base stations adjusted to NAD83(2011) Epoch 2010.00, UTM zone 19 N. Vertical control, relative to the NAD83(2011) GRS ellipsoid was verified with a series of ground check points. Horizontal and vertical RMSE accuracies (scaled to 95% confidence) were reported to be 32.3 and 29.0 cm, respectively. The data were downloaded as a collection of 5-m resolution 500 x 500 m digital elevation models (DEMs) from NOAA's Digital Coast (NOAA, 2016b).

Pre-Processing

The purposes of preprocessing were to (1) apply atmosphere and sun-glint corrections to the Landsat 8 and Sentinel-2 data and (2) generate co-registered rSDB time series and reference bathymetry. The 5-m resolution bathymetry data and the 10-m resolution Sentinel-2 data were resampled to match the resolution and grid-cell alignment of the 30-m resolution Landsat 8 data.

Multispectral Imagery

The first step in preprocessing the Landsat 8 and Sentinel-2 data was using Acolite (version 20190326.0) to apply atmospheric and sun-glint corrections. Unlike with single-image SDB, radiometric corrections are crucial when comparing reflectances from different images taken at different times. Unlike land-based or open-ocean atmospheric correction (AC) tools, which can result in large errors when applied

to coastal environments, Acolite is designed to work in relatively turbid coastal waters (Vanhellemont, 2019), where suspended particles invalidate assumptions regarding little or no signal in the NIR. Acolite was also configured to clip the Landsat 8 and Sentinel-2 data to the AOI, to merge the Sentinel-2 19TCF and 19TDF SAFE product tiles, and to output the blue and green bands of the water-surface reflectance (L2W) data product, which were the two spectral bands used to generate rSDB. The second step in preprocessing the multispectral data was generating rSDB from the blue and green L2W bands for each image in the Landsat 8 and Sentinel-2 time series. Although the state space approach to SDB does not depend on a single, particular SDB algorithm, it is demonstrated using the well-known Stumpf et al. (2003) band-ratio method.

Reference Bathymetry

Preprocessing the topobathymetric lidar dataset consisted of using the Python module xarray to merge the 500x500-m ERDAS image tiles into a single file and using the Python module Iris to resample, using bilinear sampling, the merged file to match the 30-m resolution of the Landsat 8 data.

State Space Models

The general premise of a state space model is that the signal of interest, i.e., the state, is not directly observable, but indirectly observable as a linearly transformed version of it, with noise. Using the notation of Shumway and Stoffer (2017), the general form of a state space model is defined by a state equation (Equation 12) and an observation equation (Equation 13), which relates the observations to the state. The variables in Equations 12 and 13 are explained in Table 9.

$$x_t = \Phi x_{t-1} + \Upsilon u_t + w_t, \quad \text{(Eq. 12)}$$

$$y_t = A_t x_t + \Gamma u_t + v_t \quad \text{(Eq. 13)}$$

The model assumed in this study is a local level, or random walk with noise, which is equivalent to an autoregressive (AR) model with a slope of 1. With no exogenous, or control, variables, the general state space equations in 1-D simplify to Equations 14 and 15,

$$x_{t+1} = x_t + w_t, \;\; w_t \sim N(0, Q) \quad \text{(Eq. 14)}$$

$$y_t = x_t + v_t, \qquad v_t \sim N(0, R) \quad \text{(Eq. 15)}$$

where w_t and v_t are 0-mean normal vectors with covariance Q and R, respectively. Wüst (2004) modeled bathymetry and Singh et al. (2015) modeled water volume with an additional trend component, but heuristic exploration of the relative satellite derived bathymetry data in this study did not suggest a trend term was generally necessary.

Table 9: State Space Model Variables – The table lists the variables in the general state space models as represented by Equations 12 and 13. The dimensions p, q, and r refer to the number of states, observations, and exogenous variables, respectively.

Variable	Description	Dimension
x_t	State vector, time t	$p \times 1$
x_{t-1}	State vector, time t-1	$p \times 1$
Φ	State transition matrix	$p \times p$
Υ	Control matrix	$p \times r$
w_t	State noise	$p \times 1$
y_t	Observed data vector	$q \times 1$
A_t	observation matrix	$q \times p$
Γ	Direct transmission matrix	$q \times r$
u_t	Input, or control vector	$r \times 1$
v_t	Observation noise	$p \times 1$

The state space model is solved using Kalman smoothing, which is the bi-directional (i.e., forward and backward) extension of Kalman filtering, which consists of a prediction (Equation 16) followed by a measurement update (Equation 17) relying on the Kalman gain (Equation 18).

$$x_t^{t-1} = \Phi x_{t-1}^{t-1} + \Upsilon u_t \quad \text{(Eq. 16)}$$

$$x_t^t = x_t^{t-1} + K_t(y_t - A_t x_t^{t-1} - \Gamma u_t) \quad \text{(Eq. 17)}$$

$$K_t = P_t^{t-1} A_t' [A_t P_t^{t-1} A_t' + R]^{-1}, \quad \text{(Eq. 18)}$$

where P_t^{t-1} and P_t^t, defined by Equation 19 and 20, respectively, are the error covariances associated with Equations 16 and 17, respectively.

$$P_t^{t-1} = \Phi P_{t-1}^{t-1} \Phi' + Q \quad \text{(Eq. 19)}$$

$$P_t^t = [I - K_t A_t] P_t^{t-1} \quad \text{(Eq. 20)}$$

Unlike with state space models based on known model parameters, such as those involving the laws of motion, state space solutions of AR models require that the model parameters be estimated as part of the solution, via maximum likelihood estimation (MLE).

Landsat 8 and Sentinel-2 rSDB State Space Models

This research explores two approaches to state space modeling of rSDB. In the first, Landsat 8 and Sentinel-2 time series of rSDB were modeled separately, while in the second, the two time series were combined, or data-fused, into a single model. The Python statistical package statsmodels (Seabold and Perktold, 2010) was used to implement the state space approaches, which are summarized in Figure 30.

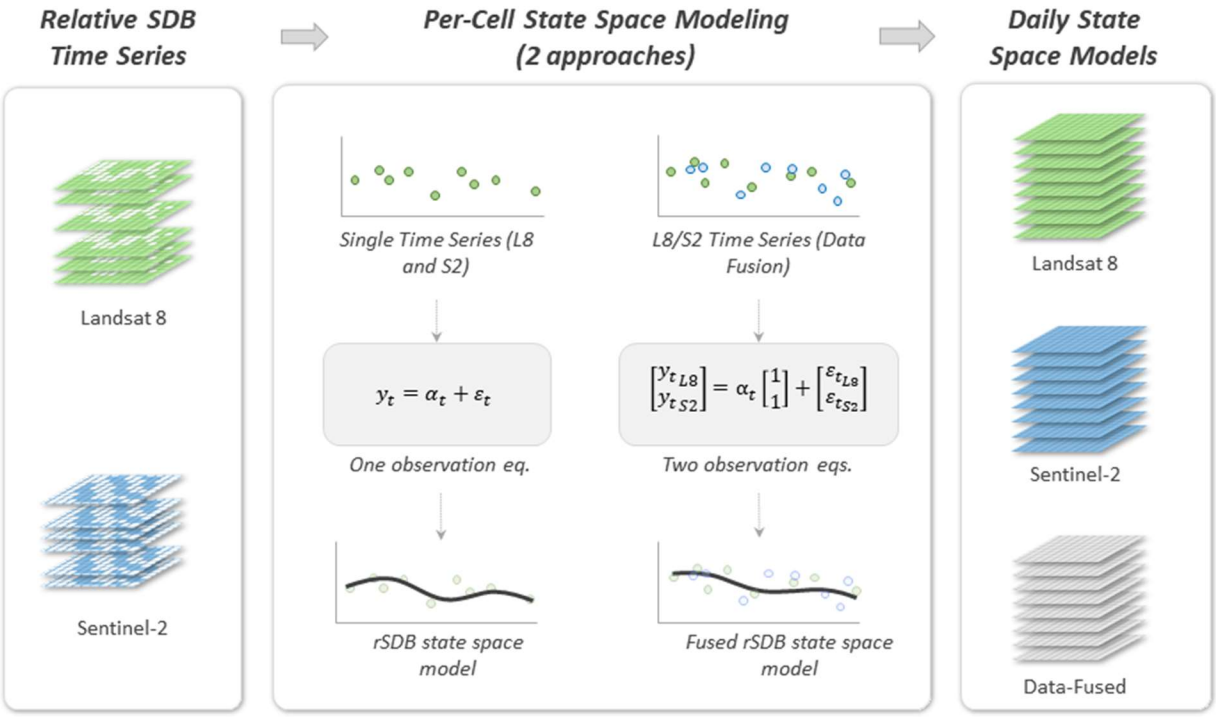

Figure 30: State Space Modeling – State space modeling was applied to Landsat 8 and Sentinel-2 rSDB time series using two approaches. First, each time series was modeled separately using a state space model consisting of a single observation equation. Second, both time series were data-fused into a single model using a state space model consisting of two observation equations, i.e., an observation for each time series. The output of each state space model was a daily time series of rSDB spanning from 1/1/15 to 2/28/19.

The Nelder-Mead (1965) optimization method was specified for the maximum likelihood estimation type. The input to both state space approaches was the respective time series of Landsat 8 and/or Sentinel-2 rSDB calculated during preprocessing. Whereas one observation equation was used in the single time series approach, two observation equations were used in the data-fusion approach. The output of both state space approaches was a daily time series of state space modeled rSDB, with corresponding uncertainties, for every cell in the AOI. The models were run using 2-core multiprocessing on an MSI Workstation laptop (model WE73) with 32 GB RAM, an Intel 8th Generation i7-8750H 6-core processor, and a solid-state drive.

Transformation Parameters

Unlike a typical application of satellite derived bathymetry, in which relatively few reference depths may be available, the transformation parameters needed to map the unitless rSDB values to real-world depths were generated using a 1-to-1 correspondence of all rSDB values and reference depths. The entire reference dataset, rather than a subsample representative of sparse reference depths, was used because

the intent of this study was to assess the state space modeling of rSDB, not the linear transformation associated with a particular set of reference depths. Transformation parameters were initially derived via ordinary least squares (OLS), whereby the reference depths were regressed against the corresponding rSDB values. However, because the initial OLS results contained unrealistically large residuals attributed to invalid assumptions regarding the homogeneity of the water and/or bottom characteristics, local transformation parameters were derived using geographically weighted regression (GWR), instead. GWR is already established in the SDB literature, with Vinayarah et al. (2016) and Su et al. (Su et al., 2014) demonstrating the value of geographically adaptive coefficients to account for spatial nonuniformity in transformation parameters. The bandwith, θ, was heuristically set to an adaptive value of 50 points. The Grass GIS module r.gwr was used to perform the GWR calculations. Once the transformation parameters were generated using GWR, SDB was generated by applying the transformation parameters to the rSDB state space model values. A point worth emphasizing is the that purpose of this application of SDB is not to infer bathymetry from multispectral imagery, although that is the net result. Rather, the purpose is to provide a mechanism to assess the correlation between the known absolute bathymetry and the modeled relative bathymetry as a measure of the ability of the state space approach to portray relative bathymetry via the rSDB parameter.

Results

Landsat 8 and Sentinel-2 Data Coverage

Figure 31 summarizes the temporal distribution of available Landsat 8 and Sentinel-2 images from the period 1/1/15 to 2/28/19, with the blue and red rectangles corresponding to individual Landsat 8 and Sentinel-2 scenes, respectively. The intensity of the color of each image tile corresponds to the relative proportion of water pixels (normalized by the maximum number of water pixels), as classified by Acolite, and the number in each cell shows the day of acquisition. In general, each 30-m pixel covering the AOI has nominally 30-40 Landsat 8 values and 35-45 Sentinel-2 values.

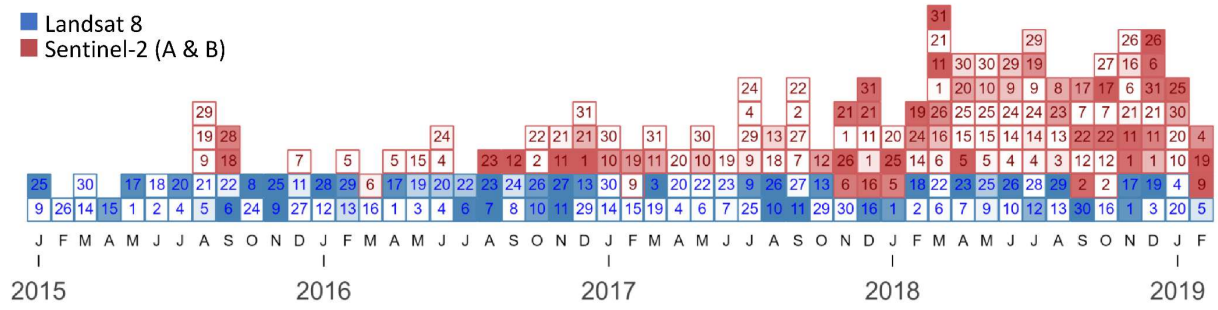

Figure 31: Landsat 8 and Sentinel-2 Data Summary – Each blue and red square corresponds to an available Landsat 8 and Sentinel-2 scene, respectively, over the period 1/1/2015 – 2/28/2019. The intensity of the colors corresponds to the relative proportion of water pixels (normalized by the maximum number of water pixels), and number in each cell shows the day of acquisition.

State Space Modeling

Figure 32-a shows example state space model results for a single pixel, including the smoothed state and the corresponding 95% confidence interval (CI) for the single and data-fused approaches. Three characteristics of this example are noteworthy. First, the Sentinel-2 model has a relatively large 95% CI in the region labeled A, which corresponds to a period of few Sentinel-2 scenes (as depicted in Figure 31). Second, all three smoothed states show general agreement in the region labeled B. Third, the Sentinel-2 smoothed model has relatively large values in the region labeled C, which coincides with a time period containing many more Sentinel-2 scenes than Landsat 8 scenes. Examination of the daily mean of all the state space rSDB models reveals these same three characteristics, as shown in Figures 32-b and 32-c, which show the mean state space rSDB and corresponding mean CI, respectively. The distinctive qualitative differences between the mean Landsat 8 and Sentinel-2 time series generally coincide with variations in the number of available scenes from each sensor. These differences are consistent with the expectation of drift in the absence of observations to constrain the models. The large CI observed at the beginning of the Landsat 8 and Sentinel-2 models correspond to smoothed states for which the Kalman filter had not yet converged.

Figure 33-a shows the Landsat 8, Sentinel-2, and data-fused state space rSDB models for 10/20/2016, the date representing the acquisition period of the reference topobathymetric lidar dataset, with Figure 33-b showing the corresponding histograms. Qualitatively, all three models are internally consistent representations of relative bathymetry containing recognizable bedforms and general bathymetric relief. However, the three models contain varying levels of noise, with the data-fused model noticeably noisier than the Landsat 8 and Sentinel-2 models. The data-fused model contains noise speckle (not discernable at the scale of the figure panel) over much of the AOI, along with patches of isolated artifacts (yellow circles).

Artifacts also exist in the Landsat 8 and Sentinel-2 models, although of a slightly different nature (white squares). In addition to noise speckle and isolated artifacts, the Sentinel-2 and data-fused models appear smoother in certain areas and do not resolve certain features that are observed in the Landsat 8 model (black squares). Quantitatively, the Sentinel-2 model, with a mean rSDB of 1.117, has a bias relative to the Landsat 8 and data-fused models, which have mean rSDB values of 1.082 and 1.088, respectively. In addition to a larger mean rSDB, the Sentinel-2 model has a larger mean standard error than the Landsat 8 and data-fused models. As observed in the images in Figure 34-a and histograms in Figure 34-b, the spatial and statistical distributions of the data-fused standard errors, respectively, are more similar to the Landsat 8 model than the Sentinel-2 model, which is consistent with the expected behavior of the Kalman filter giving greater weight to the less-uncertain observations. Overall, the spatial distributions of the standard errors reflect the spread of the rSDB values for each cell, given the collective influence of cloud cover over the entire time series.

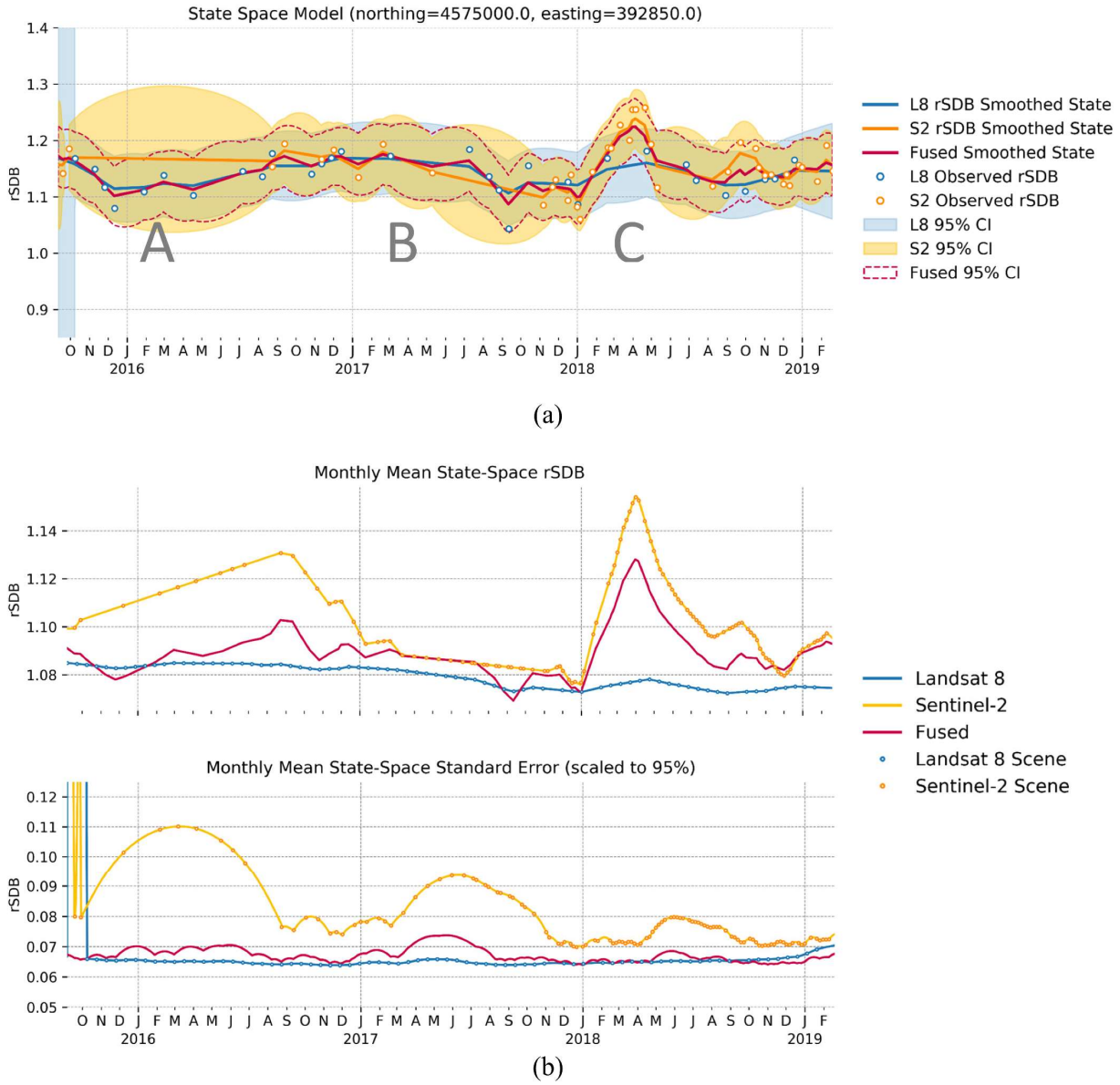

Figure 32: Example State Space Models – (a) The smoothed states and corresponding 95% confidence intervals (CIs) are shown for a single cell (northing=4,575,000, easting=392,850). The S2 model has a relatively large CI in region A and a relatively large smoothed state in region C. All three models show good agreement within region B. (b) The average smoothed states of all cells are shown with points representing available scenes. (c) The average standard errors (scaled to 95%) of all cells are shown with points representing Landsat 8 and Sentinel-2 observations. Note the different vertical scales for each subplot.

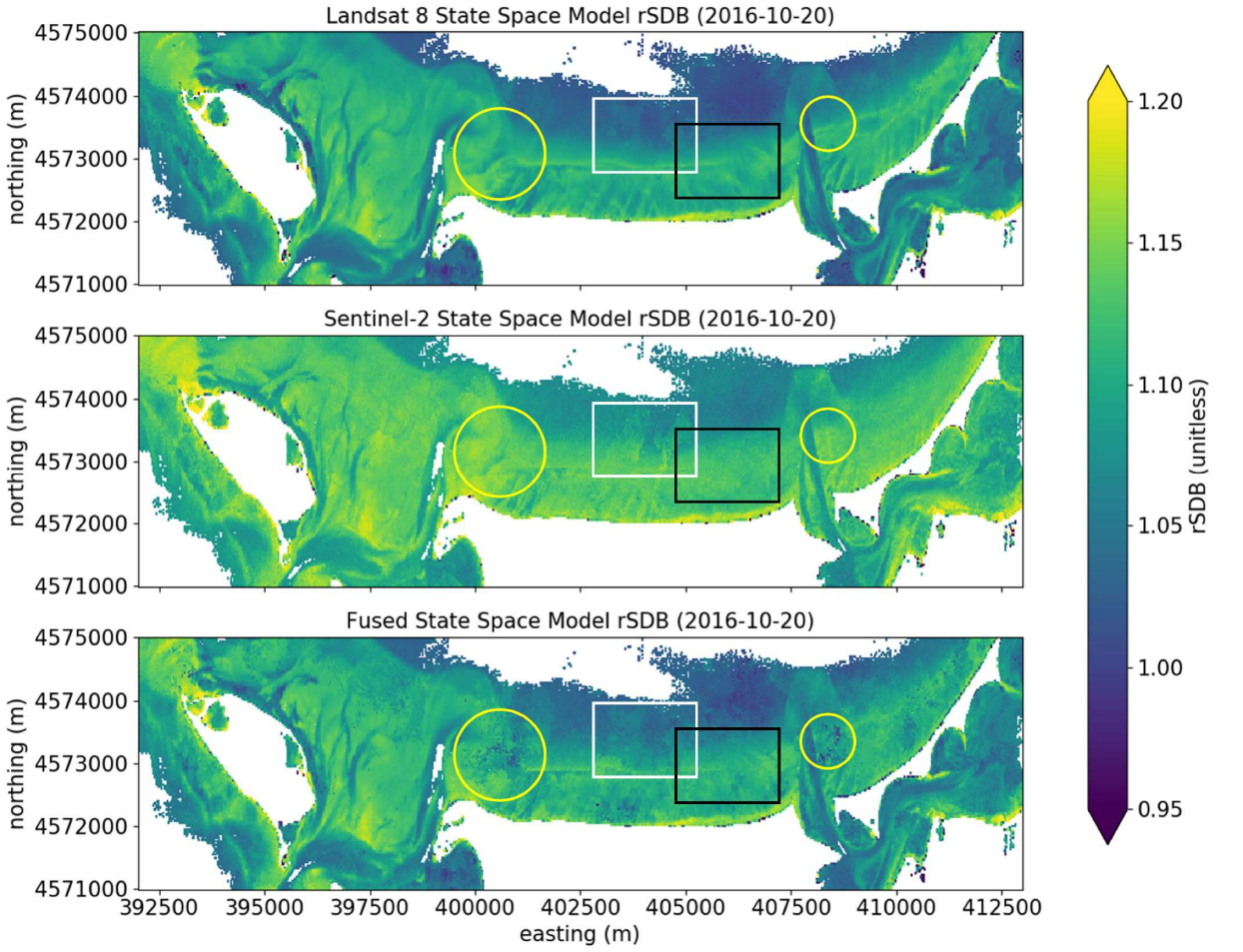

(a)

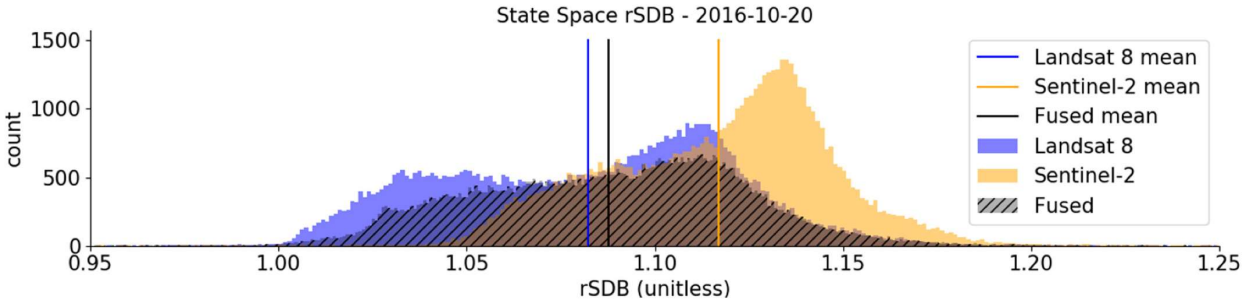

(b)

Figure 33: State Space Models from 10/20/16 – (a) The Landsat 8, Sentinel-2, and data-fused state space models from 10/20/2016 are displayed with the same colormap to aid comparison. Although the Landsat 8 model contains artifacts (see white rectangle), it is less noisy (see yellow circles) and resolves more features (see black rectangle) than the Sentinel-2 and data-fused models. (b) The distribution of the Sentinel-2 model (mean = 1.117) contains a noticeable offset relative to the Landsat 8 (mean = 1.082) and data-fused (mean = 1.088) models.

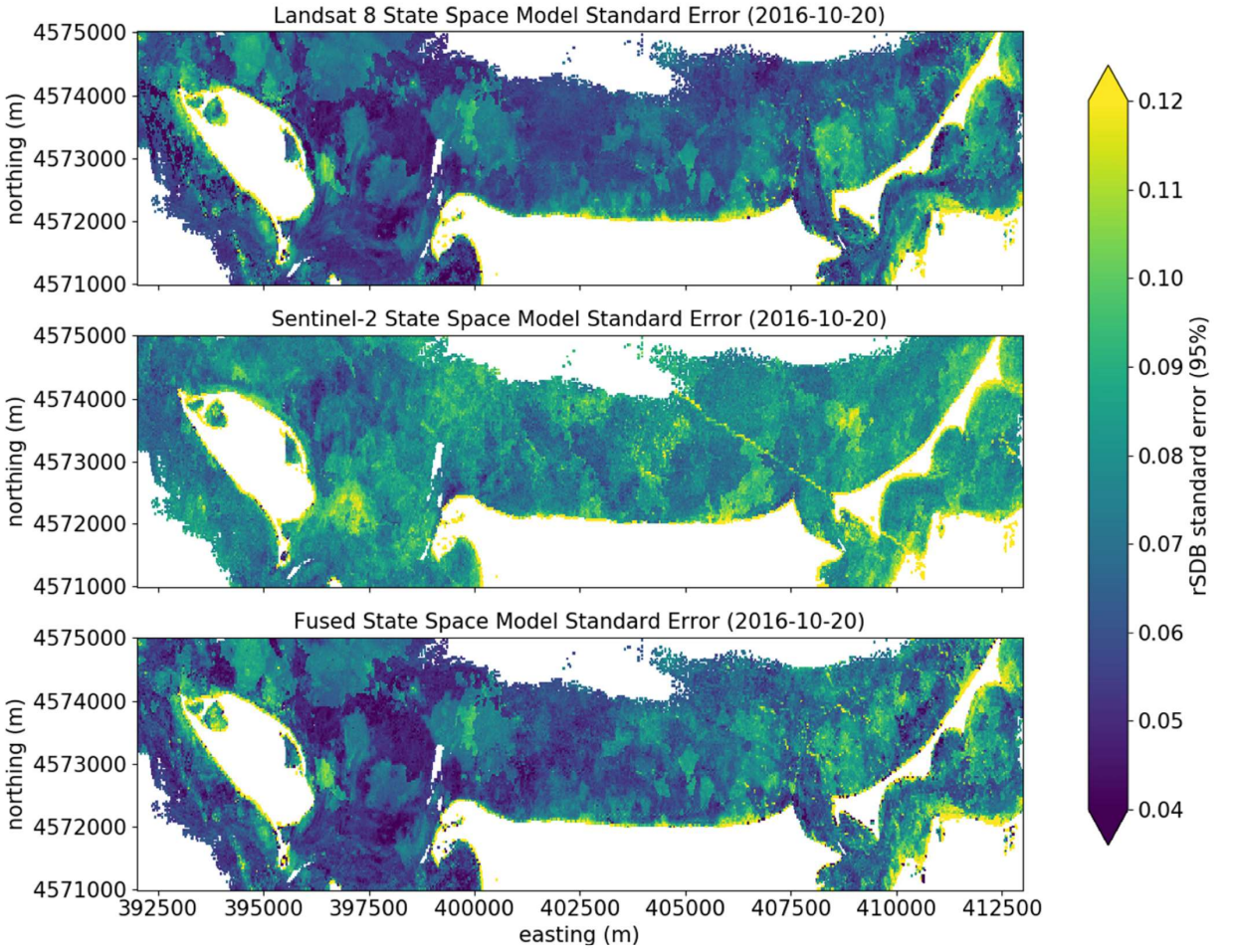

(a)

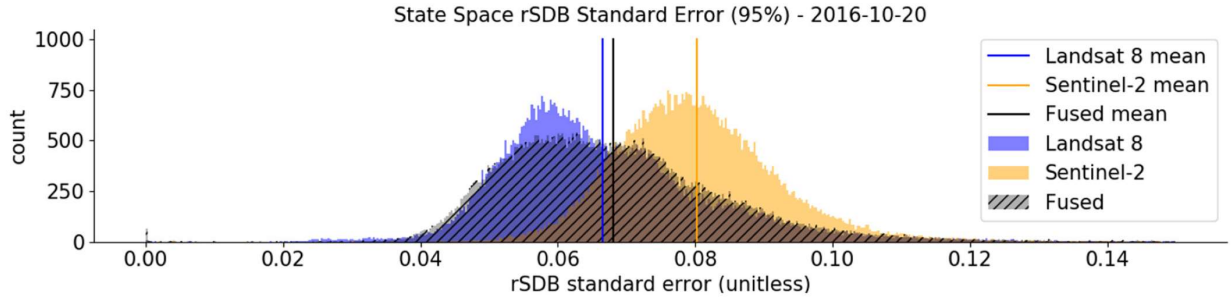

(b)

Figure 34: Map and Histogram of Residuals – (a) The spatial distribution of the standard errors of the Landsat 8, Sentinel-2, and data-fused models from 10/20/2016 are displayed with the same colormap to aid comparison. (The northwest-southeast trending linear feature observed in the Sentinel-2 standard error model corresponds to a contrail observed in the source multispectral data.) (b) The statistical distribution of the data-fused standard errors is more similar to the Landsat 8 model than the Sentinel-2 model, which is consistent with the expected behavior of the Kalman filter giving greater weight to the less uncertain observations.

Satellite Derived Bathymetry

The state space modeled SDB calculated from the transformation parameters generated using geographically weighted regression agreed with the reference bathymetry to within an RMSE of 0.29 m (μ = 0.01 m, σ = 0.29 m). Because the intent of this application of SDB was to evaluate the ability of state space modeling to portray relative bathymetry, it is important to not misinterpret the perhaps seemingly overoptimistic RMSE result. Although the reported RMSE is indeed an indicator of the agreement between the SDB and reference bathymetry, its main, intended value is as an indicator of the ability of the state space approach to model relative bathymetry via the rSDB parameter.

Detailed in Figure 35-a, the nature of the SDB residuals varies considerably over the AOI. In the area labeled A, the GWR SDB residuals form a nominally normal distribution with μ = 0.00 m and σ = 0.10 m (RMSE = 0.10 m). In the area labeled B, the GWR SDB residuals are more extreme and less normally distributed, with μ = 0.09 m and σ = 0.49 m (RMSE = 0.50 m). The spatial distribution of the GWR residuals in both areas reveals clear correlation with bottom characteristics, but noticeably more so in area B, where large along-shore variations coinciding with known eelgrass beds (DMCR, 2009) create a more leptokurtic distribution. To supplement interpreting the state space SDB results, the same areas were modeled using ordinary least squares, as shown in the rightmost images in Figure 35-b. Area A shows excellent agreement between the rSDB and reference bathymetry, with an R^2 of 0.97, while area B shows poor agreement, with an R^2 of 0.32.

Discussion

Three main benefits of the presented state space, multitemporal approach to SDB are the ability to (1) handle missing and erroneous data and create gap-free models of rSDB for a particular day, (2) generate not only a statistically based estimate of rSDB, but also a corresponding uncertainty, and (3) fuse multiple data sources.

Figure 36 illustrates the ability of state space modeling of rSDB time series to generate gap-free models from missing and noisy data. Despite numerous cloud occlusions and associated shadow effects in the Landsat 8 scene from 10/26/16, the state space approach produces a gap-free model of relative bathymetry. In addition to handling missing data due to obstructions such as cloud cover, the state space approach to modeling multitemporal SDB can also account for ephemeral noise, or outliers. Although numerous clouds in the scene were masked by the Acolite preprocessing steps, the associated shadows remained, with relatively low rSDB values (Figure 36-c). The state space modeling recognized the anomalously low values of rSDB and assigned them a low weight, effectively treating the shadows as outliers. Even without reference depths to generate the transformation parameters required to transform the rSDB to absolute bathymetry, the gap-free rSDB models provide internally consistent representations of

relative bathymetry for dates for which no multispectral data may be available or dates with compromised multispectral data quality.

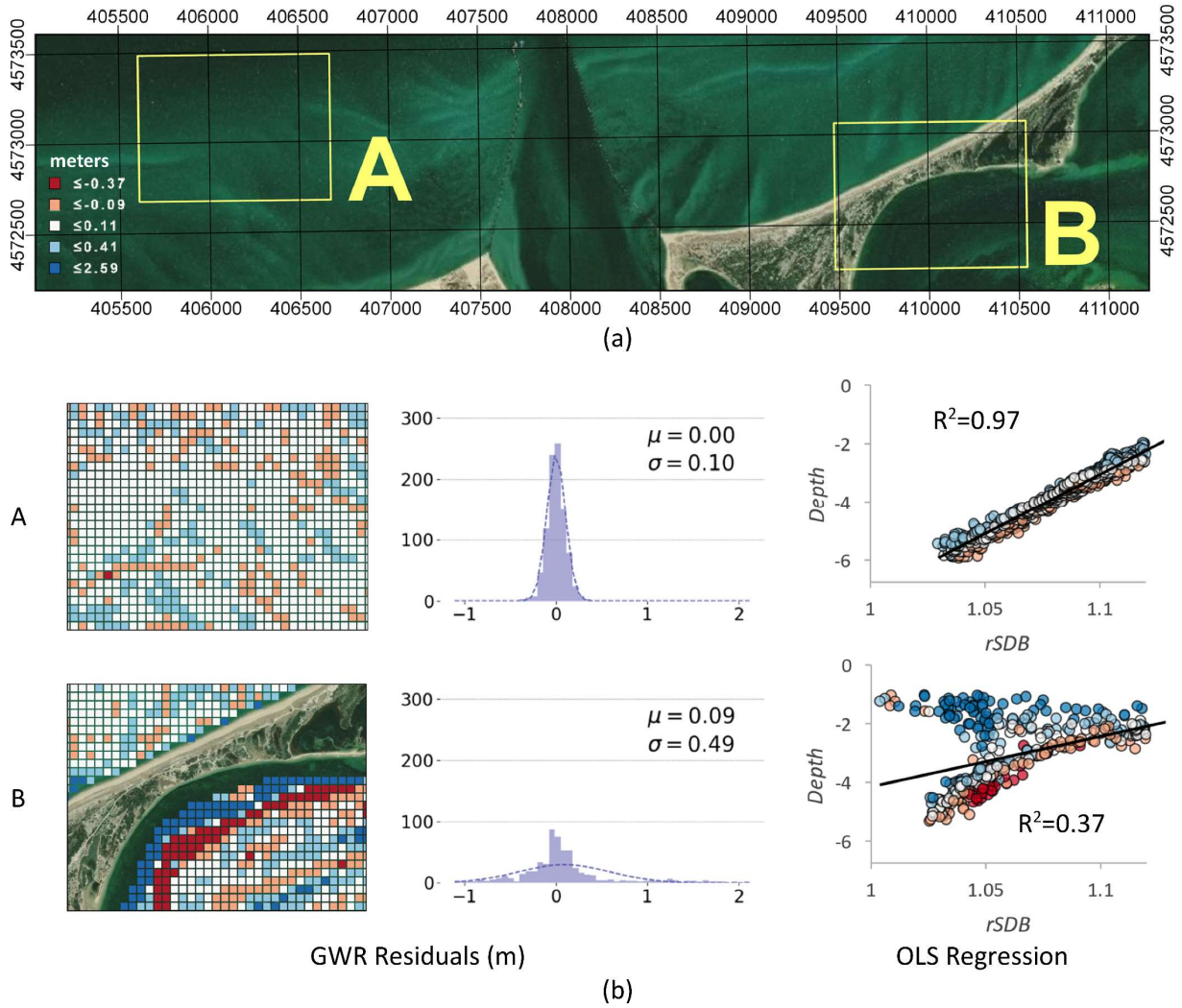

Figure 35: Map and Histogram of Residuals – The nature of the state space SDB residuals varies considerably over the AOI. Histograms and the spatial distributions of the GWR residuals are shown for two areas, labeled A and B. To supplement interpreting the state space SDB results, the same areas are modeled using ordinary least squares. The state space SDB and reference data in area A have excellent agreement, with an GWR RMSE of 0.10 m and an OLS R^2 of 0.97. The data in area B show considerably more variation, with a GWR RMSE of 0.50 m and an OLS R^2 of 0.37 m.

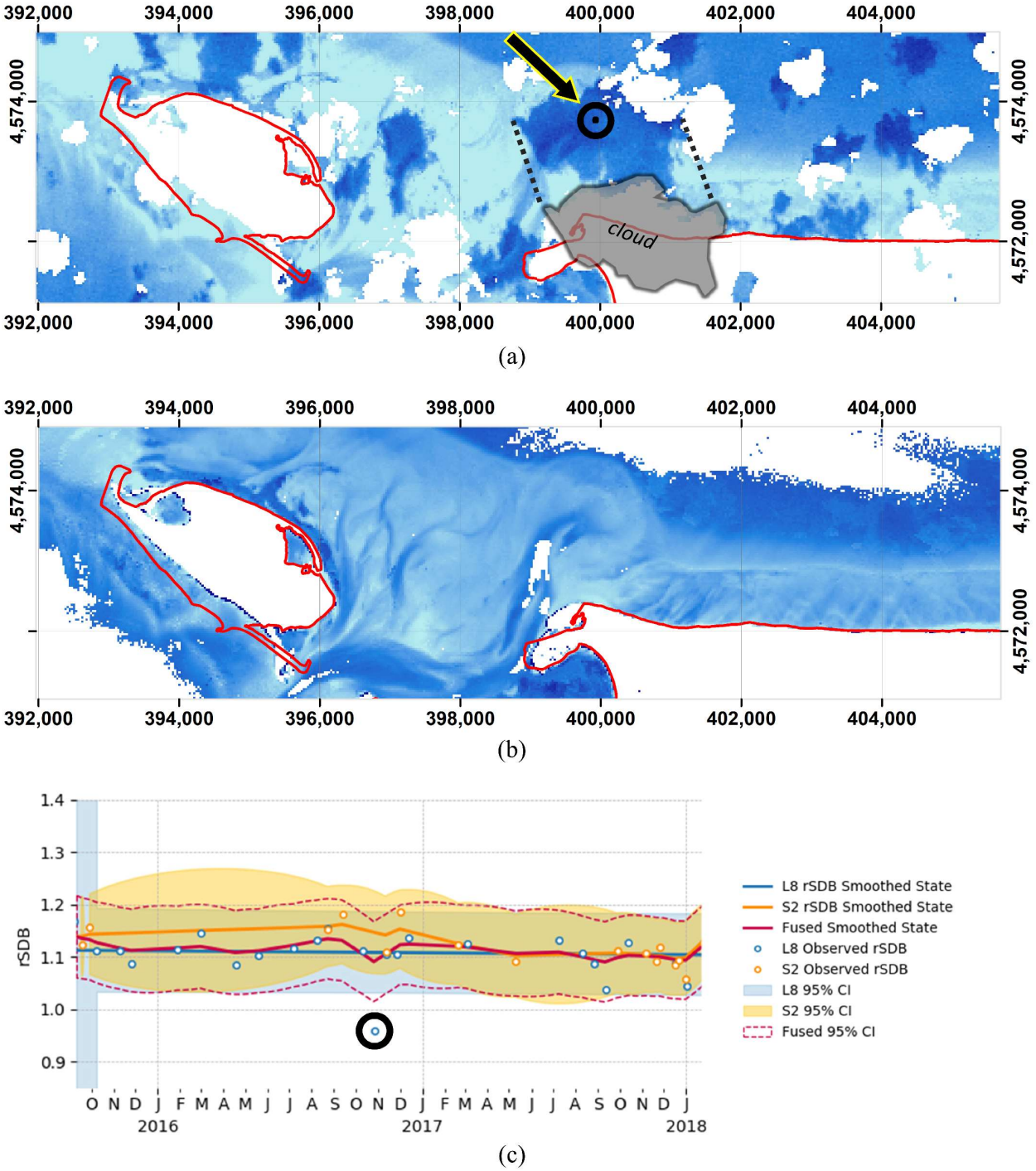

Figure 36: State space rSDB outlier detection – (a) The observed Landsat 8 rSDB from 10/26/16 has numerous cloud occlusions with associated shadows of anomalously low values. The SSMs for a single point (400380 E, 4573560 N), indicated by the black circle, are shown in subpanel *(c)*. (b) The occlusion-free Landsat 8 state space model of rSDB from 10/26/16 illustrates the ability of state space modeling to account for outliers and missing data. (c) The Landsat 8 state space model for the position highlighted in subpanel (a) effectively filters out the shadow artifact by assigning a low weight, as calculated by the Kalman gain, to the erroneous observation.

The ability to generate models of rSDB with corresponding uncertainties is a major advantage to the presented state space approach to multitemporal SDB. In general, uncertainty has received little attention in the SDB literature, with traditional assessments relying almost exclusively on the global RMSE statistic, which conflates the uncertainties of the underlying rSDB and reference bathymetry; however, a growing number of studies have broadened the characterization of SDB uncertainty, with approaches based on Monte Carlo simulations (Pe'eri et al., 2014) and analytical error propagation based on component radiometric and reference depth uncertainties (Freire, 2017). The presented state space approach contributes to the SDB uncertainty literature by offering a technique to robustly estimate the uncertainty of the underlying rSDB, beyond relying solely on instrument radiometric uncertainties, which do not capture the radiometric artifacts caused by the environment and corrections for atmosphere and sun-glint. Additionally, the approach provides uncertainty estimates for relative bathymetry that are not influenced by the uncertainty of the reference bathymetry data set used to derive transformation parameters.

In addition to providing the ability to generate gap-free models of rSDB with corresponding uncertainty estimates, the state space approach to multitemporal SDB provides the opportunity for fusing numerous multispectral datasets. This study was limited to Landsat 8 OLI and Sentinel-2 MSI data, but a number of other multispectral sensors have been used for SDB, as summarized by Forfinski-Sarkozi and Parrish (2019). The wide range of temporal and spatial resolutions of multispectral sensors may pose nontrivial multiscale and sensor-harmonization issues and may not be appropriate for every application, but the nature of state space modeling is such that more sensors can be readily incorporated into a model by providing an additional observation equation for each sensor, given that each observation equation reflects the same underlying state process.

Limitations and Error Sources

In addition to the advantages of generating gap-free rSDB models with corresponding uncertainty and providing a mechanism for fusing a diverse suite of multispectral sensors, the presented state space approach to multitemporal SDB has potential limitations and sources of error regarding data preprocessing, state space modeling, and assessment using GWR.

Preprocessing has the potential to introduce both radiometric and geometric errors into the spectral ratio data used to form the rSDB state space models. One such artifact was an abrupt change in rSDB corresponding to along-track banding observed in the corresponding RGB composites. Particularly apparent in scenes affected by sun-glint, such radiometric banding, which has been observed in other studies and attributed to detector-edge inconsistencies (ESA, 2019; Vanhellemont and Ruddick, 2016), was observed in the Sentinel-2 time series. Although atmosphere corrections were applied using an algorithm

specifically designed for coastal applications, such corrections characteristically have numerous assumptions, including ozone concentrations and atmospheric pressure, which are oftentimes quite generalized. Differences in Landsat 8 and Sentinel-2 performance characteristics are also important radiometric considerations, as discussed in a growing number of studies examining the consistency and fusion of Landsat 8 and Sentinel-2 data products. The two sensors show generally good radiometric agreement, but techniques such as vicarious gains (Pahlevan et al., 2019) and multi-band regression modeling (Chastain et al., 2019) have been used to account for small but statistically significant biases in various bands. Such sensor harmonization was considered outside the scope of the current study's objective of demonstrating the potential for state space modeling of SDB, although accounting for sensor biases would likely improve the performance of the data-fused models. Geometrically, resampling the Sentinel-2 rSDB data and the Chiroptera II reference bathymetric DEM to match the 30-m resolution of the Landsat 8 rSDB data was also a potential source of error during the preprocessing phase. A linear interpolator was chosen for simplicity, but other interpolation methods, such as cubic convolution or area-weighted interpolation could be considered in future implementations to minimize resampling errors. The approximately 38-m misalignment between Landsat 8 OLI and Sentinel-2 MSI documented in Storey et al. (2016) is also a potential source of error, as the Landsat 8 data available as of this study had not been processed with the latest Sentinel-2 global reference image (GRI) (USGS, n.d.). In addition to artifacts influenced by radiometric corrections and geometric adjustments, the presented approach is limited by relying solely on the blue and green bands. As reported by Caballero et al. (2019), incorporating red-edge bands can alleviate shoaling effects in shallow water.

Beyond radiometric and geometric errors, state space modeling has limitations potentially introducing errors. As described by Auger-Méthé et al. (2016), even simple state space models present parameter- and state-estimation issues, including variance biases and the inability to differentiate process stochasticity from measurement error. Additional research is needed to verify if the modeled variances in the state space SDB framework realistically capture measurement and process uncertainties. The SDB framework also potentially introduces error through the simplification of applying the same type of model to every pixel in the entire AOI. A more flexible approach would allow for different model types in different pixels to account to variations in time series characteristics. For example, a local linear model may be ideal for a bathymetrically stable area, but a local linear model with an additional trend term may be more appropriate for an area undergoing shoaling. Adding even more levels of complexity, such as trigonometric components to characterize cyclic phenomena such as migrating sand waves, changing water-levels/tides, and seasonal fluctuations, would also be possible. However, adding model complexity comes with increased computational costs and the potential for issues resulting from overfitting.

Another limitation of the presented state space method is that it operates on strictly a pixel-by-pixel basis, ignoring potentially useful local information. Incorporating neighborhood operations, such as kernel-based filtering, has the potential to reduce noisy estimates, such as the speckle observed in the Sentinel-2 space model results. Yet another potential source of error is that the state space modeling does not currently explicitly account for changing water levels. The Landsat 8 and Sentinel-2 acquisition times span the 0.9-m mean range (NOAA, n.d.) observed at the NOAA Nantucket water level gauge (station ID 8449130), centrally located in the AOI. In single-image SDB, the water-level is not considered an important parameter, because all pixels are typically assumed to reflect the same water level, with the vertical datum of the reference points dictating the vertical datum of the transformed SDB depths. However, in the presented state space multitemporal SDB approach, not all pixels in an "rSDB image," i.e., daily rSDB state space model, necessarily reflect the same, or a single, water level. This study adopts the simplifying assumptions that, given the multispectral data are well distributed throughout the local mean tide range, the state space model generated for any particular pixel represents an average water level and that the vertical datum of the reference depths determines the datum of the transformed SDB depths. In study areas with larger tide ranges or scenarios where the observed imagery data are not distributed throughout the tide range, such a simplifying assumption may not be appropriate. Future research plans to more rigorously account for tides include using the state space modeling method of unobserved components to identify diurnal and semidiurnal components in the observed rSDB time series.

In addition to the assumptions made during preprocessing and state space modeling, the simplifying assumption regarding the bandwidth in the GWR analysis is an important consideration when evaluating the transformed SDB and the associated residuals. If the bandwidth is too small, the local estimates will have large variance, and if the bandwidth is too large, the local estimates will have large bias. Despite the importance of the bandwidth, this study did not adopt a rigorous approach to setting the bandwidth, such as minimizing the Akaike Information Criterion (AIC) or the cross-validation (CV) score. The purpose of the GWR analysis was to nominally characterize the local performance of the state space modeling approach, not find the statistically optimal balance between local bias and variance, which can be difficult to accurately capture, given a number of theoretical and technical issues with GWR (Cho et al., 2010). Su et al. (2014) used a similar heuristic approach, whereby an adaptive bandwidth of 30 was used to derive local SDB coefficients.

Computational Complexity

The Landsat 8 and Sentinel-2 suites of daily SSMs spanning the 1264-day period from 9/1/15 to 2/5/19 each took between 2.5 and 3 hrs to generate. With 64,588 30-m cells per daily model, the computation rate was 6-8 state space models per second. The suite of data-fused SSMs took 3.75 hrs to

generate, at a computation rate of 4 models per second. A number of factors influence the computational complexity and, in turn, the accessibility and operational feasibility of the proposed state space approach. One immediate factor is the length of time series used to generate the SSMs. For example, creating a suite of daily Landsat 8 models for only half of the original period approximately doubles the model-computation rate. At a broader level, the mode of state space modeling also effects computational complexity. Whereas the presented SDB approach performs Kalman smoothing, which uses data from before and after a particular time, an approach performing Kalman filtering would only use prior data. The Python package used to implement the SSM approach, statsmodels, is also a major factor. Although much of the core statsmodels state space functionality relies on Cython, which provides access to fast C-based static typing, statsmodels does not necessarily provide the most efficient platform for implementing multitemporal SDB. For example, because statsmodels was developed for macroeconomic applications using fixed datasets, incremental Kalman filtering was not available, although recent development addresses such options (Statsmodels, n.d.). Relying on incremental Kalman techniques to efficiently incorporate new observations would be a significant advantage in an operational setting.

Implications for Global Bathymetric Databases

A state space approach to multitemporal SDB has significant implications for global bathymetric databases. Particularly as recent advances in cloud storage and distributed computing facilitate analysis of 'Big Earth Data' (Chi et al., 2016; Corbane et al., 2017), state space modeling offers a mechanism to derive bathymetry in the difficult-to-map nearshore zone on a global scale. A variety of government (EMODnet, 2018), international (GEBCO, n.d.), and commercial endeavors (Corbley, 2018; Hartmann et al., 2017) already incorporate SDB in bathymetric databases, but these databases do not leverage the bathymetric information contained in, or the uncertainty analyses afforded by, entire time series of multispectral data.

Extending the notion of data fusion beyond the multispectral data to include the corresponding reference bathymetry, the state space approach becomes even more flexible. In scenarios with limited temporal coverage of reference bathymetry, including the reference bathymetry in the state space model may not be advantageous, but doing so could be highly advantageous in scenarios with (near) repeating sources of bathymetry, such as that afforded by the ICESat-2 mission (Forfinski-Sarkozi and Parrish, 2019; Parrish et al., 2019). With repeat sources of bathymetry and the assumption that a change in rSDB implies a change in depth, estimates of bathymetry based on the current transformation parameters could be corrected based on new absolute depth measurements, analogous to how GNSS observations update estimates of positions made from inertial sensors in GNSS-aided inertial navigation. In turn, new transformation parameters could then be calculated. Granted, the corresponding update rates are vastly larger with GNSS-aided inertial navigation (200 Hz) than those for the SDB use case (7×10^{-7} Hz), but both

cases demonstrate the concept of updating a state space model incorporating relative measurements with absolute measurements. In addition to ICESat-2 bathymetry, crowd-sourced bathymetry (IHO, 2018b) offers a potential source of reference depths at update rates greater than those traditionally offered by conventional survey schedules.

Conclusion

This study has shown state space modeling of rSDB to be a viable approach to capturing bathymetric information from time series of multispectral imagery, with the potential to significantly extend the scope of existing SDB algorithms by generating daily models of rSDB, including per-pixel uncertainty estimates, that account for missing data and ephemeral environmental noise. Being able to model rSDB for an arbitrary date allows SDB to be calculated for precisely the date associated with available reference bathymetry and not simply the date of the, for example, closest-in-time multispectral image. Particularly in bathymetrically dynamic areas, using rSDB spatiotemporally coincident with reference depths is crucial to minimizing uncertainty in derived SDB values. In addition to generating sensor-specific models, the state space approach offers promise as a data-fusion method capable of incorporating time series from a diverse suite of multispectral sensors. The accuracy of the approach was assessed by examining the geographically weighted regression residual errors of rSDB transformed using a 1-to-1 correspondence of all rSDB values and reference bathymetry. Overall, the SDB generated from the Landsat 8 rSDB model for 10/20/2016 agreed with the reference bathymetry to within an RMSE of 0.29 m. Examination of the spatial distribution of the residuals provided a mechanism for assessing the local performance of the approach, with the best results occurring in areas void of eelgrass. Future research opportunities include extending the data-fusion approach to include multiple sources of reference depths, including near-repeat ICESat-2 depths, and more-sophisticated model components depicting trends, tides, and seasonality. State space analysis for multispectral rSDB time series also affords a previously unexplored opportunity to leverage recent advances in distributed computing and cloud storage to generate global spatiotemporal databases of SDB from time series of multispectral data.

CONCLUSION

This dissertation presented two spaceborne approaches to reduce the global shortage of nearshore bathymetry known as "the white ribbon," referring to the alongshore empty space observed on numerous nautical charts. Presented in two published studies, the first approach was a completely spaceborne active/passive data fusion technique potentially leveraging the 532-nm (green) wavelength photon-counting ATLAS sensor onboard the ICESat-2 satellite. Bathymetry detected in ICESat-2 ATLAS data would only be along narrow tracklines, but synergistically combining it with empirical multispectral SDB would allow depth estimation over regional and possibly global scales. Because ICESat-2 was launched just prior to the publication of the second study, ATLAS data were not available during the writing and peer-review of either study. Instead, the data analyzed in these publications were from MABEL, NASA's high-altitude ICESat-2 simulator system designed to provide ATLAS-like data for algorithm development. The second approach to reducing the global shortage of nearshore bathymetry was applying state space modeling to multispectral times series to generate gap-free models of relative SDB (rSDB) with corresponding uncertainty estimates. Whether used to model a single time series or fuse time series from multiple sensors, state space modeling offers a previously unexplored mechanism for multitemporal SDB.

Active/Passive Spaceborne Data Fusion

The first study (Forfinski-Sarkozi and Parrish, 2016) demonstrated the high-altitude photon-counting lidar MABEL capable of detecting bathymetry in up to 8 meters water depth in Keweenaw Bay, Lake Superior. Although the assessed accuracy of the MABEL-derived bathymetry is beyond IHO specifications for navigational safety, the refraction- and datum-corrected data are valuable to a number of nearshore applications. With the aim of extending the analysis toward ICESat-2 ATLAS once important system parameters became available, the first study also presented a baseline version of the lidar equation to predict the number of photoelectron returns based on water depth. Despite that MABEL was not intended for radiometric analysis, the observed numbers of photoelectrons showed general (order-of-magnitude) agreement with the prediction model. In general, the MABEL analyses suggested the potential for spaceborne bathymetry.

The second study (Forfinski-Sarkozi and Parrish, 2019) fully developed the active/passive spaceborne data fusion approach by synergistically fusing MABEL-derived bathymetry with multispectral Landsat 8 OLI imagery to successfully derive bathymetry over a large portion of Keweenaw Bay, Lake Superior. Beyond demonstrating that high-altitude photon-counting lidar data can be used to tune empirical SDB algorithms to infer depths well beyond the extents of available lidar data, this study presented a spatiotemporal analysis assessing where and when the data fusion approach might be viable. Results depicting where anticipated nearshore ICESat-2 tracklines intersect monthly Jerlov optical water type 1 and

3 polygons, as generated from VIIRS Kd(490) data, indicate that the proposed active/passive data fusion approach would be viable over large portions of the globe over the course of year. Even in areas prone to high turbidity or cloud cover, the spaceborne active/passive data fusion approach has potential to generate bathymetry, given that ICESat-2's near-repeat orbit will provide multiple opportunities to detect bathymetry.

State Space Modeling for Empirical Multispectral Satellite Derived Bathymetry

The final study demonstrated that state space modeling is a viable approach to multitemporal SDB by generating internally consistent gap-free daily models of rSDB, including per-pixel uncertainties. State space models (SSMs) have been shown capable of modeling single multispectral time series and fusing multiple time series from various multispectral sensors, including accounting for missing data and ephemeral environmental noise, such as cloud cover and sediment plumes. Multitemporal SDB employing SSMs has significant implications for the active/passive spaceborne data fusion method presented in the first two studies. Being able to model rSDB for an arbitrary date allows SDB to be calculated for precisely the date associated with available reference bathymetry and not simply the date of the, for example, closest-in-time multispectral image. Particularly in bathymetrically dynamic areas, using rSDB spatiotemporally coincident with reference depths is crucial to minimizing uncertainty in derived SDB values. SSMs, by extension, have significant implications for populating bathymetric databases and reducing the widespread shortage of nearshore bathymetry known as the "white ribbon."

Future Work

An accessible next step is to apply the active/passive data fusion method to the recently documented ICESat-2 ATLAS bathymetry (Parrish et al., 2019), incorporating rSDB generated with state space modeling. Beyond using the local linear state space model as presented, components depicting trends and seasonality could be included to more rigorously capture bathymetric dynamics. Times series from additional multispectral sensors could also be included to complement Sentinel-2 and Landsat 8 data. A longer-term research goal is to unify the presented data fusion and state space approaches into a broader bathymetric data fusion framework incorporating multiple sources of reference depths. As proposed in Figure 37, such a framework could include bathymetry with vastly different resolutions and uncertainties, ranging from high-resolution, low-uncertainty, well-documented hydrographic surveys satisfying rigorous IHO navigation specifications to low-resolution, high-uncertainty, sparsely documented crowd sourced trackline profiles. Extending the notion of data fusion to include the reference bathymetry in the underlying state equation(s), the state space approach becomes even more flexible. With the assumption that a change in rSDB implies a change in depth, estimates of bathymetry based on the current transformation parameters

and changes in rSDB could be corrected based on new reference bathymetry, and in turn, new transformation parameters could be calculated.

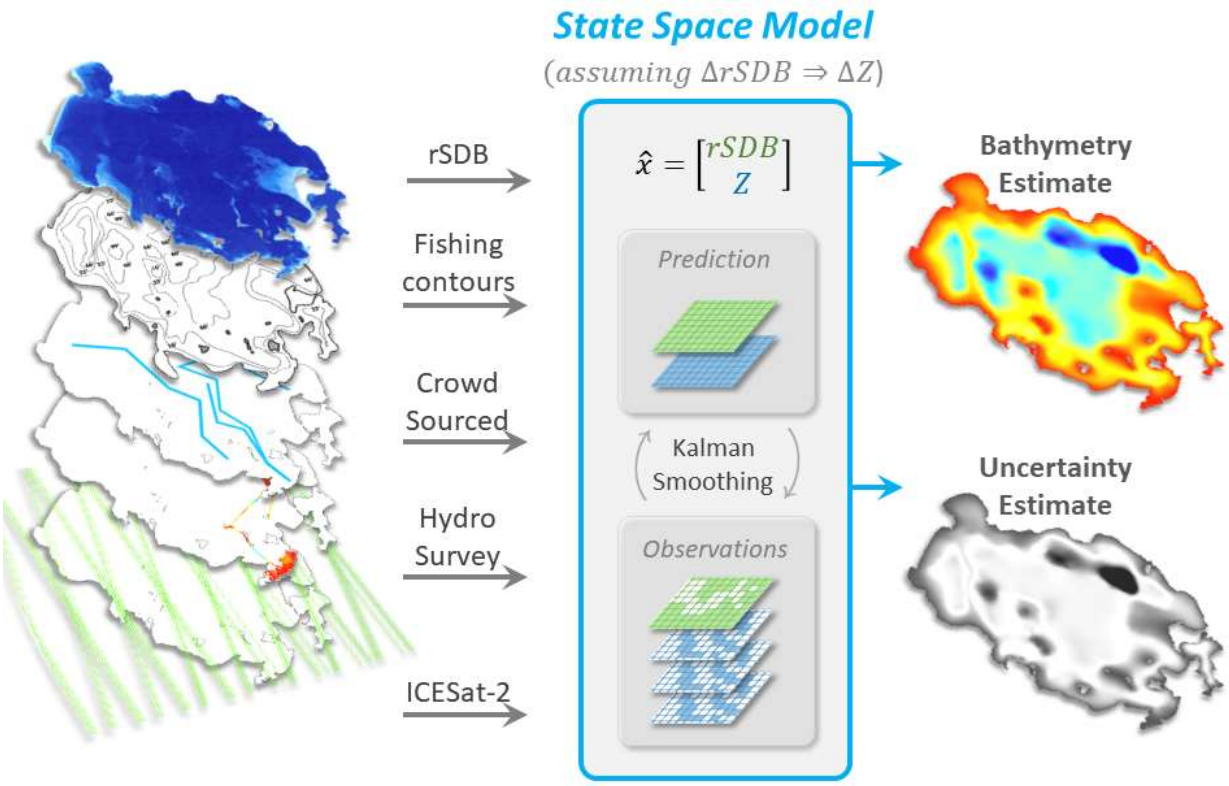

Figure 37. Prototype Bathymetry Data Fusion Framework – Based on the assumption that a change in rSDB implies a change in depth (Z), the state space model underlying the bathymetric data fusion framework can incorporate data from various multispectral sensors and sources of reference depths to generate gap-free models of bathymetry with corresponding uncertainty.

State space modeling of bathymetry has significant implications for a variety of nearshore applications, such as navigation and modeling inundation, sea level rise, and sediment transport. Statistically modeling time series of noisy, incomplete multispectral imagery and bathymetry to generate, in turn, gap-free time series of bathymetry has the potential to reveal insight into processes at a variety of spatiotemporal scales. Even changes in relative bathymetry, alone, could reveal meaningful insight into bathymetric dynamics. For example, examining the migration of sand waves and alongshore troughs could help coastal managers understand the effect of sea-level rise and changing wave-energy regimes on beach-nourishment practices. Especially with recent advances in cloud storage and distributed computing, a bathymetric data fusion framework incorporating state space modeling of multispectral imagery and

reference depths from diverse sources offers a previously unexplored mechanism to derive bathymetry and examine the associated dynamics on a global scale.

BIBLIOGRAPHY

Abdalati, W., Zwally, H.J., Bindschadler, R., Csatho, B., Farrell, S.L., Fricker, H.A., Harding, D., Kwok, R., Lefsky, M., Markus, T., Marshak, A., Neumann, T., Palm, S., Schutz, B., Smith, B., Spinhirne, J., Webb, C., 2010. The ICESat-2 Laser Altimetry Mission. Proceedings of the IEEE 98, 735–751. https://doi.org/10.1109/JPROC.2009.2034765

Abdallah, H., Bailly, J.S., Baghdadi, N.N., Saint-Geours, N., Fabre, F., 2013. Potential of Space-Borne LiDAR Sensors for Global Bathymetry in Coastal and Inland Waters. IEEE Journal of Selected Topics in Applied Earth Observations and Remote Sensing 6, 202–216. https://doi.org/10.1109/JSTARS.2012.2209864

Abshire, J.B., Sun, X., Riris, H., Sirota, J.M., McGarry, J.F., Palm, S., Yi, D., Liiva, P., 2005. Geoscience Laser Altimeter System (GLAS) on the ICESat Mission: On-orbit measurement performance. Geophysical Research Letters 32. https://doi.org/10.1029/2005GL024028

Alikas, K., Kratzer, S., Reinart, A., Kauer, T., Paavel, B., 2015. Robust remote sensing algorithms to derive the diffuse attenuation coefficient for lakes and coastal waters: Algorithm for diffuse attenuation coefficient. Limnology and Oceanography: Methods 13, 402–415. https://doi.org/10.1002/lom3.10033

Allerton, D.J., Jia, H., 2005. A Review of Multisensor Fusion Methodologies for Aircraft Navigation Systems. Journal of Navigation 58, 405–417. https://doi.org/10.1017/S0373463305003383

Arroyo-Suarez, E.N., Riley, J.L., Glang, C.D.R., Mabey, L.T., n.d. Evaluating a global differential GPS system for hydrographic surveying, in: Proceedings of MTS IEEE OCEANS. Washington, D.C., USA, 18-23 September 2005, pp. 2557–2563.

Arsen, A., Crétaux, J.-F., Berge-Nguyen, M., del Rio, R., 2013. Remote Sensing-Derived Bathymetry of Lake Poopó. Remote Sensing 6, 407–420. https://doi.org/10.3390/rs6010407

Auger-Méthé, M., Field, C., Albertsen, C.M., Derocher, A.E., Lewis, M.A., Jonsen, I.D., Mills Flemming, J., 2016. State-space models' dirty little secrets: even simple linear Gaussian models can have estimation problems. Scientific Reports 6. https://doi.org/10.1038/srep26677

Awadallah, M., Ghannam, S., Abbott, L., Ghanem, A., n.d. A two-stage algorithm for extraction of ground and top of canopy in photon-counting profiling-LiDAR data in preparation for the ICESat-2 mission, in: IEEE Geoscience and Remote Sensing Symposium (IGARSS). Quebec City, QC, Canada, 13-18 July 2014, pp. 1353–1356.

Bai, K., Chang, N.-B., Chen, C.-F., 2016. Spectral Information Adaptation and Synthesis Scheme for Merging Cross-Mission Ocean Color Reflectance Observations From MODIS and VIIRS. IEEE Transactions on Geoscience and Remote Sensing 54, 311–329. https://doi.org/10.1109/TGRS.2015.2456906

Barkby, S., Williams, S., Pizarro, O., Jakuba, M., 2009. An efficient approach to bathymetric SLAM, in: 2009 IEEE/RSJ International Conference on Intelligent Robots and Systems. Presented at the 2009 IEEE/RSJ International Conference on Intelligent Robots and Systems (IROS 2009), IEEE, St. Louis, MO, USA, pp. 219–224. https://doi.org/10.1109/IROS.2009.5354248

Benny, A.H., Dawson, G.J., 1983. Satellite Imagery as an Aid to Bathymetric Charting in the Red Sea. The Cartographic Journal 20, 5–16. https://doi.org/10.1179/caj.1983.20.1.5

Biberhofer, J., 2002. Aquatic Substrate Mapping in Support of the Keweenaw Bay Indian Community's Conservation Management Objectives. Environment Canada, National Water Research Institute., Burlington, Ontario, Canada.

Birrien, F., Castelle, B., Marieu, V., Dubarbier, B., 2013. On a data-model assimilation method to inverse wave-dominated beach bathymetry using heterogeneous video-derived observations. Ocean Engineering 73, 126–138. https://doi.org/10.1016/j.oceaneng.2013.08.002

Bramante, J.F., Raju, D.K., Sin, T.M., 2013. Multispectral derivation of bathymetry in Singapore's shallow, turbid waters. International Journal of Remote Sensing 34, 2070–2088. https://doi.org/10.1080/01431161.2012.734934

Brunt, K., 2016. (Cryospheric Sciences Laboratory, NASA Goddard Space Flight Center, Greenbelt, MD, USA). Personal communication,.

Brunt, K.M., Neumann, T.A., Amundson, J.M., Kavanaugh, J.L., Moussavi, M.S., Walsh, K.M., Cook, W.B., Markus, T., 2016. MABEL photon-counting laser altimetry data in Alaska for ICESat-2 simulations and development. The Cryosphere 10, 1707–1719. https://doi.org/10.5194/tc-10-1707-2016

Brunt, K.M., Neumann, T.A., Walsh, K.M., Markus, T., 2014. Determination of Local Slope on the Greenland Ice Sheet Using a Multibeam Photon-Counting Lidar in Preparation for the ICESat-2 Mission. IEEE Geoscience and Remote Sensing Letters 11, 935–939. https://doi.org/10.1109/LGRS.2013.2282217

Brusch, S., Held, P., Lehner, S., Rosenthal, W., Pleskachevsky, A., 2011. Underwater bottom topography in coastal areas from TerraSAR-X data. International Journal of Remote Sensing 32, 4527–4543. https://doi.org/10.1080/01431161.2010.489063

Caballero, I., Stumpf, R.P., Meredith, A., 2019. Preliminary Assessment of Turbidity and Chlorophyll Impact on Bathymetry Derived from Sentinel-2A and Sentinel-3A Satellites in South Florida. Remote Sensing 11, 645. https://doi.org/10.3390/rs11060645

Calkoen, C.J., Hesselmans, G.H.F.M., Wensink, G.J., Vogelzang, J., 2001. The Bathymetry Assessment System: Efficient depth mapping in shallow seas using radar images. International Journal of Remote Sensing 22, 2973–2998. https://doi.org/10.1080/01431160116928

Castanedo, F., 2013. A Review of Data Fusion Techniques. The Scientific World Journal 2013, 1–19. https://doi.org/10.1155/2013/704504

Ceyhun, Ö., Yalçın, A., 2010. Remote sensing of water depths in shallow waters via artificial neural networks. Estuarine, Coastal and Shelf Science 89, 89–96. https://doi.org/10.1016/j.ecss.2010.05.015

Chamberlin, C., Arcas, D., 2015. Modeling Tsunami Inundation for Hazard Mapping at Everett, Washington, from the Seattle Fault (NOAA Technical Memorandum OAR PMEL-147). National

Oceanic and Atmospheric Administration, Pacific Marine Environmental Laboratory, Seattle, WA, USA.

Chastain, R., Housman, I., Goldstein, J., Finco, M., Tenneson, K., 2019. Empirical cross sensor comparison of Sentinel-2A and 2B MSI, Landsat-8 OLI, and Landsat-7 ETM+ top of atmosphere spectral characteristics over the conterminous United States. Remote Sensing of Environment 221, 274–285. https://doi.org/10.1016/j.rse.2018.11.012

Chi, M., Plaza, A., Benediktsson, J.A., Sun, Z., Shen, J., Zhu, Y., 2016. Big Data for Remote Sensing: Challenges and Opportunities. Proceedings of the IEEE 104, 2207–2219. https://doi.org/10.1109/JPROC.2016.2598228

Cho, S.-H., Lambert, D.M., Chen, Z., 2010. Geographically weighted regression bandwidth selection and spatial autocorrelation: an empirical example using Chinese agriculture data. Applied Economics Letters 17, 767–772. https://doi.org/10.1080/13504850802314452

Chust, G., Galparsoro, I., Borja, Á., Franco, J., Uriarte, A., 2008. Coastal and estuarine habitat mapping, using LIDAR height and intensity and multi-spectral imagery. Estuarine, Coastal and Shelf Science 78, 633–643. https://doi.org/10.1016/j.ecss.2008.02.003

Clark, R.K., Fay, T.H., Walker, C.L., 1987. Bathymetry calculations with Landsat 4 TM imagery under a generalized ratio assumption. Applied Optics 26, 4036–4038.

Collin, A., Hench, J.L., 2012. Towards Deeper Measurements of Tropical Reefscape Structure Using the WorldView-2 Spaceborne Sensor. Remote Sensing 4, 1425–1447. https://doi.org/10.3390/rs4051425

Conger, C.L., Hochberg, E.J., Fletcher, C.H., Atkinson, M.J., 2006. Decorrelating remote sensing color bands from bathymetry in optically shallow waters. IEEE Transactions on Geoscience and Remote Sensing 44, 1655–1660. https://doi.org/10.1109/TGRS.2006.870405

Cook, W.B., 2016. (NASA Goddard Space Flight Center, Greenbelt, MD, USA). Personal communication,.

Corbane, C., Pesaresi, M., Politis, P., Syrris, V., Florczyk, A.J., Soille, P., Maffenini, L., Burger, A., Vasilev, V., Rodriguez, D., Sabo, F., Dijkstra, L., Kemper, T., 2017. Big earth data analytics on Sentinel-1 and Landsat imagery in support to global human settlements mapping. Big Earth Data 1, 118–144. https://doi.org/10.1080/20964471.2017.1397899

Corbley, K., 2018. MG3 & Satellite Derived Bathymetry. Marine Technology Reporter 4.

Cossio, T., Slatton, K.C., Carter, W., Shrestha, K., Harding, D., 2009. Predicting Topographic and Bathymetric Measurement Performance for Low-SNR Airborne Lidar. IEEE Transactions on Geoscience and Remote Sensing 47, 2298–2315. https://doi.org/10.1109/TGRS.2008.2011054

De Bernardis, C., Vicente-Guijalba, F., Martinez-Marin, T., Lopez-Sanchez, J., 2016. Particle Filter Approach for Real-Time Estimation of Crop Phenological States Using Time Series of NDVI Images. Remote Sensing 8, 610. https://doi.org/10.3390/rs8070610

Degnan, J.J., 2002. Photon-counting multikilohertz microlaser altimeters for airborne and spaceborne topographic measurements. Journal of Geodynamics 34, 503–549.

Deidda, M., Pala, A., Sanna, G., 2016. A new IDL implementation of the Jupp method for bathymetry extraction in shallow waters. ISPRS - International Archives of the Photogrammetry, Remote Sensing and Spatial Information Sciences XLI-B7, 467–474. https://doi.org/10.5194/isprsarchives-XLI-B7-467-2016

deRada, S., Ladner, S., Arnone, R.A., 2012. Coupling ocean models and satellite derived optical fields to estimate LIDAR penetration and detection performance, in: Remote Sensing of the Ocean, Sea Ice, Coastal Waters, and Larege Water Regions. Presented at the SPIE Remote Sensing, Edinburgh, Scotland, pp. 85320T-8532–8.

Deronde, B., Houthuys, R., Debruyn, W., Fransaer, D., Lancker, V.V., Henriet, J.-P., 2006. Use of Airborne Hyperspectral Data and Laserscan Data to Study Beach Morphodynamics along the Belgian Coast. Journal of Coastal Research 225, 1108–1117. https://doi.org/10.2112/04-0264.1

DMCR, 2009. Nantucket and Madaket Harbors Action Plan. The Nantucket and Madaket Harbors Plan Review Committee & the Department of Marine and Coastal Resources.

Dodd, D., Mills, J., 2011. Ellipsoidally referenced surveys: Issues and solutions. The International Hydrographic Review 6, 19–30.

Durbin, J., Koopman, S.Jan., 2012. Time series analysis by state space methods. Oxford University Press, Oxford.

Eakins, B.W., Grothe, P.R., 2014. Challenges in Building Coastal Digital Elevation Models. Journal of Coastal Research 942–953. https://doi.org/10.2112/JCOASTRES-D-13-00192.1

Effler, S.W., Perkins, M., Peng, F., Strait, C., Weidemann, A.D., Auer, M.T., 2010. Light-absorbing components in Lake Superior. Journal of Great Lakes Research 36, 656–665. https://doi.org/10.1016/j.jglr.2010.08.001

Elaksher, A.F., 2008. Fusion of hyperspectral images and lidar-based dems for coastal mapping. Optics and Lasers in Engineering 46, 493–498. https://doi.org/10.1016/j.optlaseng.2008.01.012

Elmenreich, W., 2002. An introduction to sensor fusion (No. 47/2001). Vienna University of Technology, Austria.

EMODnet, 2018. EMODnet Digital Bathymetry (DTM 2018). https://doi.org/10.12770/18ff0d48-b203-4a65-94a9-5fd8b0ec35f6

EMODNET Coastal Mapping [WWW Document], n.d. URL http://coastal-mapping.eu/ (accessed 8.28.16).

ESA, 2019. S2 MPC: L1C Data Quality Report (Ref. S2-PDGS-MPC-DQR).

ESA, 2015. Sentinel-2 User Handbook 64.

ESRI, Garmin International, Inc., 2017. World Water Bodies URL: https://www.arcgis.com/home/item.html?id=e750071279bf450cbd510454a80f2e63 (last date accessed: 4 July 2017) [WWW Document]. URL (accessed 7.4.17).

Farrell, S.L., Markus, T., Kwok, R., Connor, L., 2011. Laser altimetry sampling strategies over sea ice. Annals of Glaciology 52, 69–76.

Feygels, V., Aitken, J., Ramnath, V., Duong, H., Marthouse, R., Smith, B., Clark, N., Renz, E., Reisser, J., Kopilevich, Y., 2017. Coastal zone mapping and imaging lidar (CZMIL) participation in the ocean cleanup's aerial expedition project, in: OCEANS 2017 - Anchorage. Presented at the OCEANS 2017 - Anchorage, pp. 1–7.

Figueiredo, I.N., Pinto, L., Goncalves, G., 2016. A Modified Lyzenga's Model for Multispectral Bathymetry Using Tikhonov Regularization. IEEE Geoscience and Remote Sensing Letters 13, 53–57. https://doi.org/10.1109/LGRS.2015.2496401

Finkl, C.W., Benedet, L., Andrews, J.L., 2005. Interpretation of Seabed Geomorphology Based on Spatial Analysis of High-Density Airborne Laser Bathymetry. Journal of Coastal Research 501–514. https://doi.org/10.2112/05-756A.1

Fitzpatrick, A.A.W., Hubbard, A.L., Box, J.E., Quincey, D.J., van As, D., Mikkelsen, A.P.B., Doyle, S.H., Dow, C.F., Hasholt, B., Jones, G.A., 2014. A decade (2002 - 2012) of supraglacial lake volume estimates across Russell Glacier, West Greenland. The Cryosphere 8, 107–121. https://doi.org/10.5194/tc-8-107-2014

Fonstad, M.A., Marcus, W.A., 2005. Remote sensing of stream depths with hydraulically assisted bathymetry (HAB) models. Geomorphology 72, 320–339. https://doi.org/10.1016/j.geomorph.2005.06.005

Forfinski-Sarkozi, N., Parrish, C., 2016. Analysis of MABEL Bathymetry in Keweenaw Bay and Implications for ICESat-2 ATLAS. Remote Sensing 8, 772. https://doi.org/10.3390/rs8090772

Forfinski-Sarkozi, N.A., Parrish, C.E., 2019. Active-Passive Spaceborne Data Fusion for Mapping Nearshore Bathymetry. Photogrammetric Engineering & Remote Sensing 85, 281–295. https://doi.org/10.14358/PERS.85.4.281

Freire, R.R., 2017. Evaluating Satellite Derived Bathymetry in Regard to Total Propagated Uncertainty, Multi-Temporal Change Detection, and Multiple Non-Linear Estimation. University of New Hampshire.

Gao, J., 2009. Bathymetric mapping by means of remote sensing: methods, accuracy and limitations. Progress in Physical Geography 33, 103–116. https://doi.org/10.1177/0309133309105657

GEBCO, n.d. General Bathymetric Chart of the Oceans (GEBCO) [WWW Document]. URL http://www.gebco.net/ (accessed 8.25.16).

Gianinetto, M., Lechi, G., 2004. A DNA algorithm for the batimetric mapping in the lagoon of Venice using QuickBird multispectral data. Int. Archive of the Photogrammetry, Remote Sensing and Spatial Information Sciences 35.

Giardino, C., Bresciani, M., Cazzaniga, I., Schenk, K., Rieger, P., Braga, F., Matta, E., Brando, V., 2014. Evaluation of Multi-Resolution Satellite Sensors for Assessing Water Quality and Bottom Depth of Lake Garda. Sensors 14, 24116–24131. https://doi.org/10.3390/s141224116

Giese, G.S., Williams, S.J., Adams, M., 2015. Coastal landforms and processes at the Cape Cod National Seashore, Massachusetts—A primer (Report No. 1417), Circular. Reston, VA. https://doi.org/10.3133/cir1417

Gilg, J.G., McConnel, Jr., J.J., 1966. Non-Existent Seamounts -- A Case Study, Informal Manuscript No. IM66-28. U.S. Naval Oceanographic Office, Washington, D.C.

Gilvear, D., Tyler, A., Davids, C., 2004. Detection of estuarine and tidal river hydromorphology using hyper-spectral and LiDAR data: Forth estuary, Scotland. Estuarine, Coastal and Shelf Science 61, 379–392. https://doi.org/10.1016/j.ecss.2004.06.007

Glennie, C., 2016. (National Center for Airborne Laser Mapping, University of Houston, Houston, TX, USA). Unpublished Data,.

Guenther, G.C., 2007. Airborne lidar bathymetry, in: Digital Elevation Model Technologies and Applications: The DEM Users Manual. American Society for Photogrammetry and Remote Sensing, Bethesda, MD, pp. 253–320.

Guenther, G.C., Cunningham, A.G., LaRocque, P.E., Reid, D.J., n.d. Meeting the accuracy challenge in airborne bathymetry, in: Proceedings of EARSeL-SIG-Workshop LIDAR. Dresden, Germany, 16-17 June 2000; 27 pp.

Hamylton, S., Hedley, J., Beaman, R., 2015. Derivation of High-Resolution Bathymetry from Multispectral Satellite Imagery: A Comparison of Empirical and Optimisation Methods through Geographical Error Analysis. Remote Sensing 7, 16257–16273. https://doi.org/10.3390/rs71215829

Hartmann, K., Heege, T., Wettle, M., 2017. Effective Surveying Tool for the Shallow Water Zone: the increasing importance of satellite-derived bathymetry. Hydro International 20–22.

Harvey, A.C., Todd, P.H.J., 1983. Forecasting Economic Time Series With Structural and Box-Jenkins Models: A Case Study. Journal of Business & Economic Statistics 1, 299–307. https://doi.org/10.1080/07350015.1983.10509355

Hedley, J., Roelfsema, C., Koetz, B., Phinn, S., 2012. Capability of the Sentinel 2 mission for tropical coral reef mapping and coral bleaching detection. Remote Sensing of Environment 120, 145–155. https://doi.org/10.1016/j.rse.2011.06.028

Hernandez, W., Armstrong, R., 2016. Deriving Bathymetry from Multispectral Remote Sensing Data. Journal of Marine Science and Engineering 4, 8. https://doi.org/10.3390/jmse4010008

Herzfeld, U.C., McDonald, B.W., Wallin, B.F., Neumann, T.A., Markus, T., Brenner, A., Field, C., 2014. Algorithm for Detection of Ground and Canopy Cover in Micropulse Photon-Counting Lidar Altimeter Data in Preparation for the ICESat-2 Mission. IEEE Transactions on Geoscience and Remote Sensing 52, 2109–2125. https://doi.org/10.1109/TGRS.2013.2258350

Hickman, G.D., Hogg, J.E., 1969. Application of an airborne pulsed laser for near shore bathymetric measurements. Remote Sensing of Environment 1, 47–58. https://doi.org/10.1016/S0034-4257(69)90088-1

Hogrefe, K.R., Wright, D.J., Hochberg, E.J., 2008. Derivation and Integration of Shallow-Water Bathymetry: Implications for Coastal Terrain Modeling and Subsequent Analyses. Marine Geodesy 31, 299–317. https://doi.org/10.1080/01490410802466710

Horan, K.H., Kerekes, J.P., n.d. An automated statistical analysis approach to noise reduction for photon-counting lidar systems, in: IEEE International Geoscience and Remote Sensing Symposium-IGARSS. Melbourne, Australia, 21-26 July 2013, pp. 4336–4339.

Houser, C., Wernette, P., Rentschlar, E., Jones, H., Hammond, B., Trimble, S., 2015. Post-storm beach and dune recovery: Implications for barrier island resilience. Geomorphology 234, 54–63. https://doi.org/10.1016/j.geomorph.2014.12.044

Hu, L., Liu, Zhen, Liu, Zhishen, Hu, C., He, M.-X., 2014. Mapping bottom depth and albedo in coastal waters of the South China Sea islands and reefs using Landsat TM and ETM+ data. International Journal of Remote Sensing 35, 4156–4172. https://doi.org/10.1080/01431161.2014.916441

Huang, C., Yao, L., 2017. Semi-Analytical Retrieval of the Diffuse Attenuation Coefficient in Large and Shallow Lakes from GOCI, a High Temporal-Resolution Satellite. Remote Sensing 9, 825. https://doi.org/10.3390/rs9080825

Huang, W., Fu, B., 2004. A Spaceborne SAR Technique for Shallow Water Bathymetry Surveys. Journal of Coastal Research Special Issue No. 43, 223–228.

IHO, 2018a. Status of Hydrographic Surveying and Charting Worldwide (IHO/OHI Publication C-55). International Hydrographic Organization.

IHO, 2018b. Guidance on Crowdsourced Bathymetry (Draft).

IHO, 2016. The IHO-IOC GEBCO Cook Book, IHO Publication B-11, Monaco, Dec. 2016, 429 pp - IOC Manuals and Guides 63, France, Dec. 2016, 429 pp.

Intergovernmental Oceanographic Commission [WWW Document], n.d. URL http://ioc-unesco.org/ (accessed 8.25.16).

International Hydrographic Organization/Organisation Hydrographique Internationale (IHO) [WWW Document], n.d. URL http://www.iho.int/ (accessed 8.25.16).

Irish, J.L., Lillycrop, W.J., 1999. Scanning laser mapping of the coastal zone: the SHOALS system. ISPRS Journal of Photogrammetry and Remote Sensing 54, 123–129.

Jasinski, M.F., Stoll, J.D., Cook, W.B., Ondrusek, M., Stengel, E., in press. Inland and Near Shore Water Profiles Derived from High Altitude, Multiple Altimeter Beam Experimental Lidar (MABEL). Journal of Coastal Research.

Jasinski, M.F., Stoll, J.D., Cook, W.B., Ondrusek, M., Stengel, E., Brunt, K., 2016. Inland and Near-Shore Water Profiles Derived from the High-Altitude Multiple Altimeter Beam Experimental Lidar (MABEL). Journal of Coastal Research 76, 44–55. https://doi.org/10.2112/SI76-005

Jawak, S.D., Vadlamani, S.S., Luis, A.J., 2015. A Synoptic Review on Deriving Bathymetry Information Using Remote Sensing Technologies: Models, Methods and Comparisons. Advances in Remote Sensing 04, 147–162. https://doi.org/10.4236/ars.2015.42013

Jones, T.G., Coops, N.C., Sharma, T., 2010. Assessing the utility of airborne hyperspectral and LiDAR data for species distribution mapping in the coastal Pacific Northwest, Canada. Remote Sensing of Environment 114, 2841–2852. https://doi.org/10.1016/j.rse.2010.07.002

Jupp, D.L.B., 1988. Background and extensions to depth of penetration (DOP) mapping in shallow coastal waters, in: Proc Symposium on Remote Sensing of Coastal Zone, Gold Coast, Queensland. p. IV 2 (1)-IV 2 (19).

Justice, C.O., Román, M.O., Csiszar, I., Vermote, E.F., Wolfe, R.E., Hook, S.J., Friedl, M., Wang, Z., Schaaf, C.B., Miura, T., Tschudi, M., Riggs, G., Hall, D.K., Lyapustin, A.I., Devadiga, S., Davidson, C., Masuoka, E.J., 2013. Land and cryosphere products from Suomi NPP VIIRS: Overview and status. Journal of Geophysical Research: Atmospheres 118, 9753–9765. https://doi.org/10.1002/jgrd.50771

Kam, M., Xiaoxun Zhu, Kalata, P., 1997. Sensor Fusion for Mobile Robot Navigation. Proceedings of the IEEE 85, 108–119. https://doi.org/10.1109/JPROC.1997.554212

Kanno, A., Koibuchi, Y., Isobe, M., 2011a. Statistical Combination of Spatial Interpolation and Multispectral Remote Sensing for Shallow Water Bathymetry. IEEE Geoscience and Remote Sensing Letters 8, 64–67. https://doi.org/10.1109/LGRS.2010.2051658

Kanno, A., Koibuchi, Y., Isobe, M., 2011b. Shallow Water Bathymetry from Multispectral Satellite Images: Extensions of Lyzenga's Method for Improving Accuracy. Coastal Engineering Journal 53, 431–450. https://doi.org/10.1142/S0578563411002410

Kao, H.-M., Ren, H., Lee, C.-S., Chang, C.-P., Yen, J.-Y., Lin, T.-H., 2009. Determination of shallow water depth using optical satellite images. International Journal of Remote Sensing 30, 6241–6260. https://doi.org/10.1080/01431160902842367

Kennedy, D.M., Ierodiaconou, D., Schimel, A., 2014. Granitic coastal geomorphology: applying integrated terrestrial and bathymetric LiDAR with multibeam sonar to examine coastal landscape evolution. Earth Surface Processes and Landforms 39, 1663–1674. https://doi.org/10.1002/esp.3615

Kerfoot, W.C., Yousef, F., Green, S.A., Regis, R., Shuchman, R., Brooks, C.N., Sayers, M., Sabol, B., Graves, M., 2012. Light detection and ranging (LiDAR) and multispectral studies of disturbed Lake Superior coastal environments. Limnology and Oceanography 57, 749–771. https://doi.org/10.4319/lo.2012.57.3.0749

Khaleghi, B., Khamis, A., Karray, F.O., Razavi, S.N., 2013. Multisensor data fusion: A review of the state-of-the-art. Information Fusion 14, 28–44. https://doi.org/10.1016/j.inffus.2011.08.001

Kinzel, P.J., Wright, C.W., Nelson, J.M., Burman, A.R., 2007. Evaluation of an Experimental LiDAR for Surveying a Shallow, Braided, Sand-Bedded River. Journal of Hydraulic Engineering 133, 838–842. https://doi.org/10.1061/(ASCE)0733-9429(2007)133:7(838)

Knight, J.F., Voth, M.L., 2012. Application of MODIS Imagery for Intra-Annual Water Clarity Assessment of Minnesota Lakes. Remote Sensing 4, 2181–2198. https://doi.org/10.3390/rs4072181

Krainak, M.A., Yu, A.W., Yang, G., Li, S.X., Sun, X., n.d. Photon-counting detectors for space-based laser receivers, in: Proc. SPIE 7608. Presented at the Quantum Sensing and Nanophotonic Devices VII, San Francisco, CA, USA, 22 January 2010; 760827-9. https://doi.org/10.1117/12.846983

Kwok, R., Markus, T., Morison, J., Palm, S.P., Neumann, T.A., Brunt, K.M., Cook, W.B., Hancock, D.W., Cunningham, G.F., 2014. Profiling Sea Ice with a Multiple Altimeter Beam Experimental Lidar (MABEL). Journal of Atmospheric and Oceanic Technology 31, 1151–1168. https://doi.org/10.1175/JTECH-D-13-00120.1

LaDeau, S.L., Glass, G.E., Hobbs, N.T., Latimer, A., Ostfeld, R.S., 2011. Data–model fusion to better understand emerging pathogens and improve infectious disease forecasting. Ecological Applications 21, 1443–1460. https://doi.org/10.1890/09-1409.1

Lee, D.S., Shan, J., 2003. Combining Lidar Elevation Data and IKONOS Multispectral Imagery for Coastal Classification Mapping. Marine Geodesy 26, 117–127. https://doi.org/10.1080/01490410306707

Lee, K.R., Olsen, R.C., Kruse, F.A., Kim, A.M., 2013. Using multi-angle WorldView-2 imagery to determine bathymetry near Oahu, Hawaii, in: Shen, S.S., Lewis, P.E. (Eds.), Proc. SPIE 8743, Algorithms and Technologies for Multispectral, Hyperspectral, and Ultraspectral Imagery XIX. p. 874311. https://doi.org/10.1117/12.2015660

Lee, Z., Arnone, R., Boyce, D., Franz, B., Greb, S., Hu, C., Lavender, S., Lewis, M., Schaeffer, B., Shang, S., Wernand, M., Wilson, C., 2018. Global Water Clarity: Continuing a Century-Long Monitoring. EOS, American Geophysical Union, Washington, DC, 99, 1–10.

Lee, Z., Shang, S., Qi, L., Yan, J., Lin, G., 2016. A semi-analytical scheme to estimate Secchi-disk depth from Landsat-8 measurements. Remote Sensing of Environment 177, 101–106. https://doi.org/10.1016/j.rse.2016.02.033

Legleiter, C.J., 2012. Remote Measurement of River Morphology Via Fusion of Lidar Topography and Spectrally Based Bathymetry: Measuring River Morphology with Lidar and Spectral Bathymetry. Earth Surface Processes and Landforms 37, 499–518. https://doi.org/10.1002/esp.2262

Legleiter, C.J., Overstreet, B., 2012. Mapping Gravel Bed River Bathymetry from Space: Mapping River Bathymetry from Space. Journal of Geophysical Research: Earth Surface 117, 24pp. https://doi.org/10.1029/2012JF002539

Leon, J.X., Phinn, S.R., Hamylton, S., Saunders, M.I., 2013. Filling the 'white ribbon' – a multisource seamless digital elevation model for Lizard Island, northern Great Barrier Reef. International Journal of Remote Sensing 34, 6337–6354. https://doi.org/10.1080/01431161.2013.800659

Liceaga-Correa, M.A., Euan-Avila, J.I., 2002. Assessment of coral reef bathymetric mapping using visible Landsat Thematic Mapper data. International Journal of Remote Sensing 23, 3–14. https://doi.org/10.1080/01431160010008573

Liu, S., Gao, Y., Zheng, W., Li, X., 2015. Performance of two neural network models in bathymetry. Remote Sensing Letters 6, 321–330. https://doi.org/10.1080/2150704X.2015.1034885

Liu, S., Zhang, J., Ma, Y., 2010. Bathymetric ability of SPOT-5 multi-spectral image in shallow coastal water, in: Geoinformatics, 2010 18th International Conference On. IEEE, pp. 1–5.

Ludeno, G., Reale, F., Dentale, F., Carratelli, E., Natale, A., Soldovieri, F., Serafino, F., 2015. An X-Band Radar System for Bathymetry and Wave Field Analysis in a Harbour Area. Sensors 15, 1691–1707. https://doi.org/10.3390/s150101691

Lyons, M., Phinn, S., Roelfsema, C., 2011. Integrating Quickbird Multi-Spectral Satellite and Field Data: Mapping Bathymetry, Seagrass Cover, Seagrass Species and Change in Moreton Bay, Australia in 2004 and 2007. Remote Sensing 3, 42–64. https://doi.org/10.3390/rs3010042

Lyzenga, D.R., 1978. Passive remote sensing techniques for mapping water depth and bottom features. Applied optics 17, 379–383.

Lyzenga, D.R., Malinas, N.P., Tanis, F.J., 2006. Multispectral bathymetry using a simple physically based algorithm. IEEE Transactions on Geoscience and Remote Sensing 44, 2251–2259. https://doi.org/10.1109/TGRS.2006.872909

Lyzenga, D.R., Polcyn, F.C., 1979. Techniques for the Extraction of Water Depth Information from Landsat Digital Data. Hydrographic Topographic Center, Defense Mapping Agency 56 p.

Magruder, L.A., Wharton, M.E., Stout, K.D., Neuenschwander, A.L., n.d. Noise filtering techniques for photon-counting ladar data, in: Proc. SPIE 8379. Presented at the Laser Radar Technology and Applications XVII, Baltimore, MD, USA, 1 May 2012; 83790Q-9. https://doi.org/10.1117/12.919139

Mandlburger, G., Hauer, C., Wieser, M., Pfeifer, N., 2015. Topo-Bathymetric LiDAR for Monitoring River Morphodynamics and Instream Habitats—A Case Study at the Pielach River. Remote Sensing 7, 6160–6195. https://doi.org/10.3390/rs70506160

Manessa, M.D.M., Kanno, A., Sekine, M., Haidar, M., Yamamoto, K., Imai, T., Higuchi, T., 2016. Satellite-derived bathymetry using random forest algorithm and worldview-2 imagery. Geoplanning: Journal of Geomatics and Planning 3, 117. https://doi.org/10.14710/geoplanning.3.2.117-126

Mason, T., Rainbow, B., Mcvey, S., 2006. Colouring the “White Ribbon”: Strategic coastal monitoring in the south-east of England. Hydro International 10, 19–21.

McGill, M., Markus, T., Scott, V.S., Neumann, T., 2013. The Multiple Altimeter Beam Experimental Lidar (MABEL): An Airborne Simulator for the ICESat-2 Mission. Journal of Atmospheric and Oceanic Technology 30, 345–352. https://doi.org/10.1175/JTECH-D-12-00076.1

McKean, J., Tonina, D., Bohn, C., Wright, C. w., 2014. Effects of bathymetric lidar errors on flow properties predicted with a multi-dimensional hydraulic model. J. Geophys. Res. Earth Surf. 119, 644–664. https://doi.org/10.1002/2013JF002897

Melsheimer, C., Liew, S.C., 2001. Extracting bathymetry from multi-temporal spot images. Presented at the 22nd Asian Conference on Remote Sensing, Singapore.

Militino, A., Ugarte, M., Pérez-Goya, U., 2017. Stochastic Spatio-Temporal Models for Analysing NDVI Distribution of GIMMS NDVI3g Images. Remote Sensing 9, 76. https://doi.org/10.3390/rs9010076

Miller, A.D., van Rooyen, A., Rašić, G., Ierodiaconou, D.A., Gorfine, H.K., Day, R., Wong, C., Hoffmann, A.A., Weeks, A.R., 2016. Contrasting patterns of population connectivity between regions in a commercially important mollusc *Haliotis rubra* : integrating population genetics, genomics and marine LiDAR data. Molecular Ecology 25, 3845–3864. https://doi.org/10.1111/mec.13734

Miller, J., Battista, T.A., Pritchett, A.S., Rohmann, S.O., Rooney, J.J.B., 2011. Coral Reef Conservation Program mapping achievements and unmet needs. US Department of Commerce, National Oceanic and Atmospheric Administration, Coral Reef Conservation Program.

Minghelli-Roman, A., Dupouy, C., 2012. Bathymetric estimation in the lagoon of New Caledonia, using several MeRIS images, in: 2012 4th Workshop on Hyperspectral Image and Signal Processing: Evolution in Remote Sensing (WHISPERS) IEEE. pp. 1–4.

Mishra, D., Narumalani, S., Lawson, M., Rundquist, D., 2004. Bathymetric Mapping Using IKONOS Multispectral Data. GIScience & Remote Sensing 41, 301–321. https://doi.org/10.2747/1548-1603.41.4.301

Montes, M.A., Churnside, J., Lee, Z., Gould, R., Arnone, R., Weidemann, A., 2011. Relationships between water attenuation coefficients derived from active and passive remote sensing: a case study from two coastal environments. Applied Optics 50, 2990. https://doi.org/10.1364/AO.50.002990

Moses, S.A., Janaki, L., Joseph, S., Gomathi, J.P., Joseph, J., 2013. Lake bathymetry from Indian Remote Sensing (P6-LISS III) satellite imagery using artificial neural network model. Lakes & Reservoirs: Research & Management 18, 145–153. https://doi.org/10.1111/lre.12027

Moussavi, M.S., Abdalati, W., Scambos, T., Neuenschwander, A., 2014. Applicability of an automatic surface detection approach to micro-pulse photon-counting lidar altimetry data: implications for canopy height retrieval from future ICESat-2 data. International Journal of Remote Sensing 35, 5263–5279. https://doi.org/10.1080/01431161.2014.939780

Mueller, J.L., 2000. SeaWiFS algorithm for the diffuse attenuation coefficient, K (490), using water-leaving radiances at 490 and 555 nm, In: SeaWiFS Postlaunch Calibration and Validation Analyses, Part 3, 11: 24-27. NASA Goddard Space Flight Center, Greenbelt, MD, USA.

Myers, E., Wong, A., Hess, K., White, S., Spargo, E., Feyen, J., Yang, Z., Richardson, P., Auer, C., Sellars, J., others, n.d. Development of a National VDatum, and its application to sea level rise in North Carolina, in: Proceedings of United States Hydrographic Conference. San Diego, CA, USA, 29-31 March 2005; paper 9-3, 25 pp.

NASA, 2018. Technical Specs | Icesat-2 [WWW Document]. URL https://icesat-2.gsfc.nasa.gov/science/specs (accessed 1.15.18).

NASA, 2014. Goddard Space Flight Center: MABEL ICESat-2 simulation data, Version 9, Greenbelt, MD USA, https://icesat.gsfc.nasa.gov/icesat2/data/mabel/mabel_docs.php.

NASA Applied Sciences Program: Program Strategy, 2010. . National Aeronautics and Space Administration, Washington, DC.

Nelder, J.A., Mead, R., 1965. A Simplex Method for Function Minimization. The Computer Journal 7, 308–313. https://doi.org/10.1093/comjnl/7.4.308

Neumann, T.A., 2016. (NASA Goddard Space Flight Center, Greenbelt, MD, USA). Personal communication,.

Nicosia, A., Duchesne, T., Rivest, L.-P., Fortin, D., 2017. A general hidden state random walk model for animal movement. Computational Statistics & Data Analysis 105, 76–95. https://doi.org/10.1016/j.csda.2016.07.009

Niroumand-Jadidi, M., Vitti, A., 2016. Improving the accuracies of bathymetric models based on multiple regression for calibration (case study: Sarca River, Italy), in: Bostater, C.R., Mertikas, S.P., Neyt, X., Nichol, C., Aldred, O. (Eds.), . p. 99990Q. https://doi.org/10.1117/12.2242083

NOAA, 2016a. U.S. Arctic Nautical Charting Plan: Supporting Sustainable Marine Transportation in Arctic Alaska. National Oceanic and Atmospheric Administration, Office of Coast Survey, Marine Chart Division.

NOAA, 2016b. 2016 NOAA NGS Topobathy Lidar DEM: Marthas Vineyard and Nantucket Island, MA | ID: 51268 | InPort [WWW Document]. URL https://inport.nmfs.noaa.gov/inport/item/51268 (accessed 8.6.19).

NOAA, n.d. Datums for 8449130, Nantucket Island, MA [WWW Document]. URL https://tidesandcurrents.noaa.gov/datums.html?id=8449130 (accessed 6.15.19).

NOAA CSC, 2011. Report of Survey, Lake Superior Bathymetric Lidar (Contract EA133C-05-CQ-1051) (Report of Survey). National Oceanic and Atmospheric Administration, Coastal Services Center, Charleston, SC, USA.

NOAA NGS, 2017. Nantucket and Martha's Vinyeard Topobathy Final Report of Survey.

NOAA NGS, 2013. Great Lakes Low Water Datums [WWW Document]. Great Lakes Low Water Datums. URL https://tidesandcurrents.noaa.gov/gldatums.html (accessed 7.7.16).

NRC, 2004. A geospatial framework for the coastal zone: national needs for coastal mapping and charting. National Academies Press., Washington, D.C., USA.

Oldale, R.N., 2001. Cape Cod, Martha's Vineyard & Nantucket : the geologic story. On Cape Publications, Yarmouth Port, Mass.

Pacheco, A., Horta, J., Loureiro, C., Ferreira, ó., 2015. Retrieval of nearshore bathymetry from Landsat 8 images: A tool for coastal monitoring in shallow waters. Remote Sensing of Environment 159, 102–116. https://doi.org/10.1016/j.rse.2014.12.004

Pack, R.T., Brooks, V., Young, J., Vilaca, N., Vatslid, S., Rindle, P., Kurz, S., Parrish, C., Craig, R., Smith, P.W., 2012. Chapter 2: An Overview of ALS Technology, in: Manual of Airborne Topographic Lidar. American Society for Photogrammetry and Remote Sensing, pp. 7–97.

Pahlevan, N., Chittimalli, S.K., Balasubramanian, S.V., Vellucci, V., 2019. Sentinel-2/Landsat-8 product consistency and implications for monitoring aquatic systems. Remote Sensing of Environment 220, 19–29. https://doi.org/10.1016/j.rse.2018.10.027

Paredes, J.M., Spero, R.E., 1983. Water depth mapping from passive remote sensing data under a generalized ratio assumption. Applied Optics 22, 1134–1135.

Parker, B., Hess, K., Milbert, D., Gill, S., 2003. A national vertical datum transformation tool. Sea Technology 44, 10–15.

Parrish, C.E., Magruder, L.A., Neuenschwander, A.L., Forfinski-Sarkozi, N., Alonzo, M., Jasinski, M., 2019. Validation of ICESat-2 ATLAS Bathymetry and Analysis of ATLAS's Bathymetric Mapping Performance. Remote Sensing 11, 1634. https://doi.org/10.3390/rs11141634

Pattanaik, A., Sahu, K., Bhutiyani, M.R., 2015. Estimation of Shallow Water Bathymetry Using IRS-Multispectral Imagery of Odisha Coast, India. Aquatic Procedia 4, 173–181. https://doi.org/10.1016/j.aqpro.2015.02.024

Pe'eri, S., Azuike, C., Parrish, C., 2013. Satellite-Derived Bathymetry a Reconnaissance Tool for Hydrography. Hydro. Int. 17, 16–19.

Pe'eri, S., Madore, B., Nyberg, J., Snyder, L., Parrish, C., Smith, S., 2016. Identifying Bathymetric Differences over Alaska's North Slope using a Satellite-derived Bathymetry Multi-temporal Approach. Journal of Coastal Research 76, 56–63. https://doi.org/10.2112/SI76-006

Pe'eri, S., Morgan, L.V., Philpot, W.D., Armstrong, A.A., 2011. Shoreline mapping resolved from airborne LIDAR bathymetry (ALB) waveforms. Journal of Coastal Research, Special Issue: Applied LIDAR Techniques 62, 75–85.

Pe'eri, S., Parrish, C., Azuike, C., Alexander, L., Armstrong, A., 2014. Satellite Remote Sensing as a Reconnaissance Tool for Assessing Nautical Chart Adequacy and Completeness. Marine Geodesy 37, 293–314. https://doi.org/10.1080/01490419.2014.902880

Pe'eri, S., Philpot, W., 2007. Increasing the Existence of Very Shallow-Water LIDAR Measurements Using the Red-Channel Waveforms. IEEE Transactions on Geoscience and Remote Sensing 45, 1217–1223. https://doi.org/10.1109/TGRS.2007.894584

Petrie, G., Toth, C.K., 2009. Airborne and Spaceborne Laser Profilers and Scanners, in: Shan, J., Toth, C.K. (Eds.), Topographic Laser Ranging and Scanning: Principles and Processing. CRC Press/Taylor & Francis Group, Boca Raton, FL, pp. 29–85.

Philpot, W.D., 1989. Bathymetric mapping with passive multispectral imagery. Applied Optics 28, 1569–1578.

Polcyn, F.C., Rollin, R.A., 1969. Remote Sensing Techniques for the Location and Measurement of Shallow-Water Features (No. 8973-10- P). Willow Run Laboratories, Institute of Science and Technology, The University of Michigan, Ann Arbor, MI.

Priedhorsky, W.C., Smith, R.C., Ho, C., 1996. Laser ranging and mapping with a photon-counting detector. Applied optics 35, 441–452.

Proietti, T., 2006. Temporal disaggregation by state space methods: Dynamic regression methods revisited. The Econometrics Journal 9, 357–372. https://doi.org/10.1111/j.1368-423X.2006.00189.x

Provost, J.-N., Collet, C., Rostaing, P., Pérez, P., Bouthemy, P., 2004. Hierarchical Markovian segmentation of multispectral images for the reconstruction of water depth maps. Computer Vision and Image Understanding 93, 155–174. https://doi.org/10.1016/j.cviu.2003.07.004

Quadros, N.D., 2013. Unlocking the characteristics of Bathymetric Lidar sensors. LiDAR Magazine 3, 62–67.

Quadros, N.D., Collier, P.A., Fraser, C.S., 2008. Integration of bathymetric and topographic LiDAR: a preliminary investigation. The International Archives of the Photogrammetry, Remote Sensing and Spatial Information Sciences 36, 1299–1304.

Roberts, A.C.B., Anderson, J. M., 1999. Shallow water bathymetry using integrated airborne multi-spectral remote sensing. International Journal of Remote Sensing 20, 497–510. https://doi.org/10.1080/014311699213299

Salah, M., 2016. Determination of Shallow Water Depths using Inverse Probability Weighted Interpolation: A Hybrid System-Based Method. International Journal of Geoinformatics 12.

Saucan, A., Sintes, C., Chonavel, T., Caillec, J.L., 2014. Robust, track before detect particle filter for bathymetric sonar application, in: 17th International Conference on Information Fusion (FUSION). Presented at the 17th International Conference on Information Fusion (FUSION), pp. 1–7.

Saylam, K., Brown, R.A., Hupp, J.R., 2017. Assessment of depth and turbidity with airborne Lidar bathymetry and multiband satellite imagery in shallow water bodies of the Alaskan North Slope. International Journal of Applied Earth Observation and Geoinformation 58, 191–200. https://doi.org/10.1016/j.jag.2017.02.012

Schmitt, M., Zhu, X.X., 2016. Data Fusion and Remote Sensing: An ever-growing relationship. IEEE Geoscience and Remote Sensing Magazine 4, 6–23. https://doi.org/10.1109/MGRS.2016.2561021

Seabold, S., Perktold, J., 2010. Statsmodels: Econometric and statistical modeling with python, in: 9th Python in Science Conference.

Shi, K., Zhang, Y., Zhu, G., Qin, B., Pan, D., 2018. Deteriorating water clarity in shallow waters: Evidence from long term MODIS and in-situ observations. International Journal of Applied Earth Observation and Geoinformation 68, 287–297. https://doi.org/10.1016/j.jag.2017.12.015

Shrestha, K.Y., Carter, W.E., Slatton, K.C., Cossio, T.K., 2012. Shallow Bathymetric Mapping via Multistop Single Photoelectron Sensitivity Laser Ranging. IEEE Transactions on Geoscience and Remote Sensing 50, 4771–4790. https://doi.org/10.1109/TGRS.2012.2192445

Shumway, R.H., Stoffer, D.S., 2017. Time Series Analysis and Its Applications : With R Examples [WWW Document].

Singh, A., Kumar, U., Seitz, F., 2015. Remote Sensing of Storage Fluctuations of Poorly Gauged Reservoirs and State Space Model (SSM)-Based Estimation. Remote Sensing 7, 17113–17134. https://doi.org/10.3390/rs71215872

Smith, W.H., Sandwell, D.T., 2004. Conventional bathymetry, bathymetry from space, and geodetic altimetry. Oceanography 17, 8–23.

Sneed, W.A., Hamilton, G.S., 2007. Evolution of melt pond volume on the surface of the Greenland Ice Sheet. Geophysical Research Letters 34. https://doi.org/10.1029/2006GL028697

Solonenko, M.G., Mobley, C.D., 2015. Inherent optical properties of Jerlov water types. Applied Optics 54, 5392. https://doi.org/10.1364/AO.54.005392

Statsmodels, n.d. SARIMAX: incremental Kalman filter (question) · Issue #5563 · statsmodels/statsmodels [WWW Document]. GitHub. URL https://github.com/statsmodels/statsmodels/issues/5563 (accessed 7.20.19).

Stepčenko, A., Čižovs, J., 2016. Markov Chain Modelling for Short-Term NDVI Time Series Forecasting. Information Technology and Management Science 19. https://doi.org/10.1515/itms-2016-0009

Stewart, C., Renga, A., Gaffney, V., Schiavon, G., 2016. Sentinel-1 bathymetry for North Sea palaeolandscape analysis. International Journal of Remote Sensing 37, 471–491. https://doi.org/10.1080/01431161.2015.1129563

Storey, J., Roy, D.P., Masek, J., Gascon, F., Dwyer, J., Choate, M., 2016. A note on the temporary misregistration of Landsat-8 Operational Land Imager (OLI) and Sentinel-2 Multi Spectral Instrument (MSI) imagery. Remote Sensing of Environment 186, 121–122. https://doi.org/10.1016/j.rse.2016.08.025

Stumpf, R.P., Holderied, K., Sinclair, M., 2003. Determination of water depth with high-resolution satellite imagery over variable bottom types. Limnology and Oceanography 48, 547–556.

Su, H., Liu, H., Heyman, W.D., 2008. Automated Derivation of Bathymetric Information from Multi-Spectral Satellite Imagery Using a Non-Linear Inversion Model. Marine Geodesy 31, 281–298. https://doi.org/10.1080/01490410802466652

Su, H., Liu, H., Wang, L., Filippi, A.M., Heyman, W.D., Beck, R.A., 2014. Geographically Adaptive Inversion Model for Improving Bathymetric Retrieval From Satellite Multispectral Imagery. IEEE Transactions on Geoscience and Remote Sensing 52, 465–476. https://doi.org/10.1109/TGRS.2013.2241772

T. Nicosevici, R. Garcia, M. Carreras, M. Villanueva, 2004. A review of sensor fusion techniques for underwater vehicle navigation, in: Oceans '04 MTS/IEEE Techno-Ocean '04 (IEEE Cat. No.04CH37600). Presented at the Oceans '04 MTS/IEEE Techno-Ocean '04 (IEEE Cat. No.04CH37600), pp. 1600-1605 Vol.3. https://doi.org/10.1109/OCEANS.2004.1406361

Tandeo, P., Ailliot, P., Autret, E., 2011. Linear Gaussian state-space model with irregular sampling: application to sea surface temperature. Stochastic Environmental Research and Risk Assessment 25, 793–804. https://doi.org/10.1007/s00477-010-0442-8

Tanis, F.J., Hieber, R., Thomson, F.J., 1983. Multi-Temporal Analysis of Landsat Imagery for Bathymetry. DTIC Document.

Taramelli, A., Valentini, E., Innocenti, C., Cappucci, S., n.d. FHYL: Field spectral libraries, airborne hyperspectral images and topographic and bathymetric LiDAR data for complex coastal mapping, in: IEEE International Geoscience and Remote Sensing Symposium (IGARSS) 21-26 July 2013 Melbourne Australia. pp. 2270–2273. https://doi.org/10.1109/IGARSS.2013.6723270

Traganos, D., Poursanidis, D., Aggarwal, B., Chrysoulakis, N., Reinartz, P., 2018. Estimating Satellite-Derived Bathymetry (SDB) with the Google Earth Engine and Sentinel-2. Remote Sensing 10, 859. https://doi.org/10.3390/rs10060859

Tripathi, N.K., Rao, A.M., 2002. Bathymetric mapping in Kakinada Bay, India, using IRS-1D LISS-III data. International Journal of Remote Sensing 23, 1013–1025. https://doi.org/10.1080/01431160110075785

Tuell, G., Barbor, K., Wozencraft, J., n.d. Overview of the coastal zone mapping and imaging lidar (CZMIL): a new multisensor airborne mapping system for the U.S. Army Corps of Engineers, in: Proc. SPIE 7695. Presented at the Algorithms and Technologies for Multispectral, Hyperspectral, and Ultraspectral Imagery XVI, Orlando, FL, USA, 12 May 2010; 76950R-8. https://doi.org/10.1117/12.851905

Tulldahl, H.M., Philipson, P., Kautsky, H., Wikström, S.A., n.d. Sea floor classification with satellite data and airborne lidar bathymetry, in: Proc. SPIE 8724. Presented at the Ocean Sensing and Monitoring V, Baltimore, MD, USA, 3 June 2013; 87240B-16. https://doi.org/10.1117/12.2015727

UNEP-WCMC et al., 2010. Global distribution of coral reefs, compiled from multiple sources including the Millennium Coral Reef Mapping Project. Version 2.0, updated by UNEP-WCMC. Includes contributions from IMaRSUSF and IRD (2005), IMaRS-USF (2005) and Spalding et al. (2001). Cambridge (UK): UNEP World Conservation Monitoring Centre URL: http://data.unepwcmc.org/datasets/1.

US Department of Commerce, N.S. and I.S., n.d. NOAA National Centers for Environmental Information (NCEI) [WWW Document]. URL https://www.ngdc.noaa.gov/ngdc.html (accessed 8.28.16).

USGS, 2016. Landsat 8 (L8) Data Users Handbook, Version 2.0.

USGS, n.d. Landsat Collection 2 [WWW Document]. URL https://www.usgs.gov/land-resources/nli/landsat/landsat-collection-2 (accessed 6.15.19).

van Hengel, W., Spitzer, D., 1991. Multi-temporal water depth mapping by means of Landsat TM. International Journal of Remote Sensing 12, 703–712. https://doi.org/10.1080/01431169108929687

Vanhellemont, Q., 2019. Adaptation of the dark spectrum fitting atmospheric correction for aquatic applications of the Landsat and Sentinel-2 archives. Remote Sensing of Environment 225, 175–192. https://doi.org/10.1016/j.rse.2019.03.010

Vanhellemont, Q., Ruddick, K., 2016. ACOLITE processing for Sentinel-2 and Landsat-8: atmospheric correction and aquatic applications 12.

Varma, H., Fadaie, K., Habbane, M., Stockhausen, J., 2003. Confusion in data fusion. International Journal of Remote Sensing 24, 627–636. https://doi.org/10.1080/01431160210155028

Vinayaraj, P., Raghavan, V., Masumoto, S., 2016. Satellite-Derived Bathymetry using Adaptive Geographically Weighted Regression Model. Marine Geodesy 39, 458–478. https://doi.org/10.1080/01490419.2016.1245227

Wang, M., Son, S., Harding, L.W., 2009. Retrieval of diffuse attenuation coefficient in the Chesapeake Bay and turbid ocean regions for satellite ocean color applications. Journal of Geophysical Research 114. https://doi.org/10.1029/2009JC005286

Wang, X., Pan, Z., Glennie, C., 2016. A Novel Noise Filtering Model for Photon-Counting Laser Altimeter Data. IEEE Geoscience and Remote Sensing Letters 13, 947–951. https://doi.org/10.1109/LGRS.2016.2555308

Ward, L., 2016. (University of New Hampshire, Department of Earth Sciences, Center for Coastal and Ocean Mapping). Personal communication,.

Warne, D.K., 1978. Landsat as an aid in the preparation of hydrographic charts. Photogrammetric Engineering & Remote Sensing 44, 1011–1016.

Weatherall, P., Marks, K.M., Jakobsson, M., Schmitt, T., Tani, S., Arndt, J.E., Rovere, M., Chayes, D., Ferrini, V., Wigley, R., 2015. A New Digital Bathymetric Model of the World's Oceans: New Digital Bathymetric Model. Earth and Space Science 2, 331–345. https://doi.org/10.1002/2015EA000107

Wedding, L.M., Friedlander, A.M., McGranaghan, M., Yost, R.S., Monaco, M.E., 2008. Using bathymetric lidar to define nearshore benthic habitat complexity: Implications for management of reef fish assemblages in Hawaii. Remote Sensing of Environment, Applications of Remote Sensing to Monitoring Freshwater and Estuarine Systems 112, 4159–4165. https://doi.org/10.1016/j.rse.2008.01.025

Wikle, C.K., Milliff, R.F., Herbei, R., Leeds, W.B., 2013. Modern Statistical Methods in Oceanography: A Hierarchical Perspective. Statistical Science 28, 466–486.

Wilson, G.W., Özkan-Haller, H.T., Holman, R.A., Haller, M.C., Honegger, D.A., Chickadel, C.C., 2014. Surf zone bathymetry and circulation predictions via data assimilation of remote sensing observations. Journal of Geophysical Research: Oceans 119, 1993–2016. https://doi.org/10.1002/2013JC009213

Wozencraft, J.M., Park, J.Y., 2013. Integrated LiDAR and Hyperspectral, in: Goodman, J.A., Purkis, S.J., Phinn, S.R. (Eds.), Coral Reef Remote Sensing. Springer Netherlands, Dordrecht, pp. 175–191. https://doi.org/10.1007/978-90-481-9292-2_7

Wüst, J.C., 2004. Data-driven probablistic predictions of sand wave bathymetry. Marine Sandwave and River Dune Dynamics II 338–345.

Yousef, F., Kerfoot, W.C., Brooks, C.N., Shuchman, R., Sabol, B., Graves, M., 2013. Using LiDAR to reconstruct the history of a coastal environment influenced by legacy mining. Journal of Great Lakes Research 39, 205–216. https://doi.org/10.1016/j.jglr.2013.01.003

Yu, A.W., Stephen, M.A., Li, S.X., Shaw, G.B., Seas, A., Dowdye, E., Troupaki, E., Liiva, P., Poulios, D., Mascetti, K., n.d. Space laser transmitter development for ICESat-2 mission, in: Proc. SPIE 7578.

Presented at the Solid State Lasers XIX: Technology and Devices, San Francisco, CA, USA, 24-28 January 2010; 757809-11. https://doi.org/10.1117/12.843342

Zavalas, R., Ierodiaconou, D., Ryan, D., Rattray, A., Monk, J., 2014. Habitat Classification of Temperate Marine Macroalgal Communities Using Bathymetric LiDAR. Remote Sensing 6, 2154–2175. https://doi.org/10.3390/rs6032154